

MULTIPLE DEGREE OF FREEDOM INVERTED PENDULUM DYNAMICS:  
MODELING, COMPUTATION, AND EXPERIMENTATION

by

Cheng-Yuan Jerry Chen

---

A Dissertation Presented to the  
FACULTY OF THE GRADUATE SCHOOL  
UNIVERSITY OF SOUTHERN CALIFORNIA  
In Partial Fulfillment of the  
Requirements for the Degree  
DOCTOR OF PHILOSOPHY  
(AEROSPACE AND MECHANICAL ENGINEERING)

May 2009

Copyright 2009

Cheng-Yuan Jerry Chen

UMI Number: 3355370

### INFORMATION TO USERS

The quality of this reproduction is dependent upon the quality of the copy submitted. Broken or indistinct print, colored or poor quality illustrations and photographs, print bleed-through, substandard margins, and improper alignment can adversely affect reproduction.

In the unlikely event that the author did not send a complete manuscript and there are missing pages, these will be noted. Also, if unauthorized copyright material had to be removed, a note will indicate the deletion.



UMI Microform 3355370  
Copyright 2009 by ProQuest LLC  
All rights reserved. This microform edition is protected against  
unauthorized copying under Title 17, United States Code.

---

ProQuest LLC  
789 East Eisenhower Parkway  
P.O. Box 1346  
Ann Arbor, MI 48106-1346

# Table of Contents

<b>List of Figures</b>	<b>iv</b>
<b>Abstract</b>	<b>x</b>
<b>Chapter 1 Inverted Pendulum Dynamics</b>	<b>1</b>
1.1 Introduction . . . . .	1
1.2 Motivation and Related Early Work on Inverted Pendulum Dynamics . . . . .	4
<b>Chapter 2 Inverted Pendulum Under Periodic Vertical Forcing</b>	<b>7</b>
2.1 Single Degree of Freedom Inverted Pendulum Model . . . . .	7
Equations of Motion . . . . .	7
Linearized $s$ DOF Model and Mathieu's Equation . . . . .	13
Numerical Integration of the Nonlinear $s$ DOF Inverted Pendulum Model . . . . .	28
Nonlinear Analysis of $s$ DOF Model Using Perturbation Theory . . . . .	41
<b>Chapter 3 Experiments on the <math>s</math>DOF Inverted Pendulum</b>	<b>57</b>
3.1 Material and Methods . . . . .	57
Driving Inverted Pendulum by Loud Speaker . . . . .	57
Inverted Pendulum Motion Using High Speed Camera . . . . .	60
System Calibration and Image Processing by NI Vision Builder . . . . .	63
Data Analysis and Data Filtering . . . . .	64
3.2 Single Degree of Freedom System Experimental Results . . . . .	67
<b>Chapter 4 Multiple Degree of Freedom Inverted Pendulum Model</b>	<b>74</b>
4.1 Formulate $n$ DOF System Equation of Motion From Lagrangian Approach . . . . .	74
4.2 Validate the Single Degree of Freedom Inverted Pendulum Model . . . . .	81
4.3 Two Degree of Freedom Inverted Pendulum Model . . . . .	82
4.4 Coefficients of 2DOF Inverted Pendulum Equation of Motion . . . . .	86
4.5 Numerical Integration on Nonlinear 2DOF Inverted Pendulum Model . . . . .	89
4.6 Small Angle Assumption to Obtain Linear 2DOF Inverted Pendulum Model . . . . .	92

Simulation Results on Linear 2DOF Inverted Pendulum Model under Mode 1 Vibration . . . . .	97
Simulation Results on Linear 2DOF Inverted Pendulum Model under Mode 2 Vibration . . . . .	101
Numerical simulation result comparison . . . . .	110
<b>Chapter 5 Experiments on the 2DOF Inverted Pendulum</b>	<b>115</b>
5.1 Material and Methods for 2DOF Experimentations . . . . .	115
5.2 2DOF System Experimental Results . . . . .	120
Experimental Results on 2DOF Mode 1 Vibration . . . . .	120
Experimental Results on 2DOF Mode 2 Vibration . . . . .	124
Experimental Results on 2DOF Upright Vertical Mode . . . . .	128
<b>Chapter 6 Summary and Future Work</b>	<b>133</b>
<b>Bibliography</b>	<b>135</b>
<b>Appendix</b>	<b>140</b>

# List of Figures

2.1	Single degree of freedom inverted pendulum under vertical periodic forcing at its base $P$ . . . . .	9
2.2	Transition curves for the linear Mathieu equation on the $\delta - \epsilon$ plane separate regions of bounded solution(shaded area) from regions of unbounded solution or unstable system(white area). . . . .	23
2.3	Stutt's diagram for stability regions separated by the transition curves of $n = 0$ and $n = 1$ within the range of $-0.5 < \delta < 0.5$ . . . . .	25
2.4	Stability regime diagram of single degree of freedom inverted pendulum under vertical periodic forcing showing in the $\epsilon - \bar{\omega}$ plane. . . . .	27
2.5	Numerical integration results of the single degree of freedom inverted pendulum under normalized forcing amplitude $\epsilon = 0.1708$ and normalized forcing frequency $\bar{\omega} = 8.7313$ with initial condition $\theta_0 = 0.1$ and $\dot{\theta}_0 = 0$ . (a)System time response. (b)Angular velocity time trace. (c)System phase portrait. (d)3D view of phase portrait with respect to periodic forcing. . . . .	32
2.6	Numerical integration results of single degree of freedom inverted pendulum under $\epsilon = 0.1710$ and $\bar{\omega} = 14.2784$ with initial condition $\theta_0 = 0.1$ and $\dot{\theta}_0 = 0$ . (a)System time response. (b)Angular velocity time trace. (c)System phase portrait. (d)3D view of phase portrait with respect to periodic forcing. . . . .	34
2.7	Numerical integration results of single degree of freedom inverted pendulum under normalized forcing amplitude $\epsilon = 0.2193$ and normalized forcing frequency $\bar{\omega} = 14.2784$ with initial condition $\theta_0 = 0.1$ and $\dot{\theta}_0 = 0$ . (a)System time response. (b)Angular velocity time trace. (c)System phase portrait. (d)3D view of phase portrait with respect to periodic forcing. . . . .	35

2.8	Numerical integration results of single degree of freedom inverted pendulum under normalized forcing amplitude $\epsilon = 0.400$ and normalized forcing frequency $\bar{\omega} = 12.8506$ with initial condition $\theta_0 = 0.56$ and $\dot{\theta}_0 = 0$ . (a)System time response. (b)Angular velocity time trace. (c)System phase portrait. (d)3D view of phase portrait with respect to periodic forcing. . . . .	37
2.9	Numerical integration results of single degree of freedom inverted pendulum under normalized forcing amplitude $\epsilon = 0.200$ and normalized forcing frequency $\bar{\omega} = 14.2784$ with initial condition $\theta_0 = 0.1$ and $\dot{\theta}_0 = 0$ . (a)System time response. (b)Angular velocity time trace. (c)System phase portrait. (d)3D view of phase portrait with respect to periodic forcing. . . . .	38
2.10	Numerical simulation results of periodic solutions from varying normalized forcing amplitude $\epsilon$ with fixed normalized forcing frequency $\bar{\omega} = 14.2784$ . Graphs from top to bottom show $\epsilon$ values increase from $\epsilon = 0.1019$ to $\epsilon = 0.1240$ . From left to right showing four geometric representations of system response: time trace, phase portrait, 3D phase portrait, and PSD, respectively.	42
2.11	(Cont. of 2.10) Numerical simulation results of periodic solutions from varying normalized forcing amplitude $\epsilon$ with fixed normalized forcing frequency $\bar{\omega} = 14.2784$ . Graphs from top to bottom show $\epsilon$ values increase from $\epsilon = 0.1293$ to $\epsilon = 0.1531$ . From left to right showing four geometric representations of system response: time trace, phase portrait, 3D phase portrait, and PSD, respectively. . . . .	43
2.12	(Cont. of 2.11) Numerical simulation results of periodic solutions from varying normalized forcing amplitude $\epsilon$ with fixed normalized forcing frequency $\bar{\omega} = 14.2784$ . Graphs from top to bottom show $\epsilon$ values increase from $\epsilon = 0.1611$ to $\epsilon = 0.3346$ . From left to right showing four geometric representations of system response: time trace, phase portrait, 3D phase portrait, and PSD, respectively. . . . .	44
2.13	Numerical simulation based on perturbation analysis solutions. All simulation is under fixed normalized driving amplitude $\epsilon = 0.1233$ . . . . .	54
2.14	Quantitative comparison of the perturbation analysis simulation result to the experimental result. (a)filtered experimental time trace and phase portrait (b)simulation time trace and phase portrait. . . . .	56
3.1	Single degree of freedom inverted pendulum experimental setup. . . . .	59
3.2	Precise experimental measurements from image acquisition and image processing using XS-3 high-speed camera, NI Vision Builder, MS Excel and Matlab.	60

3.3	Three dimensional view of the SDOF experimental setup. . . . .	62
3.4	NI Vision Bulider software applied to a single degree of freedom experimental setup. . . . .	65
3.5	Zoom-in view of experimental data of inverted pendulum base motion. $X$ denotes vertical periodic forcing displacement which has coordinate $u(t) = \varepsilon \cos \omega t$ ; $Y$ denotes horizontal motion. . . . .	66
3.6	Experiment on single degree of freedom pendulum under $10.0 \pm 0.2$ mm driving amplitude and 25 Hz driving frequency. System has normalized amplitude $\bar{\varepsilon} = 0.14 \pm 0.01$ and normalized frequency $\bar{\omega} = 13.3 \pm 0.2$ . . . . .	69
3.7	Experiment on single degree of freedom pendulum under $8.0 \pm 0.3$ mm driving amplitude and 25 Hz driving frequency. System has normalized amplitude $\bar{\varepsilon} = 0.11 \pm 0.01$ and normalized frequency $\bar{\omega} = 13.3 \pm 0.2$ . . . . .	71
3.8	Experiment on single degree of freedom pendulum under $6.5 \pm 0.3$ mm driving amplitude and 30 Hz driving frequency. System has normalized amplitude $\bar{\varepsilon} = 0.09 \pm 0.01$ and normalized frequency $\bar{\omega} = 15.9 \pm 0.2$ . . . . .	73
4.1	Geometric relationship of general case nDOF inverted pendulum. under vertical oscillatory forcing at its base . . . . .	76
4.2	Simplified two degree of freedom inverted pendulum model with two point masses mounted on two rigid rods. Two modes of vibration shown on graph: Mode 1(left) and Mode 2(right). . . . .	88
4.3	2DOF inverted pendulum under mode 1 vibration with vertical periodic forcing amplitude $\varepsilon = 0.00593$ and forcing frequency $\omega = 250$ rad/s. Initial conditions are $\theta_{1_0} = 0.05, \dot{\theta}_{1_0} = 0$ and $\theta_{2_0} = 0.1, \dot{\theta}_{2_0} = 0$ . . . . .	91
4.4	When applying different initial conditions to the same 2DOF inverted pendulum model we can get mode 2 vibration with the same vertical periodic forcing amplitude $\varepsilon = 0.00593$ and forcing frequency $\omega = 250$ rad/s. Initial conditions are $\theta_{1_0} = 0.1, \dot{\theta}_{1_0} = 0$ and $\theta_{2_0} = -0.101, \dot{\theta}_{2_0} = 0$ . . . . .	93
4.5	2DOF inverted pendulum under mode 1 vibration. The periodic input forcing amplitude was $\varepsilon = 0.2138$ and the forcing frequency was $\omega = 200$ . . . . .	99
4.6	2DOF inverted pendulum under mode 1 vibration. The periodic input forcing amplitude was $\varepsilon = 0.03025$ and the forcing frequency was $\omega = 200$ . . . . .	100

4.7	2DOF inverted pendulum under mode 1 vibration. The periodic input forcing amplitude was $\varepsilon = 0.03023$ and the forcing frequency was $\omega = 200$ . The inverted pendulum shows quasiperiodic response. . . . .	102
4.8	2DOF inverted pendulum under mode 2 vibration. The periodic input forcing amplitude was $\varepsilon = 0.2138$ and the forcing frequency was $\omega = 200$ . . . . .	104
4.9	2DOF inverted pendulum under mode 2 vibration. The periodic input forcing amplitude was $\varepsilon = 0.1514$ and the forcing frequency was $\omega = 200$ . . . . .	105
4.10	2DOF inverted pendulum under mode 2 vibration. The periodic input forcing amplitude was $\varepsilon = 0.11637$ and the forcing frequency was $\omega = 200$ . . . . .	106
4.11	2DOF inverted pendulum under mode 2 vibration. The periodic input forcing amplitude was $\varepsilon = 0.05037$ and the forcing frequency was $\omega = 200$ . . . . .	108
4.12	2DOF inverted pendulum under mode 2 vibration. The periodic input forcing amplitude was $\varepsilon = 0.05$ and the forcing frequency was $\omega = 200$ . The inverted pendulum shows quasiperiodic response. . . . .	109
4.13	2DOF inverted pendulum under mode 2 vibration. The periodic input forcing amplitude was $\varepsilon = 0.26$ and the forcing frequency was $\omega = 200$ . The inverted pendulum shows near periodic response. . . . .	111
4.14	Phase portrait comparison of periodic solutions on numerical simulation using linear 2DOF inverted pendulum model. From upper left to lower right, the forcing amplitude has ascending values which result in descending frequency ratio. . . . .	112
4.15	Power spectral density comparison of periodic solutions on numerical simulation using linear 2DOF inverted pendulum model. From upper left to lower right, the forcing amplitude has ascending values which result in descending frequency ratio. . . . .	114
5.1	Two degree of freedom inverted pendulum experimental setup. (a)Mode1 vibration. (b)Mode2 vibration. . . . .	117
5.2	NI Vision Builder on two degree of freedom experimental setup. . . . .	119

5.3	Experimental result on 2DOF inverted pendulum under periodic forcing amplitude $\varepsilon = 0.0085 \pm 0.0005$ m and periodic forcing frequency $\omega = 30.0 \pm 0.1$ Hz. System is under mode 1 vibration. (a)periodic forcing (b)pendulum base horizontal movement (c)time traces of system response (d)time traces of system angular velocity (e)time traces zoom-in view of system response (f)time traces zoom-in view of system angular velocity. . . . .	122
5.4	Experimental result on 2DOF inverted pendulum under periodic forcing amplitude $\varepsilon = 0.0085 \pm 0.0005$ m and periodic forcing frequency $\omega = 30.0 \pm 0.1$ Hz. System is under mode 1 vibration. Left graphs indicate the system response of the first pendulum; right graphs indicate the system response of the second pendulum. . . . .	123
5.5	Power spectral density graphs of 2DOF inverted pendulum under periodic forcing amplitude $\varepsilon = 0.0085 \pm 0.0005$ m and periodic forcing frequency $\omega = 30.0 \pm 0.1$ Hz. System is under mode 1 vibration. (a)PSD for the first pendulum (b)PSD for the second pendulum. . . . .	124
5.6	Experimental result on 2DOF inverted pendulum under periodic vertical forcing. The forcing frequency was $\omega = 28.0 \pm 0.1$ Hz. System is under mode 2 vibration. Notice that the input forcing was not harmonic which had two forcing amplitudes involved. . . . .	126
5.7	Experimental result on 2DOF inverted pendulum under periodic vertical forcing. The forcing frequency was $\omega = 28.0 \pm 0.1$ Hz. System is under mode 2 vibration. Left graphs indicate the system response of the first pendulum; right graphs indicate the system response of the second pendulum. . . . .	127
5.8	Power spectral density graphs of 2DOF inverted pendulum under periodic vertical forcing. The forcing frequency was $\omega = 28.0 \pm 0.1$ Hz. System is under mode 2 vibration. (a)PSD for the first pendulum (b)PSD for the second pendulum. . . . .	128
5.9	Experimental result on 2DOF inverted pendulum under periodic vertical forcing with 0 initial condition. The forcing frequency was $\omega = 30.0 \pm 0.1$ Hz. Notice that the input forcing was not harmonic which had two forcing amplitudes involved. . . . .	129
5.10	Experimental result on 2DOF inverted pendulum under periodic vertical forcing with 0 initial condition. The forcing frequency was $\omega = 30.0 \pm 0.1$ Hz. Notice that the input forcing was not harmonic which had two forcing amplitudes involved. . . . .	131

5.11	Power spectral density graphs of 2DOF inverted pendulum under periodic vertical forcing with 0 initial condition. The forcing frequency was $\omega = 30.0 \pm 0.1$ Hz. . . . .	132
6.1	Modified 2DOF model has each pendulum's center of mass offset to a new location different than the pivot point. . . . .	134

# Abstract

A pendulum is statically unstable in its upright inverted state due to the Earth's gravitational attraction which points downward. However, with proper forcing, the pendulum can be stabilized in its upright inverted state. Special interest is on periodic vertical forcing applied to the pendulum's base to stabilize it around the upright inverted equilibrium. Many researchers have studied how to stabilize the system by varying various parameters, in particular its amplitude and frequency. Most have focused on the single degree of freedom inverted pendulum case, which with linear assumption can be described via Mathieu's equation. The system stability can then be characterized by Floquet theory. Our focus is on searching for the periodic solutions inside the linearly stable region of the pendulum's inverted state when the pendulum is under proper periodic forcing. Our research shows that under appropriate excitation by controlling the forcing amplitude and frequency, the pendulum can maintain certain periodic orbits around its inverted state which we characterize in a systematic way.

In this thesis, we applied four different kinds of geometric realizations of the system response: system time traces, system phase portraits, three dimensional views of the system phase portrait as a function of input forcing, and the system's power spectral density diagram. By analyzing these four diagrams simultaneously, we characterize different kinds of multi-frequency periodic behavior around the pendulum's inverted state. To further discuss the effect of the nonlinearity, we applied perturbation techniques using the normalized forcing amplitude as a perturbation parameter to carry out the approximate periodic solutions on a single degree of freedom inverted pendulum nonlinear model.

We also discuss the multiple degree of freedom inverted pendulum system. Both numerical simulation and experiments were performed and detailed comparisons are discussed. Our numerical simulations show close qualitative agreement with experiments.

# Chapter 1

## Inverted Pendulum Dynamics

### 1.1 Introduction

This dissertation discusses the effect of pendulum stabilization around its inverted state under vertical high-frequency periodic forcing. Although, in general, the inverted pendulum's response won't be periodic under periodic forcing, we are interested in characterizing periodic and multi-periodic behavior. Of special interest is the inverted pendulum stabilized in periodic orbits where the system performs multiple frequency nodding behavior as discussed in Acheson [1], [2]. This phenomenon, is also known as 'hovering motion' (refer to Weibel and Baillieul [60]). The system's phase portrait exhibits periodic orbits which are similar to limit cycles to a time-invariant system. In this dissertation, we study the system through four different types of diagrams: system time traces, system phase portraits, three dimensional views of the system phase portrait as a function of input forcing, and the system's power spectral density diagram. First, we discuss the single degree of freedom system showing modeling, numerical simulation and experiments. In later chapters, we extend the

single degree of freedom system to higher degree of freedom cases. Our system response results show close agreement (qualitatively) between numerical simulation and experiments.

Beginning from the single degree of freedom inverted pendulum model under vertical periodic forcing, a set of nonlinear non-autonomous ordinary differential equations were obtained to describe our model. First, we follow those remarkable ancestors in researching the stability in the single degree of freedom inverted pendulum problem such as Acheson [1], [2], Weibel and Baillicul [60], Rand and Morrison [46], [38]. The linearized equation of motion (Mathieu's equation) is shown in early sections of this dissertation. We apply Floquet theory to Mathieu's equation, which is also known as Hill's equation, to obtain the stability diagram through transition curves calculated from Hill's equation. To understand the effect of the nonlinearity, we then apply a two-timing perturbation technique by assigning a (normalized) forcing amplitude  $\epsilon$  as the perturbation parameter. We then carry out analytic solutions from the nonlinear single degree of freedom model. Later, we perform numerical simulations based on the nonlinear single degree of freedom model to obtain periodic solution sets which we characterize using different normalized forcing parameters and initial conditions. Finally, we conducted a sequence of experiments to obtain detailed measurements to compare with our simulation results. Although experimental results show damping effects, which contradict our assumption of energy conservation, for short times and for the purposes of identifying the multi-frequency state, the experiments and simulations matched reasonably well.

Presented in this paper is a way to analyze a dynamic system where the nonlinearity and time-varying properties cannot be neglected. Unlike the well-known simple

pendulum example in classical mechanics, the inverted pendulum doesn't provide the same kind of clockwork regularity which can be properly predicted by the solutions of a simple time invariant linear ordinary differential equation. Furthermore, such regularity in the simple pendulum can be properly modelled by conservation laws where the system is regular back-and-forth swinging motion can be seen from exchanging its potential and kinetic energies. On the other hand, the inverted pendulum needs certain external energy to excite the system to overcome the Earth's gravitational attraction in order to stabilize it in a statically upright state. The periodic excitation to a simple pendulum brings additional complexity to the system and its governing equation of motion usually needs to be treated as non-autonomous, non-conservative and nonlinear. The analysis of such systems is a challenging task because there is no closed-form analytical solution that can be directly applied.

We use a 4th order Runge-Kutta numerical integration technique to get solutions for different initial conditions. By examining the time evolution in its phase portrait, we can find limit cycles under specific driving parameters and initial conditions. In later chapters, we apply singular perturbation techniques to the nonlinear model to derive sequences of asymptotic approximations to get higher order of accuracy to the solution of the inverted pendulum under multi-frequency nodding state which can be compared directly to the numerical integration and experimental results. Perturbation analysis also provides a better understanding of the complex system and stimulated the development of new methods for the numerical solution of the higher order approximations. Experiments were then introduced and compared with the analytical and numerical integration results in detail.

## 1.2 Motivation and Related Early Work on Inverted Pendulum Dynamics

The instability of the pendulum in its inverted state can be removed by applying rapid vertical oscillatory forcing to its pivot point. This phenomenon had been discovered in early 20th century by Stephenson [53] [54] . When placing it initially in its upright state, the inverted pendulum will remain in its upright vertical state without falling over. However, this is not the only stable state when pendulum is inverted. Acheson et al [1] [2] [3] discovered that the pendulum may withstand large initial disturbances when applying appropriate vertical oscillatory forcing with proper driving amplitude and frequency. Under such conditions, the pendulum will oscillate around its upright vertical equilibrium point without falling over. The pendulum becomes trapped in a limit cycle oscillation. This is an interesting phenomenon which can be applied to model many engineering systems undergoing periodic vibrations. Many research papers discuss the oscillations of a driven pendulum. Here are some examples: Blackburn et al [12] studied the stability and Hopf bifurcations in an inverted pendulum; Smith et al [49] investigated the behavior of an inverted pendulum through experimental measurements; Kalmus [25] worked on a driven inverted pendulum experiment using a speaker; Michaelis [36] used an electric jigsaw to drive an inverted pendulum and study its behavior through stroboscopic photos; Acheson et al [1],[2],[3] compared the stability of an inverted pendulum from theoretical models and experimental approaches; Flashner et al [18] studied the bifurcation through the point mapping method. This kind of system has a time-dependent coefficient in a governing differential equation also known as parametric excitation. The physical sense of the parametric excitation is that the stiffness

or moment of inertia in a dynamic system depends on time. This is quite different compared with adding a nonhomogeneous term in the governing differential equation which results from external excitation. Parametric excitation occurs in a wide variety of engineering applications. Here are a few recent applications: Stephan G. et al [51] investigated parametric excitation in high-speed milling applications; Gani [19] studied parametric excitation of stay-cables; Yu realized parametric excitation in a nanowire system using an oscillating electric field; Mennem [35] studied parametrically excited vibrations in spiral bevel geared systems; Kaajakari [26] realized parametric excitation in ultrasonic surface micromachine actuation.

Most analysis methods for time-varying nonlinear dynamic systems are coordinate-based approaches. This dissertation aims to develop a systematic technique to understand and analyze time-varying and, more specifically, time-periodic nonlinear inverted pendulum dynamic systems in a geometric setting. Series expansion methods and averaging theory were two powerful tools used in solving time varying nonlinear differential equations. Vela [64],[65] gives a detailed treatment of the method of averaging and the related theorems that comprise averaging theory which showed how averaging theory may be used to time-dependent differential equations and it can also be applied to nonlinear control theory of underactuated systems. He pointed out that the averaging theory is derived from nonlinear Floquet theory and perturbation theory. Vela's work also shown that nonlinear time-varying control systems can also be given an exponential representation, meaning that all of the intuition and analysis from linear control theory may provide the control engineer with the needed background to construct and analyze stabilizing controllers for nonlinear systems.

Bogoliubov and Mitropolsky [13] cover the same topics, and also give a general algorithm for calculating higher-order averages. The Poincaré map is a powerful tool for visualizing the results from Floquet theory and extending it to the nonlinear regime. Bogoliubov and Mitropolsky were aware that the averaged equations of a time-dependent differential equation gave the Poincaré map, thereby allowing for stability analysis, and also posited that their method was able to recover higher orders of averaging. This method of averaging is known as the Krylov- Bogoliubov-Mitropolsky (KBM) method of averaging. The higher-order methods proposed by Bogoliubov and Mitropolsky have been studied and extended by several researchers as they are the most general and most powerful of the known averaging methods. Averaging theory also includes two-timing methods, which involve fast and slow time scale; only the fast time scale is averaged over. In many cases averaging over multiple dimensions will introduce resonance. There also exist other papers detailing higher-order averaging theory, however they focus on particular classes of time-periodic systems.

## Chapter 2

# Inverted Pendulum Under Periodic Vertical Forcing

### 2.1 Single Degree of Freedom Inverted Pendulum Model

#### Equations of Motion

Consider a simplified single degree of freedom inverted pendulum which consists of a weightless rigid rod with length  $L$ . A point mass  $m$  is mounted on one end of the inverted pendulum and on the other end a frictionless pivot point  $P$  is subjected to periodic vertical forcing with coordinate  $u(t) = \varepsilon \cos \omega t$  measured downward from some fixed point  $O$ . Here  $\varepsilon$  denotes the vertical driving amplitude and  $\omega$  denotes the periodic driving frequency. The whole system is under uniform gravitational field with gravitational acceleration  $g$  pointing downward. The pendulum has angular displacement  $\theta$  measured from the vertical upright position (inverted state) as shown in Figure 2.1. Here we neglect the effect of damping in

order to apply the energy conservation property by means of Lagrange's equations. The equations of motion can be derived from the general form of Lagrange's equations as

$$\frac{d}{dt} \left( \frac{\partial T}{\partial \dot{\theta}} \right) - \frac{\partial T}{\partial \theta} + \frac{\partial V}{\partial \theta} = \Theta \quad (2.1)$$

$$\frac{d}{dt} \left( \frac{\partial T}{\partial \dot{u}} \right) - \frac{\partial T}{\partial u} + \frac{\partial V}{\partial u} = U \quad (2.2)$$

where  $T$  is the kinetic energy,  $V$  is the potential energy and  $\Theta$  and  $U$  are generalized nonconservative forces with respect to  $\theta$  and  $u$  direction respectively. Since the vertical driving vibration is the only source of nonconservative forces, the right hand side of equations (2.1) and (2.2) can be written as

$$\Theta = 0, U = F. \quad (2.3)$$

From the energy conservation law, (2.1) indicates the energy exchange between kinetic energy and system potential due to the rotational motion of the pendulum; (2.2) indicates the balance of vertical periodic forcing and system energy transfer between kinetic energy and potential energy due to the applied force. The kinetic energy can be derived as

$$\begin{aligned} T &= \frac{1}{2}m(v_x^2 + v_y^2) \\ &= \frac{1}{2}m \left[ (L\dot{\theta} \cos \theta)^2 + (\dot{u} + L\dot{\theta} \sin \theta)^2 \right] \\ &= \frac{1}{2}m \left( L^2\dot{\theta}^2 + 2L\dot{u}\dot{\theta} \sin \theta + \dot{u}^2 \right) \end{aligned} \quad (2.4)$$

where  $v_x$  is horizontal velocity vector and  $v_y$  is vertical velocity vector of the point mass as shown in Figure 2.1. The potential energy  $V$  depends on the vertical displacement  $\Delta y$

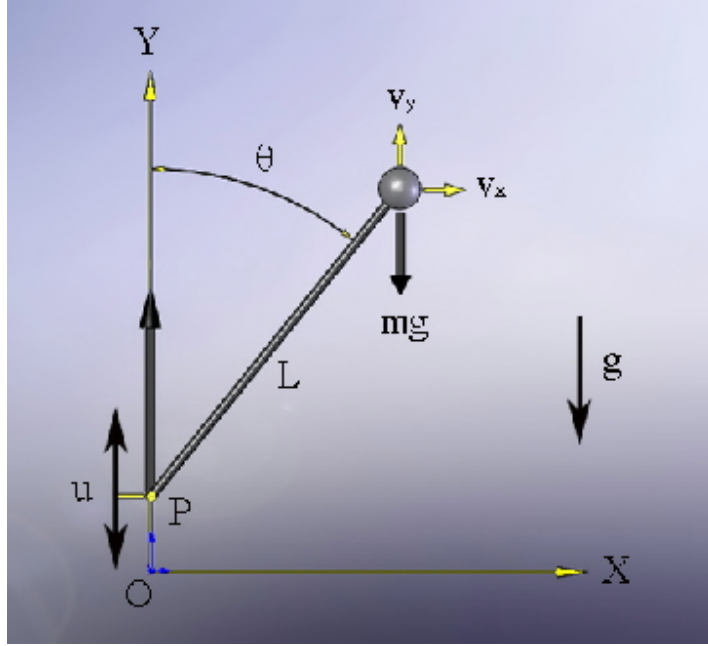


Figure 2.1: Single degree of freedom inverted pendulum under vertical periodic forcing at its base  $P$ .

which can be written as

$$V = mg\Delta y = mg[L(1 + \cos \theta) + u]. \quad (2.5)$$

As indicated in (2.5), the system potential only depends on the posture of the pendulum at that instance, not its motion. In other words,  $V$  is not a function of  $\dot{\theta}$  or  $\dot{u}$ . We can then calculate individual components of (2.1) from derivatives of (2.4) and (2.5) as

$$\begin{aligned} \frac{\partial T}{\partial \dot{\theta}} &= mL^2\dot{\theta} + mL\dot{u} \sin \theta \\ \frac{d}{dt} \left( \frac{\partial T}{\partial \dot{\theta}} \right) &= mL^2\ddot{\theta} + mL(\ddot{u} \sin \theta + \dot{u}\dot{\theta} \cos \theta) \\ \frac{\partial T}{\partial \dot{u}} &= mL\dot{\theta} \cos \theta \\ \frac{\partial V}{\partial \theta} &= -mgL \sin \theta \end{aligned} \quad (2.6)$$

From derivatives of (2.4) and (2.5) to individual components of (2.2) we get

$$\begin{aligned}
\frac{\partial T}{\partial \dot{u}} &= m \left( L\dot{\theta} \sin \theta + \dot{u} \right) \\
\frac{d}{dt} \left( \frac{\partial T}{\partial \dot{u}} \right) &= m \left( L\ddot{\theta} \sin \theta + L\dot{\theta}^2 \cos \theta + \ddot{u} \right) \\
\frac{\partial T}{\partial u} &= 0 \\
\frac{\partial V}{\partial u} &= mg
\end{aligned} \tag{2.7}$$

Hence, substitute (2.6) and (2.7) into (2.1) and (2.2), we obtain the explicit Lagrange's equations as

$$mL^2\ddot{\theta} + mL\ddot{u} \sin \theta - mgL \sin \theta = 0, \tag{2.8}$$

$$m \left( L\ddot{\theta} \sin \theta + L\dot{\theta}^2 \cos \theta + \ddot{u} \right) + mg = F. \tag{2.9}$$

From time derivatives to the driving displacement  $u$ , we obtain it's velocity as  $\dot{u} = -\varepsilon\omega \sin \omega t$ . From second time derivatives to  $u$ , we obtain it's acceleration as

$$\ddot{u} = \varepsilon\omega^2 \cos \omega t. \tag{2.10}$$

The simplified equation of motion of the single degree of freedom inverted pendulum model under vertical vibration can then be obtained by inserting (2.10) into (2.8) as

$$mL^2\ddot{\theta} - (mgL + mL\varepsilon\omega^2 \cos \omega t) \sin \theta = 0. \tag{2.11}$$

Equation (2.11) is a nonlinear differential equation with a time-dependent coefficient. By dividing both sides of (2.11) by  $mL^2$  we obtain

$$\ddot{\theta} - \left( \frac{g}{L} + \frac{\varepsilon\omega^2}{L} \cos \omega t \right) \sin \theta = 0. \quad (2.12)$$

Unlike the simple pendulum case whose state coefficient is constant, our system has a time-varying coefficient due to driving forces. When the driving acceleration amplitude is smaller than gravity,  $\varepsilon\omega^2 < g$ , the system coefficient,  $\frac{g}{L} + \frac{\varepsilon\omega^2}{L} \cos \omega t$ , doesn't change sign and the system response has little effect due to forcing. Based on linear theory, the state is said to be hyperbolic since the eigenvalues of the Jacobian matrix around the equilibrium points do not lie on the imaginary axis. In this case, the nonlinear behavior can be properly predicted through linear analysis around its equilibrium points. On the other hand, when the driving acceleration amplitude is larger than gravity,  $\varepsilon\omega^2 > g$ , the system coefficient changes sign. In this case, the equilibrium point will change from hyperbolic to non-hyperbolic since the eigenvalues of the Jacobian matrix around its equilibrium points will sometimes lie on the imaginary axis.

**Definition 1** *For a continuous-time system, an equilibrium is called non-hyperbolic if the Jacobian matrix evaluated at the equilibrium point has at least one eigenvalue with zero real part. In other words, if there is any eigenvalue located on the imaginary axis then the system is non-hyperbolic. For a discrete-time system a fixed point is called non-hyperbolic if the Jacobian matrix evaluated at the fixed point has at least one multipliers located on the unit circle.*

The nonlinear behavior of a hyperbolic system can be properly predicted from its

linearized counterparts. The Hartman-Grobman theorem states that the local phase portrait near a hyperbolic equilibrium point of the nonlinear system is topologically equivalent to the phase portrait of its linearization. One important consequence is the stability type of the equilibrium point of the nonlinear system is preserved by its linearization. However, if the system is non-hyperbolic, the theorem does not hold. In this paper, we are exclusively discussing the effect of driving acceleration amplitude much larger than gravity or  $\varepsilon\omega^2 \gg g$  which will excite the pendulum to stabilize at its inverted state and such a system usually is non-hyperbolic. Acheson [3],[1] shows that the pendulum can be stabilized in its inverted state only when  $\varepsilon^2\omega^2 > 2gL$  which guarantees  $\varepsilon\omega^2 \gg g$  under small driving amplitude  $\varepsilon$ . Our experimental results also show that a driving acceleration of about  $30G \sim 50G$  is required for a single degree of freedom pendulum to stabilize its inverted state, i.e.  $\varepsilon\omega^2$  needs to be 30 to 50 times larger than  $g$ .

The analysis of time-varying, nonautonomous nonlinear systems is a challenging task. The time-varying coefficient or parametric excitation of (2.12) plays a big role in contributing to the response of the system when the driving acceleration is much larger than the gravitational acceleration, or  $\varepsilon\omega^2 \gg g$ . When the frequency of excitation is sufficiently far from the primary resonance, a small parametric excitation can produce a large response. This time-varying property makes the system difficult to solve analytically and the system response is highly dependent on the initial conditions. However, the system response can be simplified if we limit the time-varying parameters to be time-periodic. With time-periodic parametric excitation, there may exist periodic solutions (from averaging theory) if the system initial conditions are selected properly. Averaging theory is a technique

which synthesizes Floquet theory and perturbation theory by applying series expansions to approximate time-varying vector fields [64], [65]. In the next section, we apply averaging theory to a linear single degree of freedom inverted pendulum system by means of Floquet theory and series expansion through system perturbation parameter. System stability can be shown using transition curves and Stutt's diagram.

### Linearized $s$ DOF Model and Mathieu's Equation

When using the small angle assumption,  $\sin \theta \rightarrow \theta$ , the original nonlinear single degree of freedom inverted pendulum equation of motion (2.12) can be linearized as

$$\ddot{\theta} - \left( \frac{g}{L} + \frac{\varepsilon \omega^2}{L} \cos \omega t \right) \theta = 0. \quad (2.13)$$

Equation (2.13) is then transformed to well-known Mathieu's equation

$$\frac{d^2 \theta}{d\tau^2} + (\delta + \epsilon \cos \tau) \theta = 0. \quad (2.14)$$

Here, the first system parameter  $\delta = -\left(\frac{\omega_n}{\omega}\right)^2$  is defined as negative value of the square of the ratio of the system natural frequency  $\omega_n = \sqrt{\frac{g}{L}}$  and the driving frequency  $\omega$ . The second system parameter  $\epsilon = \frac{\varepsilon}{L}$  is defined as normalized driving amplitude. Equation (2.14) has new system time defined as  $\tau = \omega t$ .

### Primary Resonance of the Transition Curves of Mathieu's Equation

Apply the 2-timing perturbation technique by introducing two new variables: fast time  $\xi = \tau$  and slow time  $\eta = \varepsilon \tau$  to (2.14). The system's state is then translated into  $\theta(\tau) \mapsto \theta(\xi, \eta)$  and its derivatives can be carried out using chain rule as follows:

$$\dot{\theta} = \frac{d\theta}{d\tau} = \frac{\partial\theta}{\partial\xi} \frac{d\xi}{d\tau} + \frac{\partial\theta}{\partial\eta} \frac{d\eta}{d\tau} = \frac{\partial\theta}{\partial\xi} + \epsilon \frac{\partial\theta}{\partial\eta}, \quad (2.15)$$

$$\ddot{\theta} = \frac{d^2\theta}{d\tau^2} = \frac{\partial^2\theta}{\partial\xi^2} + 2\epsilon \frac{\partial^2\theta}{\partial\xi\partial\eta} + \epsilon^2 \frac{\partial^2\theta}{\partial\eta^2}. \quad (2.16)$$

Substitute (2.16) into (2.14),

$$\frac{\partial^2\theta}{\partial\xi^2} + 2\epsilon \frac{\partial^2\theta}{\partial\xi\partial\eta} + \epsilon^2 \frac{\partial^2\theta}{\partial\eta^2} + (\delta + \epsilon \cos \xi) \theta = 0. \quad (2.17)$$

An approximate solution of (2.14) can be obtained from expanding  $\theta$  in a power series for small  $\epsilon$  as:

$$\theta(\xi, \eta) = \theta_0(\xi, \eta) + \epsilon\theta_1(\xi, \eta) + \epsilon^2\theta_2(\xi, \eta) + \dots \quad (2.18)$$

Substituting (2.18) into (2.17) and neglecting higher order terms of  $O(\epsilon^2)$  we get

$$\frac{\partial^2(\theta_0 + \epsilon\theta_1)}{\partial\xi^2} + 2\epsilon \frac{\partial^2(\theta_0 + \epsilon\theta_1)}{\partial\xi\partial\eta} + \epsilon^2 \frac{\partial^2(\theta_0 + \epsilon\theta_1)}{\partial\eta^2} + (\delta + \epsilon \cos \xi)(\theta_0 + \epsilon\theta_1) = 0 \quad (2.19)$$

Collect terms of the same orders of  $\epsilon$ :

$$\frac{\partial^2\theta_0}{\partial\xi^2} + \delta\theta_0 = 0, \quad (2.20)$$

$$\frac{\partial^2\theta_1}{\partial\xi^2} + \delta\theta_1 = -2 \frac{\partial^2\theta_0}{\partial\xi\partial\eta} - \theta_0 \cos \xi. \quad (2.21)$$

The general solution to (2.20) can be expressed as

$$\theta_0(\xi, \eta) = A(\eta) \cos \sqrt{\delta}\xi + B(\eta) \sin \sqrt{\delta}\xi. \quad (2.22)$$

Differentiating to (2.22) with respect to  $\xi$  and  $\eta$  we have

$$\frac{\partial^2\theta_0}{\partial\xi\partial\eta} = -\sqrt{\delta} \frac{dA(\eta)}{d\eta} \sin \sqrt{\delta}\xi + \sqrt{\delta} \frac{dB(\eta)}{d\eta} \cos \sqrt{\delta}\xi. \quad (2.23)$$

Substituting (2.22) and (2.23) into (2.21) , we then obtain

$$\begin{aligned} \frac{\partial^2 \theta_1}{\partial \xi^2} + \delta \theta_1 &= -2 \left( -\sqrt{\delta} \frac{dA(\eta)}{d\eta} \sin \sqrt{\delta} \xi + \sqrt{\delta} \frac{dB(\eta)}{d\eta} \cos \sqrt{\delta} \xi \right) \\ &\quad - \left( A(\eta) \cos \sqrt{\delta} \xi + B(\eta) \sin \sqrt{\delta} \xi \right) \cos \xi. \end{aligned} \quad (2.24)$$

Apply the following trigonometric identities to simplify (2.24)

$$\sin \alpha \cos \beta = \frac{1}{2} (\sin (\alpha + \beta) - \sin (\alpha - \beta)), \quad (2.25)$$

$$\cos \alpha \cos \beta = \frac{1}{2} (\cos (\alpha + \beta) + \cos (\alpha - \beta)), \quad (2.26)$$

where  $\alpha, \beta$  are dummy variables. Substitute (2.25) and (2.26) using proper variables in (2.24) to replace  $\alpha$  and  $\beta$  we obtain

$$\begin{aligned} \frac{\partial^2 \theta_1}{\partial \xi^2} + \delta \theta_1 &= 2\sqrt{\delta} \frac{dA(\eta)}{d\eta} \sin \sqrt{\delta} \xi - 2\sqrt{\delta} \frac{dB(\eta)}{d\eta} \cos \sqrt{\delta} \xi \\ &\quad - \frac{A(\eta)}{2} \left( \cos \left( \sqrt{\delta} + 1 \right) \xi + \cos \left( \sqrt{\delta} - 1 \right) \xi \right) \\ &\quad - \frac{B(\eta)}{2} \left( \sin \left( \sqrt{\delta} + 1 \right) \xi - \sin \left( \sqrt{\delta} - 1 \right) \xi \right). \end{aligned} \quad (2.27)$$

For general values of  $\delta$ , removal of resonance terms require the coefficients of  $\sin \sqrt{\delta} \xi$  and  $\cos \sqrt{\delta} \xi$  become zero which gives the trivial solutions as:

$$\frac{dA(\eta)}{d\eta} = 0, \quad (2.28)$$

$$\frac{dB(\eta)}{d\eta} = 0. \quad (2.29)$$

This means that for general  $\delta$ , the  $\cos \omega t$  driving term in Mathieu's equation (2.14) has no effect. However, if we choose  $\delta = \frac{1}{4}$  and substitute into (2.27) we get

$$\frac{\partial^2 \theta_1}{\partial \xi^2} + \frac{1}{4} \theta_1 = \frac{dA(\eta)}{d\eta} \sin \frac{\xi}{2} - \frac{dB(\eta)}{d\eta} \cos \frac{\xi}{2} - \frac{A(\eta)}{2} \left( \cos \frac{3\xi}{2} + \cos \frac{\xi}{2} \right) - \frac{B(\eta)}{2} \left( \sin \frac{3\xi}{2} - \sin \frac{\xi}{2} \right). \quad (2.30)$$

From analyzing the right-hand side of (2.30), the removal of resonance terms gives the following solutions:

$$\frac{dA(\eta)}{d\eta} = -\frac{B(\eta)}{2}, \quad (2.31)$$

$$\frac{dB(\eta)}{d\eta} = -\frac{A(\eta)}{2}. \quad (2.32)$$

We may also rewrite (2.31) and (2.32) in matrix form as

$$\begin{bmatrix} \frac{dA(\eta)}{d\eta} \\ \frac{dB(\eta)}{d\eta} \end{bmatrix} = \begin{bmatrix} 0 & -\frac{1}{2} \\ -\frac{1}{2} & 0 \end{bmatrix} \begin{bmatrix} A(\eta) \\ B(\eta) \end{bmatrix}. \quad (2.33)$$

Combine (2.31) and (2.32) to obtain

$$\frac{d^2 A(\eta)}{d\eta^2} = \frac{A(\eta)}{4}. \quad (2.34)$$

Here  $A(\eta)$  and  $B(\eta)$  involve exponential growth where the instability occurs when  $\delta = \frac{1}{4}$ .

This corresponds to a 2 : 1 subharmonic resonance in which the driving frequency is twice the natural frequency [38]. By expanding  $\delta$  in a power series in  $\epsilon$  we may get a  $\delta - \epsilon$  curve due to resonance excitation in more generalized way as

$$\delta = \frac{1}{4} + \delta_1 \epsilon + \delta_2 \epsilon^2 + \dots \quad (2.35)$$

Substitute (2.35) into (2.19) and neglecting terms of  $O(\epsilon^2)$  we get

$$\frac{\partial^2 (\theta_0 + \epsilon\theta_1)}{\partial \xi^2} + 2\epsilon \frac{\partial^2 (\theta_0 + \epsilon\theta_1)}{\partial \xi \partial \eta} + \epsilon^2 \frac{\partial^2 (\theta_0 + \epsilon\theta_1)}{\partial \eta^2} + \left( \frac{1}{4} + \delta_1 \epsilon + \epsilon \cos \xi \right) (\theta_0 + \epsilon\theta_1) = 0. \quad (2.36)$$

Collect terms of the same  $\epsilon$  orders, yields

$$\frac{\partial^2 \theta_0}{\partial \xi^2} + \frac{1}{4} \theta_0 = 0, \quad (2.37)$$

$$\frac{\partial^2 \theta_1}{\partial \xi^2} + \frac{1}{4} \theta_1 = -2 \frac{\partial^2 \theta_0}{\partial \xi \partial \eta} - \theta_0 \cos \xi - \delta_1 \theta_0, \quad (2.38)$$

which results in the following additional terms in (2.31) and (2.32) as

$$\frac{dA(\eta)}{d\eta} = \left( \delta_1 - \frac{1}{2} \right) B(\eta), \quad (2.39)$$

$$\frac{dB(\eta)}{d\eta} = - \left( \delta_1 + \frac{1}{2} \right) A(\eta). \quad (2.40)$$

We may also rewrite (2.39) and (2.40) in matrix form as

$$\begin{bmatrix} \frac{dA(\eta)}{d\eta} \\ \frac{dB(\eta)}{d\eta} \end{bmatrix} = \begin{bmatrix} 0 & \delta_1 - \frac{1}{2} \\ -(\delta_1 + \frac{1}{2}) & 0 \end{bmatrix} \begin{bmatrix} A(\eta) \\ B(\eta) \end{bmatrix}, \quad (2.41)$$

Comparing with (2.34), an additional term is introduced

$$\frac{d^2 A(\eta)}{d\eta^2} + \left( \delta_1^2 - \frac{1}{4} \right) A(\eta) = 0. \quad (2.42)$$

From (2.42) we may conclude that if  $\delta_1^2 - \frac{1}{4} > 0$ , that is, if either  $\delta_1 > \frac{1}{2}$  or  $\delta_1 < -\frac{1}{2}$ , then  $A(\eta)$  and  $B(\eta)$  will be sine and cosine function of slow time  $\eta$ . We may substitute boundary values of  $\delta_1$  into (2.35), which yields

$$\delta = \frac{1}{4} \pm \frac{\epsilon}{2} + O(\epsilon^2). \quad (2.43)$$

There are two curves described in (2.43), starting from the point  $\delta = \frac{1}{4}$  on the  $\delta$  axis in  $\delta - \epsilon$  plane. These are recognized as primary resonances of the transition curves [46]. Transition curves as in Figure 2.2 represent stability changes, region in between of these two curves is unstable. Inside the unstable region, for small  $\epsilon$ ,  $\theta$  grows exponentially in time and the solution is unbounded. Outside the unstable region, from (2.22), (2.39), (2.40) and (2.42),  $\theta$  is the sum of terms each of which is the product of two periodic or harmonic functions and  $\theta$  is bounded, specifically,  $\theta(t)$  is a quasiperiodic function of time.

### Floquet Theory

Because the time-varying coefficient in Mathieu's equation (2.14) is periodic in time, we may apply Floquet theory to simplify the system. Floquet theory is concerned with the following system of first order differential equations:

$$\frac{dx}{dt} = A(t)x, \quad (2.44)$$

where  $x$  is an  $n \times 1$  column vector, and  $A$  is an  $n \times n$  time-periodic coefficients matrix with period  $T$  with the following property:

$$A(t + T) = A(t). \quad (2.45)$$

Although  $A(t)$  varies periodically in time, the general solutions of (2.44) are typically not periodic. Floquet theory indicates that there exists a fundamental matrix solution  $\Phi_{0,t}^A$  of (2.44) of the form

$$\Phi_{0,t}^A = P(t) \exp(\mu t), \quad (2.46)$$

where  $P(t)$  is period in time  $P(t+T) = P(t)$ , and  $\mu$  is in general a complex number. The general solution of (2.44) takes the following form:

$$x(t) = \sum_i^n C_i \exp(\mu_i t) P_i(t) \quad (2.47)$$

where  $C_i$  are constants that depend only on initial conditions  $x(t_0) = x_0$ . They take the following form:

$$C = (\Phi_{0,t_0}^A)^{-1} x_0.$$

$P_i(t)$  in (2.47) are vector-valued functions which are also periodic in time with period  $T$ , and  $\mu_i$  are complex numbers known as Floquet exponents. The Floquet multipliers can be defined as

$$\rho_i = \exp(\mu_i T). \quad (2.48)$$

The Floquet exponents are not unique since  $\exp(\mu_i + \frac{2\pi ik}{T}) T = \exp(\mu_i T)$  for any integer value  $k$ . Furthermore, the long-term behavior of the solution of  $x(t)$  is determined by the Floquet exponents. Floquet theory allows us to reach an important conclusion about the solution's stability. If any of the Floquet multipliers have modulus greater than unity, i.e.  $|\rho_i| > 1$ , then  $x(t)$  is unbounded as  $t \rightarrow \infty$  and the system becomes unstable. On the other hand, if all Floquet multipliers have modulus less than unity, i.e.  $|\rho_i| < 1$ , then  $x(t)$  is bounded as  $t \rightarrow \infty$  and the system is stable. The Floquet exponents and Floquet multipliers represent the growth rate of different perturbations averaged over a cycle. Floquet exponents are rates with unit  $t^{-1}$  and Floquet multipliers are dimensionless numbers that give the period to period increase or decrease of the perturbation.

Floquet theory can be applied to a generalized Mathieu equation (also known as Hill's equation [46]) which takes the following form:

$$\begin{aligned}\frac{d^2x}{dt^2} + f(t)x &= 0, \\ f(t+T) &= f(t).\end{aligned}\tag{2.49}$$

Here  $x$  and  $f$  are scalars, and  $f(t)$  represents a general periodic function with period  $T$ .

The second order ordinary differential equation in (2.49) can be transferred into a system of two first order o.d.e's by defining  $x_1 = x$  and  $x_2 = \dot{x}$  and then substitute into (2.49) yields

$$\begin{bmatrix} \dot{x}_1 \\ \dot{x}_2 \end{bmatrix} = \begin{bmatrix} 0 & 1 \\ -f(t) & 0 \end{bmatrix} \begin{bmatrix} x_1 \\ x_2 \end{bmatrix}.\tag{2.50}$$

Two fundamental solutions can then be constructed as  $\begin{bmatrix} x_{11}(t) \\ x_{12}(t) \end{bmatrix}$  and  $\begin{bmatrix} x_{21}(t) \\ x_{22}(t) \end{bmatrix}$  which

satisfy the initial conditions  $\begin{bmatrix} x_{11}(0) \\ x_{12}(0) \end{bmatrix} = \begin{bmatrix} 1 \\ 0 \end{bmatrix}$  and  $\begin{bmatrix} x_{21}(0) \\ x_{22}(0) \end{bmatrix} = \begin{bmatrix} 0 \\ 1 \end{bmatrix}$  respectively.

We can then construct a matrix  $C$  which is the fundamental solution matrix evaluated at time  $T$

$$C = \begin{bmatrix} x_{11}(T) & x_{12}(T) \\ x_{21}(T) & x_{22}(T) \end{bmatrix}.\tag{2.51}$$

From Floquet theory, we may conclude that the system stability is determined by the eigenvalues of  $C$ . If all eigenvalues of  $C$  have modulus less than unity, the system's solution will be bounded and the system is stable; if any eigenvalue of  $C$  is greater than unity, the system's solution will grow exponential in time and the system is unstable. The eigenvalues of  $C$  can be written as

$$\lambda^2 - \text{tr}(C)\lambda + \det(C) = 0,\tag{2.52}$$

where  $tr(C)$  denotes the trace of  $C$  which defines as  $tr(C) = x_{11}(T) + x_{22}(T)$  and  $\det(C)$  denotes the determinant of  $C$  which defines as  $\det(C) = x_{11}(T)x_{22}(T) - x_{12}(T)x_{21}(T)$ . The Hill's equation (2.49) has a special property that its determinant has value equal to one, i.e.  $\det(C) = 1$ . Due to this special property, (2.52) becomes

$$\lambda^2 - tr(C)\lambda + 1 = 0, \quad (2.53)$$

and the eigenvalue  $\lambda$  has solution

$$\lambda = \frac{tr(C) \pm \sqrt{(tr(C))^2 - 4}}{2}. \quad (2.54)$$

Therefore, the eigenvalue has real roots when  $|tr(C)| > 2$  and the eigenvalues have a pair of complex conjugate roots when  $|tr(C)| < 2$ . Another special property is the product of the eigenvalues must equal to unity. Thus, in the case of two real roots, if one root is less than unity then the other root must be larger than unity which results in instability. There are two stable conditions for two real roots case which can be obtained when  $|tr(C)| = 2$ . If  $tr(C) = 2$  then two real eigenvalues are  $\lambda_{1,2} = 1, 1$  and according to Floquet theory, this condition corresponds to a periodic solution with period  $T$ . If  $tr(C) = -2$  then two real eigenvalues are  $\lambda_{1,2} = 1, -1$  and according to Floquet theory this condition corresponds to a periodic solution with period  $2T$ . On the other hand, in the case of a pair of complex conjugate roots, both eigenvalues must lie on the unit circle. We can conclude this condition as neutral stability and the system has quasiperiodic solution. All stable conditions in Hill's equation have eigenvalues which lie on the unit circle. Such a system is non-hyperbolic.

Since Hill's equation has no damping effect and its stable conditions are non-hyperbolic, it allows us to make conclusions about long time behavior using the solution

form merely one forcing period. Full transition curves can be carried out using the harmonic balance technique by applying the fact that the period of the forcing function in Mathieu's equation (2.14) is  $2\pi$  periodic, i.e.  $T = 2\pi$ . Detail discussion about Hill's equation and harmonic balance is shown in Rand [46].

### **Transition Curves of Mathieu's Equation: Strutt's Diagram**

The transition curves on the  $\delta - \epsilon$  plane also known as Strutt's diagram is shown in Figure 2.2. The transition curves were obtained by applying Floquet theory to linear Mathieu's equation and then applying the harmonic balance technique. Refer to the Appendix at the end of this paper for a listing of the complete sets of transition curves derived by Rand [46].

In Figure 2.2, the region of  $\delta > 0$  denotes the pendulum has downward vertical equilibrium where inside the bounded region(shaded area) the pendulum will be trapped around its downward vertical position(normal state); the region of  $\delta < 0$  denotes the pendulum has upright vertical equilibrium where inside the bounded region(shaded area) the pendulum will be trapped around its upright vertical position(inverted state). The unbounded region between the two transition curves were obtained through resonance excitation, starting from

$$\delta = \frac{n^2}{4}, n = 0, 1, 2, 3... \quad (2.55)$$

for small  $\epsilon$ . The unbounded region from the starting point  $\delta = \frac{1}{4}$  at  $n = 1$  is called the primary resonance and its transition curves were calculated from (2.43). The unbounded region under primary resonance has the largest area. As  $n$  value increases, the unbounded region moves to the right hand side of the primary resonance and its covering area becomes

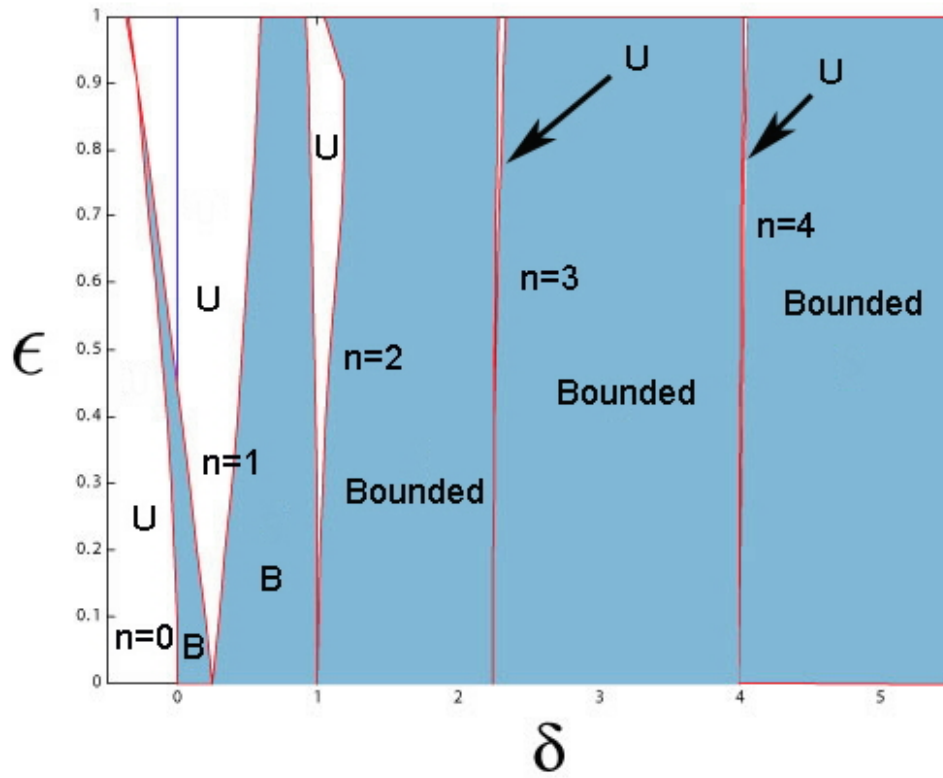


Figure 2.2: Transition curves for the linear Mathieu equation on the  $\delta - \epsilon$  plane separate regions of bounded solution (shaded area) from regions of unbounded solution or unstable system (white area).

smaller. We only discuss the region of  $\delta < 0$  when the pendulum has upright vertical equilibrium. In other words, our special interest focuses on the bounded region (shaded area) of  $\delta < 0$  covered in between the two transition curves of  $n = 0$  and  $n = 1$ . Figure 2.3 shows the zoom-in view of Figure 2.2 where  $\delta < 0$  region being emphasized. Recall that in our inverted pendulum model (2.14)  $\delta$  was defined as negative value of the square of the ratio of the system natural frequency and the driving frequency which takes the following equation:  $\delta = -\left(\frac{\omega_n}{\omega}\right)^2$ . If system's natural frequency remain fixed then the higher the forcing frequency  $\omega$ , the closer  $\delta$  approaches 0. There are 3 regions labelled  $A, B, C$  in Figure 2.3 which indicates our region of interest in our single degree of freedom inverted pendulum model. These regions are in relative higher forcing frequency region ( $> 25$  Hz) where  $\delta$  is close to 0. In our simulation trials, we fixed the forcing frequency while varying the forcing amplitude gradually from  $A$  to  $B$  then to  $C$  regions. Our main focus is on  $B$  region where the pendulum is stabilized in its inverted state, while  $A$  and  $C$  regions are only to test stability boundaries.

Another way to present the stability boundaries on a graph of an inverted pendulum under periodic forcing is to graph the stability region in the  $\epsilon - \bar{\omega}$  plane as in Figure 2.4. The shaded area in Figure 2.4 indicates the results from Acheson and Mullin [3] which showed the stability boundaries calculated from solving linear Mathieu's equation. Inside the shaded region, the pendulum can be stabilized around its inverted posture where the system has bounded solutions. On the other hand, the region outside the shaded region has unbounded solutions. Left ( $n = 0$ , blue-color curve) and right ( $n = 1$ , green-color curve) transition curves in  $\epsilon - \bar{\omega}$  stability diagram in Figure 2.4 show the stability boundaries of our

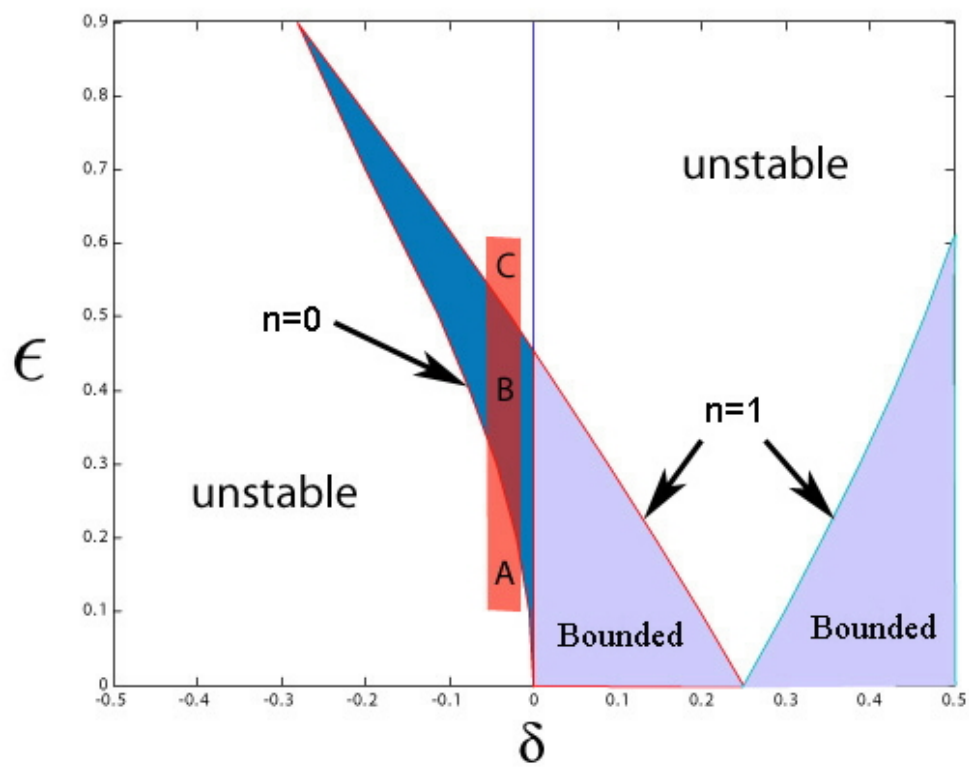


Figure 2.3: Stutt's diagram for stability regions separated by the transition curves of  $n = 0$  and  $n = 1$  within the range of  $-0.5 < \delta < 0.5$ .

calculations matched with the results from Acheson and Mullin [3]. These two transition curves are the same curves as shown in Figure 2.3 inside  $\delta < 0$  region. The left stability limit curve described by  $\varepsilon^2\omega^2 = 2gL$  was calculated from Acheson [1] which showed more conservative stability region compared with the left transition curve( $n = 0$ ). This left stability curve(red-color) is very close to the left transition curve(blue-color) as shown in Figure 2.4. Those green-color data points denote the experimental results from Acheson and Mullin [3] which show the stability boundary from their experimentations were even wider than their prediction from solving linear  $s$ DOF inverted pendulum model. This can be explained by the effect of system damping due to friction in their experimental setups. In other words, system damping helps the system's stability in this case.

There are three sets of diamond data points in Figure 2.4, indicating 3 sets of periodic solutions from our numerical simulations to the nonlinear single degree of freedom inverted pendulum model. Basically, these diamond data points indicate the stability boundaries and periodic solutions to the same single degree of freedom inverted pendulum model where we fixed the normalized forcing frequency  $\bar{\omega}$  at three locations:  $\bar{\omega} = 11.6218, \bar{\omega} = 14.2784$ , and  $\bar{\omega} = 20.0$ , while we varied normalized forcing amplitude  $\varepsilon$  from small to large values. Our simulation results showed that the left limit was located on the left transition curve, while the right limit was wider than the right transition curve. The periodic solutions were discovered in numerical simulation inside the stable region in Figure 2.4 labelled as  $4 : 1, 5 : 1, 6 : 1, \dots$ , where the ratio indicates the forcing period with respect to system's periodic response. We denoted this ratio as frequency ratio  $N_r$  whose detail will be shown in later chapters. The set of data points in blue-color circles

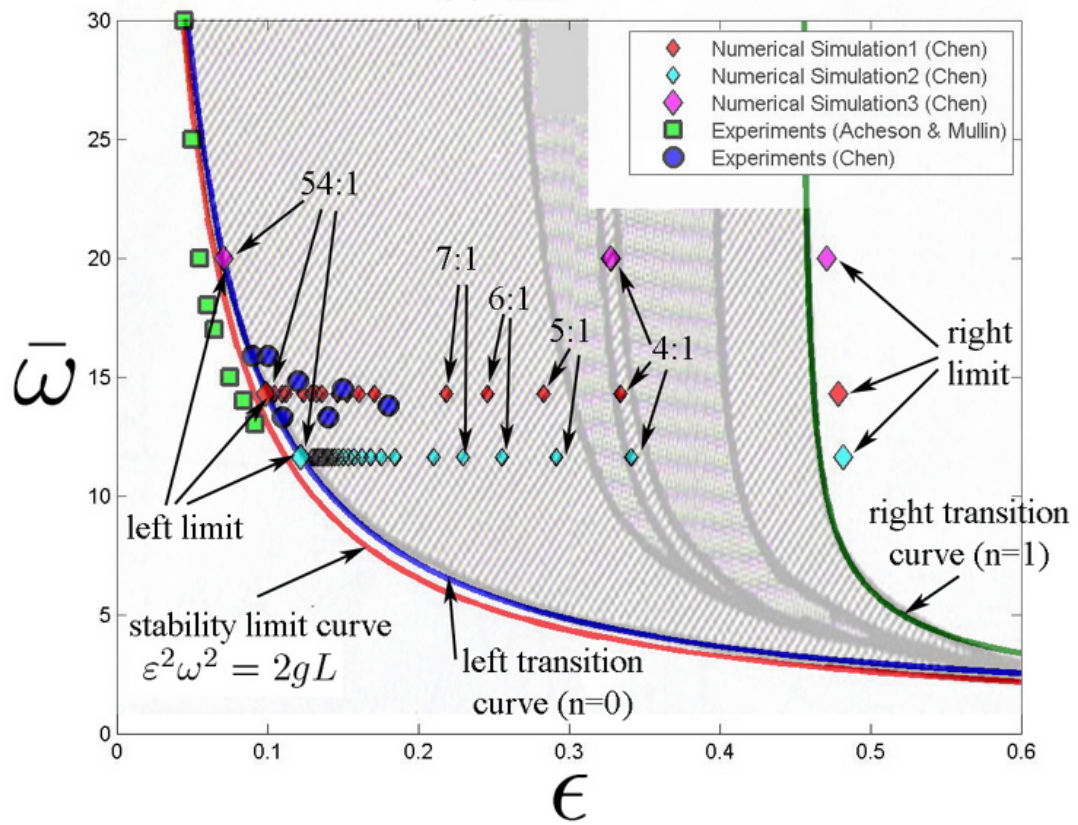


Figure 2.4: Stability regime diagram of single degree of freedom inverted pendulum under vertical periodic forcing showing in the  $\epsilon - \bar{\omega}$  plane.

indicates the parameter distributions of our single degree of freedom inverted pendulum experiments. Due to physical limitations of our experimental setups, experimental data only occupied the region of normalized forcing amplitude  $\epsilon < 0.2$  and normalized forcing frequency  $10 \leq \bar{\omega} \leq 20$ . More details of Figure 2.4 will be shown in later sections in this paper.

### **Numerical Integration of the Nonlinear $s$ DOF Inverted Pendulum Model Simulation Based on Parameter Continuation Code Using 4<sup>th</sup> Order Runge-Kutta Numerical Integration Scheme**

This section discusses the simulations from direct numerical integration of the time-varying single degree of freedom inverted pendulum model. We normalized the  $s$ DOF model by substituting the normalized driving amplitude  $\epsilon$  and normalized driving frequency  $\bar{\omega}$  into (2.12). The normalized driving amplitude  $\epsilon$  is defined as  $\epsilon = \frac{\varepsilon}{L}$  and normalized driving frequency is defined as  $\bar{\omega} = \frac{\omega}{\omega_n}$ , where the system natural frequency is  $\omega_n = \sqrt{\frac{g}{L}}$ . Therefore, (2.12) can be expressed as:

$$\ddot{\theta}(t) - (1 + \epsilon\bar{\omega}^2 \cos \omega t) \omega_n^2 \sin \theta(t) = 0. \quad (2.56)$$

The original 2<sup>nd</sup> order system equation can then be re-written as two 1<sup>st</sup> order equations

$$\begin{aligned} \dot{x}_1 &= x_2, \\ \dot{x}_2 &= (1 + \epsilon\bar{\omega}^2 \cos \omega t) \omega_n^2 \sin x_1. \end{aligned} \quad (2.57)$$

where  $x_1 = \theta$ , and  $x_2 = \dot{\theta}$ . The natural frequency of the system is  $\omega_n = \sqrt{\frac{g}{L}}$ , the normalized driving amplitude is  $\epsilon = \frac{\varepsilon}{L}$ , and the normalized driving frequency is  $\bar{\omega} = \frac{\omega}{\omega_n}$ .

The periodic forcing in the system can be replaced by introducing two more dimensions as

$$\dot{u} = u(1 - u^2 - v^2) - \omega v, \quad (2.58)$$

$$\dot{v} = v(1 - u^2 - v^2) + \omega u.$$

where the two dynamic harmonic functions are described as  $u = \cos \omega t$  and  $v = \sin \omega t$ . We apply a 4<sup>th</sup> order Runge-Kutta numerical integration scheme to (2.57) and (2.58).

#### **Four Geometric Representations of the System Response**

In this paper, we apply four different kinds of geometric realizations of system response: system time traces, system phase portrait, three dimensional view of system phase portrait compare to input forcing, and system's power spectral density diagram. Below are short descriptions to these four representations.

**System Time Trace** The system time trace represents the system response with respect to time evolution. Periodic responses of a system can be detected by inspecting the repeated patterns in a system time trace. If a system response repeats itself after some constant time  $T$ , or  $x(t + T) = x(t)$ , then such a system is periodic with period  $T$ .

**System Phase Portrait** A phase portrait is a geometric representation of the trajectories of a dynamic system in the phase plane. A system with periodic response exhibits closed trajectories or orbits in a phase portrait. Associated with our phase portrait graphs are vector fields showing piecewise system response in a phase plane starting from uniformly distributed initial conditions.

**3D View of System Phase Portrait** By adding a new dimension, the system's periodic input  $u = \varepsilon \cos \omega t$ , to a system phase portrait, we may get a three dimensional view of a dynamic response. All closed orbits shown in a periodic phase portrait graph result in closed curves in a 3D phase portrait. Recall that the system response in a periodically forced inverted pendulum system is, in general, non-periodic. However, if a system's response is periodic under periodic forcing, one period of the system response cycle must be an integer multiple of the periodic forcing period. In other words, the periodic forcing frequency is  $N_r$  times larger than the periodic system response's frequency where  $N_r$  is an integer. Therefore, the frequency ratio  $N_r$  can be measured from counting the cycles of a 3D phase portrait graph of a periodic response.

**Power Spectral Density (PSD) Analysis** Power spectral density(PSD) describes how the power of a signal or discrete time series is distributed with frequency. PSD requires that the Fourier transforms of the signals exist and that the signals are square-integrable or square-summable. PSD can be applied to extract the frequency components of the response in order to obtain the periodic pattern of the signals composed of harmonic functions. We apply the discrete Fourier transform(DFT) to the dynamic response as follows:

$$u_k \equiv u(t_k) \equiv u(k\Delta t) = a_0 + 2 \sum_{n=1}^{N/2} \left( a_n \cos \frac{2\pi n t_k}{T} + b_n \sin \frac{2\pi n t_k}{T} \right). \quad (2.59)$$

where  $k = 1, 2, \dots, N$  is an integer index of  $t_k \equiv k\Delta t$  and  $\Delta t$  is the sampling interval;  $N$  is the total number of samples and  $T = N\Delta t$  is the sample period. The sampling frequency is defined as  $f_s = \frac{1}{\Delta t}$  which leads to the maximum observable frequency, or Nyquist frequency,

$f_{ny} = f_s/2$  or  $f_{ny} = \frac{1}{2\Delta t}$ . For convenience, throughout this paper for PSD calculations we used a uniform sampling frequency which is 500 Hz. The spectral coefficients  $a_n$  and  $b_n$  are defined as

$$a_n = \frac{1}{N} \sum_{j=1}^N u_j \cos \frac{2\pi nj}{N}, \quad (2.60)$$

$$b_n = \frac{1}{N} \sum_{j=1}^N u_j \sin \frac{2\pi nj}{N}. \quad (2.61)$$

The spectral coefficients represent the amplitudes of the harmonic components extracted from the dynamic response. The power spectral density is then defined as:

$$PSD = U\bar{U} = a_n^2 + b_n^2, \quad (2.62)$$

where  $U$  is the spectrum of  $u(t)$  defined as

$$U\left(\frac{n}{T}\right) \equiv a_n - ib_n = \frac{1}{N} \sum_{j=1}^N u_j \exp\left(-i\frac{2\pi nj}{N}\right). \quad (2.63)$$

where  $i \equiv \sqrt{-1}$  and  $\bar{U}$  represents the complex conjugate of  $U$ .

### Numerical Simulation Results of a sDOF Inverted Pendulum

We begin by presenting the first three types of system representations: time traces of inverted pendulum angles and angular velocities, phase portraits of the system, and a 3-dimensional view of the system phase portrait with respect to periodic forcing. Later in this chapter we introduced the power spectral density to further inspect its harmonic components.

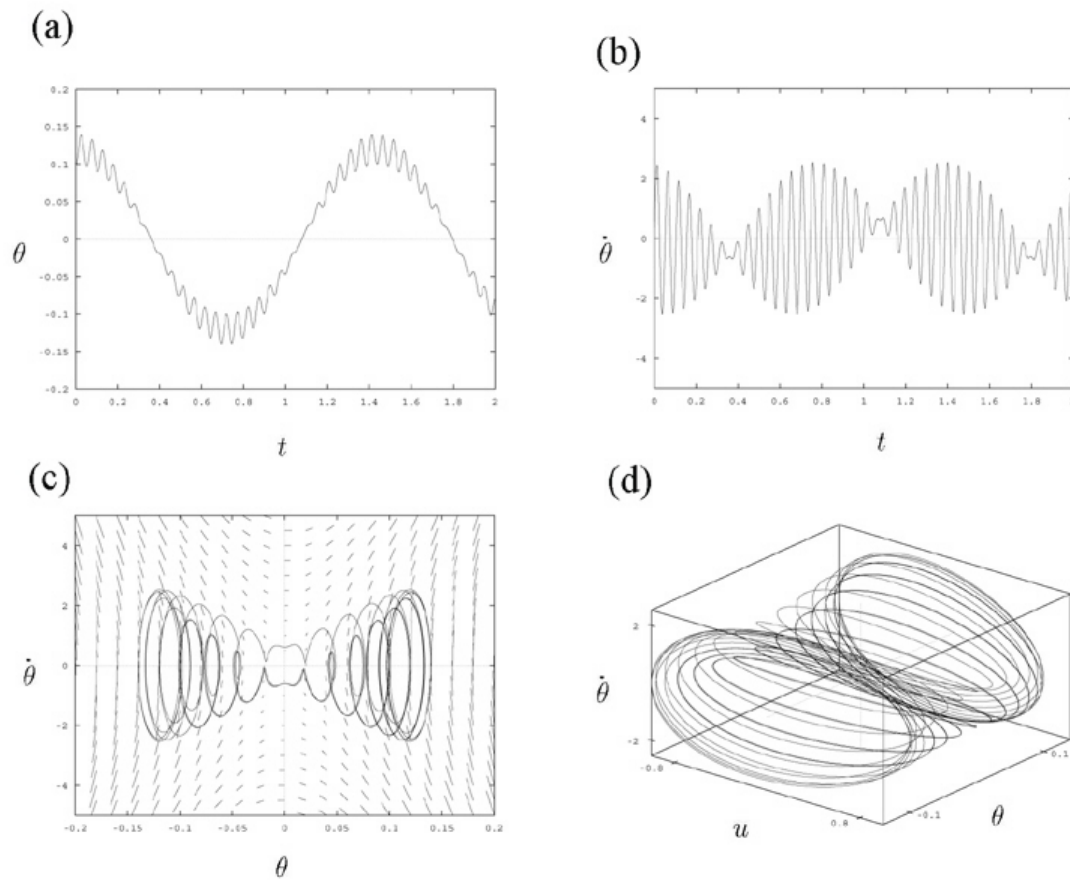


Figure 2.5: Numerical integration results of the single degree of freedom inverted pendulum under normalized forcing amplitude  $\epsilon = 0.1708$  and normalized forcing frequency  $\bar{\omega} = 8.7313$  with initial condition  $\theta_0 = 0.1$  and  $\dot{\theta}_0 = 0$ . (a) System time response. (b) Angular velocity time trace. (c) System phase portrait. (d) 3D view of phase portrait with respect to periodic forcing.

From inspection of Figure 2.5(a) we see the system time trace repeats itself in a period around 1.5s, which refers to slow time of the system response. The fast time response is proportional to the periodic vertical forcing at normalized forcing parameters  $\epsilon = 0.1708$  and  $\bar{\omega} = 8.7313$ . From Figure 2.5(b) we can see that the system angular velocity response also has the same slow time period of around 1.5s. From the phase portrait graph in Figure 2.5(c), we see a symmetric periodic orbit starting from a uniform distribution of initial conditions. There are two straight nullclines in the phase portrait at  $\theta = 0$ (vertical) and  $\dot{\theta} = 0$ (horizontal) lines. The intersection of these two nullclines is the system fixed point at  $(\theta, \dot{\theta}) = (0, 0)$ . Figure 2.5(d) indicates the 3-dimensional view of the system phase portrait with respect to forcing displacement  $u = \cos \omega t$ . In a periodic response we may use this 3D graph to count the number of forcing cycles in one period of the phase portrait cycle, which is the same as the number of fast time cycles in one slow time response period in the time trace. We can then obtain the frequency ratio of 28 : 1 from Figure 2.5(d). Notice that if the periodic orbit in the phase portrait is symmetric, then its ratio will have even numbers. For asymmetric phase portrait orbits, the ratio will have odd number.

**Definition 2** *Let  $\dot{x} = f(x)$  be a system of first order ordinary differential equation. The  $x_j$  nullcline is the set of points which satisfy  $f_j(x_1, x_2, \dots, x_n) = 0$  and the intersection points of nullclines are equilibrium points of the system.*

From inspection of Figure 2.6(a) we may see the system time trace repeats itself in a period of around 0.3s, which refers to slow time of the system response. The fast time response of time trace is proportional to the periodic vertical forcing at normalized forcing parameters  $\epsilon = 0.1710$  and  $\bar{\omega} = 14.2784$ . From Figure 2.6(b) we can see that the system

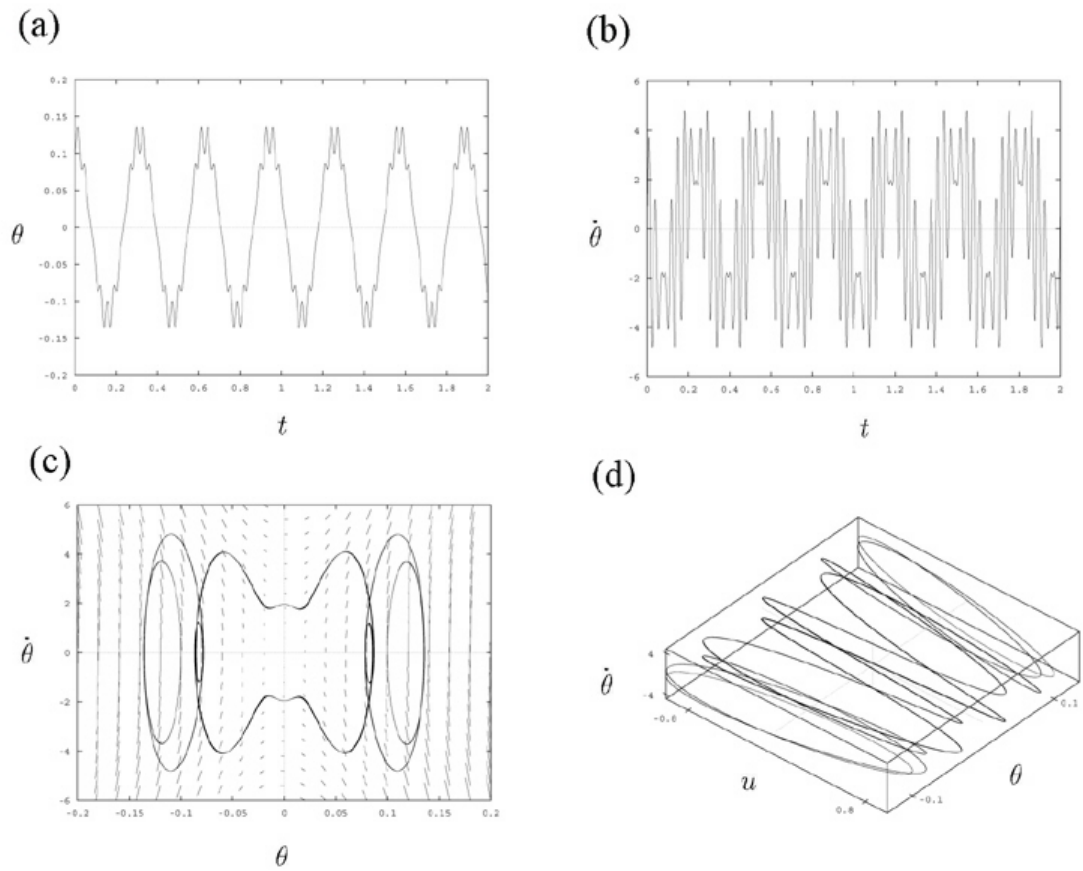


Figure 2.6: Numerical integration results of single degree of freedom inverted pendulum under  $\epsilon = 0.1710$  and  $\bar{\omega} = 14.2784$  with initial condition  $\theta_0 = 0.1$  and  $\dot{\theta}_0 = 0$ . (a) System time response. (b) Angular velocity time trace. (c) System phase portrait. (d) 3D view of phase portrait with respect to periodic forcing.

angular velocity response also has the same repeated period around 0.3s. In the system phase portrait graph in Figure 2.6(c), we see a symmetric periodic orbit in a vector field starting from uniform distribution of initial conditions. Figure 2.6(d) indicates 10 : 1 ratio from its 3D phase portrait.

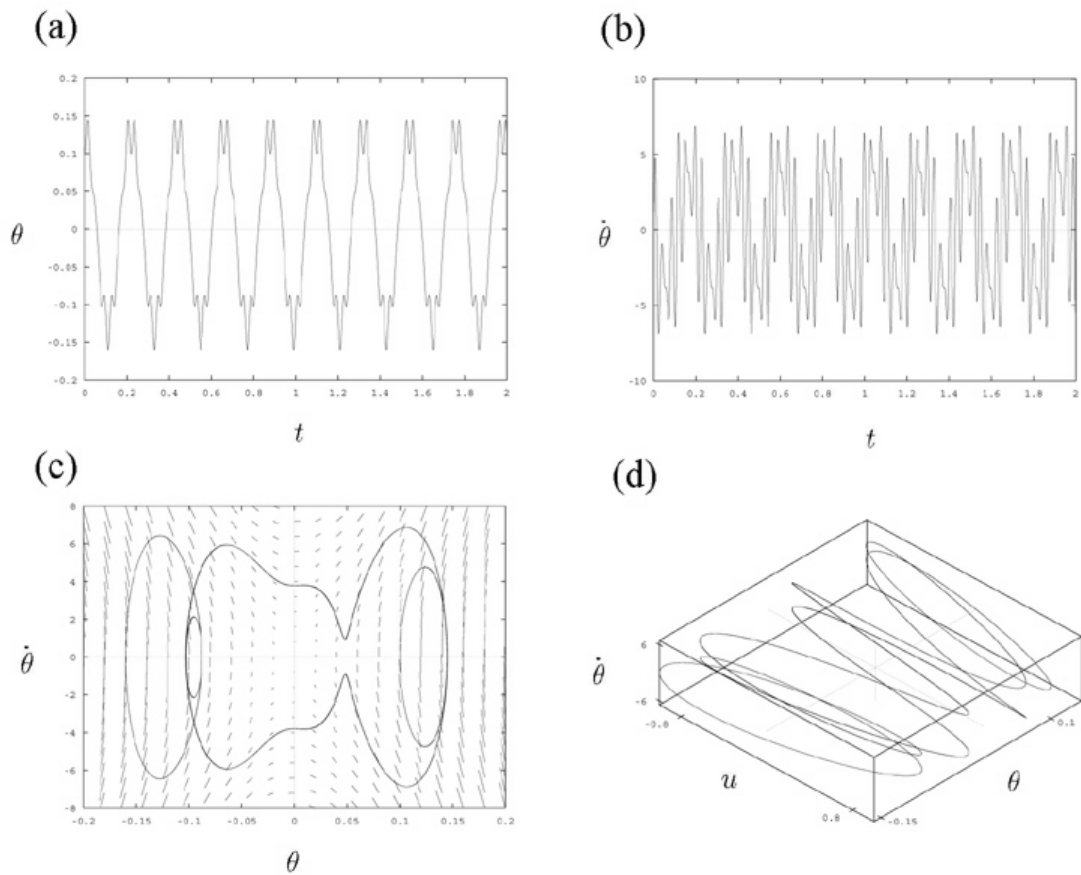


Figure 2.7: Numerical integration results of single degree of freedom inverted pendulum under normalized forcing amplitude  $\epsilon = 0.2193$  and normalized forcing frequency  $\bar{\omega} = 14.2784$  with initial condition  $\theta_0 = 0.1$  and  $\dot{\theta}_0 = 0$ . (a) System time response. (b) Angular velocity time trace. (c) System phase portrait. (d) 3D view of phase portrait with respect to periodic forcing.

From inspection of Figure 2.7(a) we may see the system time trace repeats itself in a period of around 0.25 s, which refers to slow time of the system response. The fast time response of time trace is proportional to the periodic vertical forcing at normalized forcing parameters  $\epsilon = 0.2193$  and  $\bar{\omega} = 14.2784$ . From Figure 2.7(b) we can see that the system angular velocity response also has the same repeated period of around 0.25 s. In the system phase portrait graph in Figure 2.7(c), we see an asymmetric periodic orbit in a vector field starting from uniform distribution of initial conditions. Figure 2.7(d) indicates 7 : 1 ratio from its 3D phase portrait.

From inspection of Figure 2.8(a) we may see the system time trace repeat itself in a period around 0.14s, which refers to slow time of the system response. The fast time response of time trace is proportional to the periodic vertical forcing at normalized forcing parameters  $\epsilon = 0.400$  and  $\bar{\omega} = 12.8506$ . From Figure 2.8(b) we can see that the system angular velocity response also has the same repeated period of around 0.14 s. In the system phase portrait graph in Figure 2.8(c), we see a symmetric periodic orbit in a vector field starting from uniform distribution of initial conditions. Figure 2.8(d) indicates 4 : 1 ratio from its 3D phase portrait.

Since the system response is in general not periodic, more often we may get quasi-periodic orbits for bounded solutions as shown in Figure 2.9. Figure 2.9 has forcing parameters  $\epsilon = 0.200$  and  $\bar{\omega} = 14.2784$  which is very close to Figure 2.8. However, their system responses are total different. From time trace of Figure 2.9 we can only conclude that the system has bounded solution. Although system show symmetric pattern but we cannot obtain its repeatability as easy as in Figure 2.8.

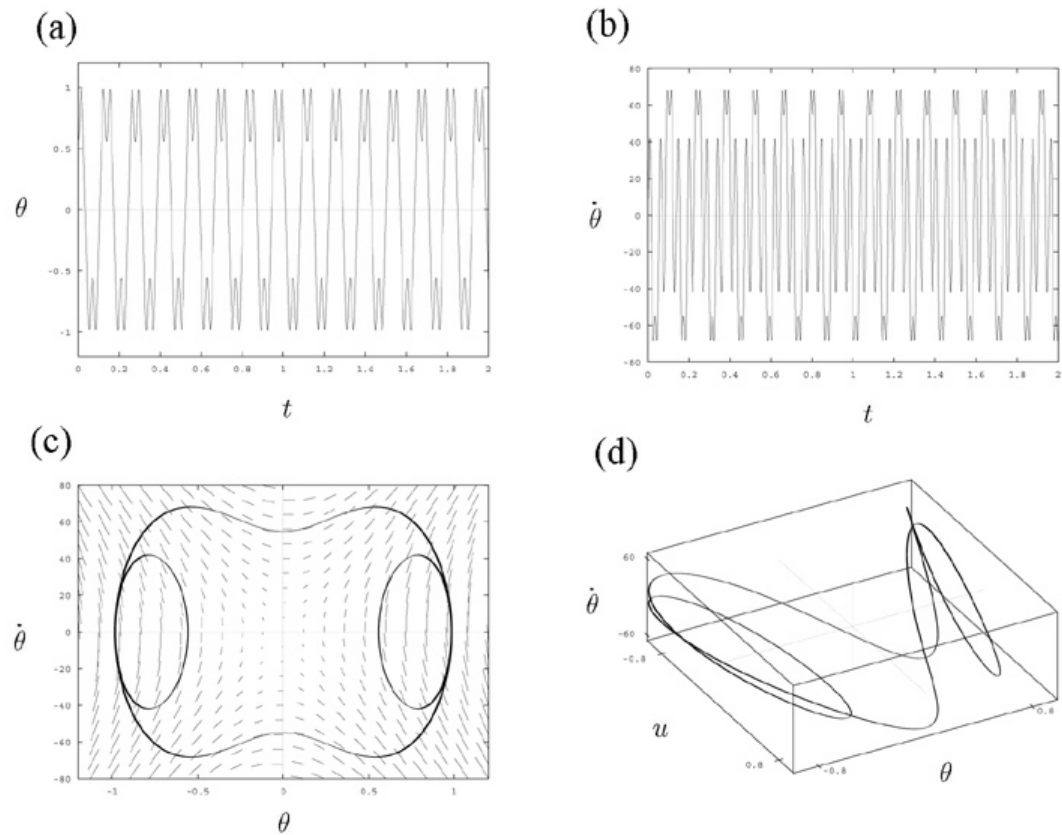


Figure 2.8: Numerical integration results of single degree of freedom inverted pendulum under normalized forcing amplitude  $\epsilon = 0.400$  and normalized forcing frequency  $\bar{\omega} = 12.8506$  with initial condition  $\theta_0 = 0.56$  and  $\dot{\theta}_0 = 0$ . (a) System time response. (b) Angular velocity time trace. (c) System phase portrait. (d) 3D view of phase portrait with respect to periodic forcing.

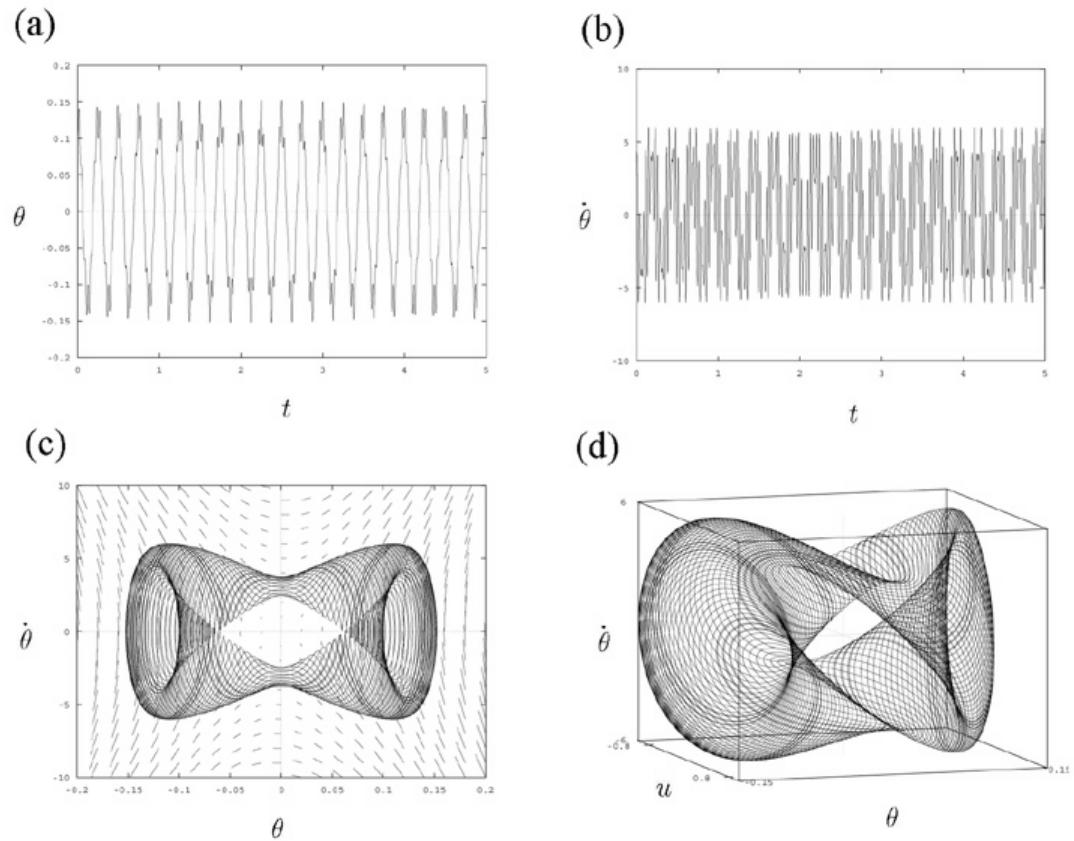


Figure 2.9: Numerical integration results of single degree of freedom inverted pendulum under normalized forcing amplitude  $\epsilon = 0.200$  and normalized forcing frequency  $\bar{\omega} = 14.2784$  with initial condition  $\theta_0 = 0.1$  and  $\dot{\theta}_0 = 0$ . (a) System time response. (b) Angular velocity time trace. (c) System phase portrait. (d) 3D view of phase portrait with respect to periodic forcing.

### Increasing the Forcing Amplitude

Figure 2.10, 2.11 and 2.12 present the numerical results for the inverted pendulum under varying periodic forcing amplitudes. In these 3 graphs, we vary the forcing amplitude  $\epsilon$ , holding the normalized forcing frequency  $\bar{\omega}$  fixed at  $\bar{\omega} = 14.2784$ . This normalized forcing frequency corresponds to the physical forcing frequency around 25 Hz. All system initial conditions start from  $\theta_{1_0} = 0.1$  and  $\dot{\theta}_{1_0} = 0$ . Four system response representations are shown in a systematic way from left to right as: system response time trace, system phase portrait, 3D phase portrait, and power spectral density graph of system response, respectively. The normalized forcing amplitude  $\epsilon$  increases from top to bottom and from Figure 2.10 to Figure 2.12. Recall Figure 2.4 in the previous chapter where this simulation data sets were presented in the sDOF inverted pendulum stability diagram shown in  $\epsilon - \bar{\omega}$  plane. This set of data points are referred to as 'numerical simulation 1 (Chen)' indicated by the red diamond dots in Figure 2.4. As  $\epsilon$  increases, the location of the data point moving toward the right side of Figure 2.4 horizontally with fixed  $\bar{\omega}$  value. All data points were within the bounded region as predicted by the transition curves obtained from solving the linear Mathieu's equation. From inspecting Figure 2.10 to Figure 2.12, we notice that as  $\epsilon$  increases, the frequency ratio  $N_r$  decreases.

As shown on the top graph in Figure 2.10, under  $\epsilon = 0.1019$  the time trace has two distinct frequencies. One is referred to as the fast time response which is directly related to the forcing frequency; the other is referred to as slow time response which frequency is 54 times less than the forcing frequency. It's phase portrait has right moving vector field when  $\dot{\theta} > 0$ , and left moving vector field when  $\dot{\theta} < 0$ . Two nullclines are shown at the

horizontal line  $\dot{\theta} = 0$  and the vertical line  $\theta = 0$  in the phase plane which indicate that the system has an equilibrium point located at  $(\dot{\theta}, \theta) = (0, 0)$ . The phase portrait shows one closed orbit, even with large numerical integration time. It's 3D phase portrait measured 54 : 1 frequency ratio where 54 forcing cycles can be counted from one phase portrait orbit. The power spectral density graph shows three distinct harmonic components, the largest peak in the low frequency region where the resolution of the graph is not fine enough to identify the exact location, the second peak is located at around 25 Hz, and the third peak is located at around 50 Hz. The low frequency peak is referred to as the slow time response of the system which may be measured from the time trace graph around 0.5 Hz; the peak at around 25 Hz is referred to as fast time system response which corresponds to the periodic forcing frequency. As we increase the value of  $\epsilon$ , the system's slow time response becomes more rapid, resulting in a higher frequency in its largest peak in the power spectral density graph. If we inspect the evolution of system power spectral density graphs from increasing  $\epsilon$ , we note that not only its largest peak moving toward the higher frequency region, it's second and third peaks become wider in shape and eventually split into two new peaks as shown in  $\epsilon = 0.1611$ . There were higher frequency peaks after the third peaks and they became more obvious when  $\epsilon$  increased. These peaks also became wider in shape and finally split at higher  $\epsilon$  values. When the frequency ratio  $N_r$  has even value, the phase portrait exhibits a symmetric pattern, as shown in  $N_r = 54, 40, 30, \dots, 10, 6, 4$ ; while the frequency ratio  $N_r$  has odd value, the phase portrait exhibits an asymmetric pattern as shown in  $N_r = 27, 19, \dots, 11, 7, 5$ . Figure 2.10 to Figure 2.12 does not show periodic solutions with every periodic. In fact, we may find solutions in every period from  $N_r \geq 4$  provided that

the numerical simulation tool has high enough resolution.

## Nonlinear Analysis of $s$ DOF Model Using Perturbation Theory

In order to understand the nonlinear effect further in detail in the single degree of freedom inverted pendulum model described in (2.12), we applied a two-timing perturbation technique to the normalized model (2.56). Different than the direct numerical integration method that deal with time-varying model as described in previous sections, perturbation technique can transfer the original time-varying equation of motion into a set of autonomous ordinary differential equations. One of the advantages of applying perturbation technique is that large system response solutions can be obtained, system response won't be limited by the small angle assumption as in the linear case. Also, the cost for numerical simulations on perturbation technique is usually less than direct numerical integration to the full time-varying model.

We applied 2-timing perturbation technique by assigning  $t$  as slow system time and  $\tau = \bar{\omega}t$  as fast system time then making second time derivatives using chain rules:

$$\frac{d^2}{dt^2} = \frac{\partial^2}{\partial t^2} + 2\bar{\omega} \frac{\partial^2}{\partial t \partial \tau} + \bar{\omega}^2 \frac{\partial^2}{\partial \tau^2}. \quad (2.64)$$

We then apply a uniform expansion using the normalized driving amplitude  $\epsilon$  as a perturbation parameter in the following form:

$$\theta(t, \tau; \epsilon) = \theta_0(t, \tau) + \epsilon \theta_1(t, \tau) + \epsilon^2 \theta_2(t, \tau) + \dots \quad (2.65)$$

Substitute (2.64) and (2.65) into (2.56),

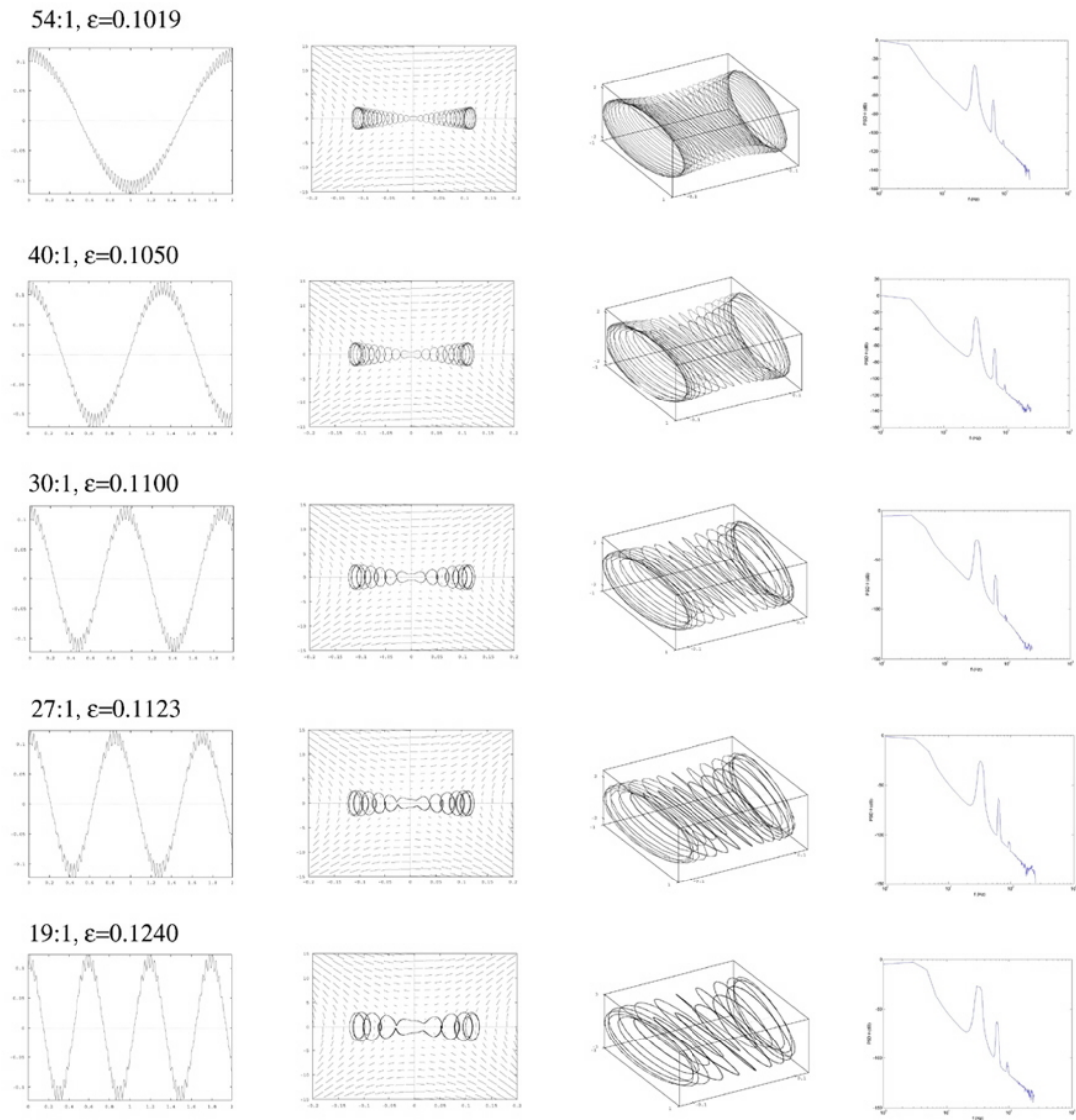


Figure 2.10: Numerical simulation results of periodic solutions from varying normalized forcing amplitude  $\epsilon$  with fixed normalized forcing frequency  $\bar{\omega} = 14.2784$ . Graphs from top to bottom show  $\epsilon$  values increase from  $\epsilon = 0.1019$  to  $\epsilon = 0.1240$ . From left to right showing four geometric representations of system response: time trace, phase portrait, 3D phase portrait, and PSD, respectively.

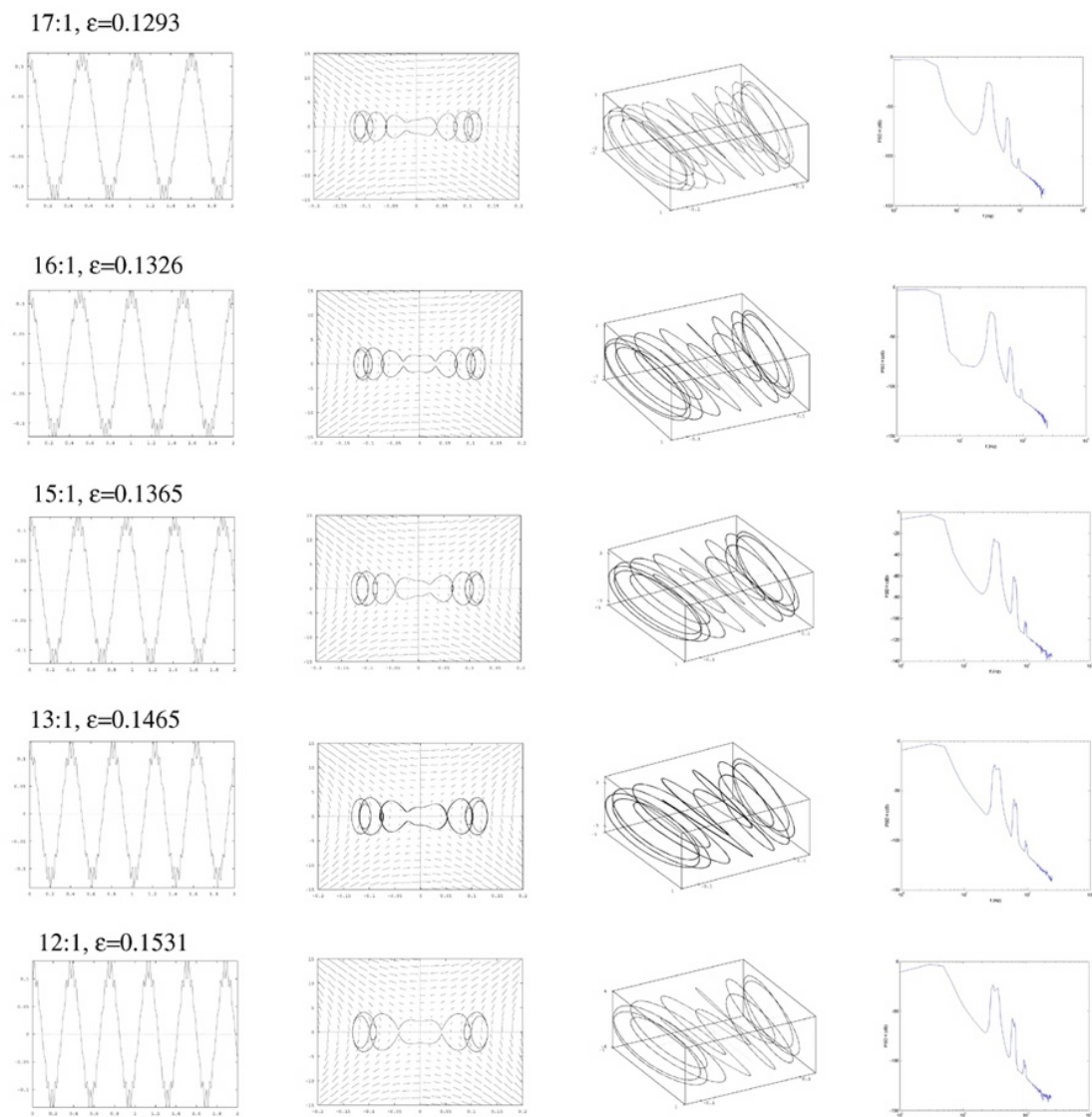


Figure 2.11: (Cont. of 2.10) Numerical simulation results of periodic solutions from varying normalized forcing amplitude  $\epsilon$  with fixed normalized forcing frequency  $\bar{\omega} = 14.2784$ . Graphs from top to bottom show  $\epsilon$  values increase from  $\epsilon = 0.1293$  to  $\epsilon = 0.1531$ . From left to right showing four geometric representations of system response: time trace, phase portrait, 3D phase portrait, and PSD, respectively.

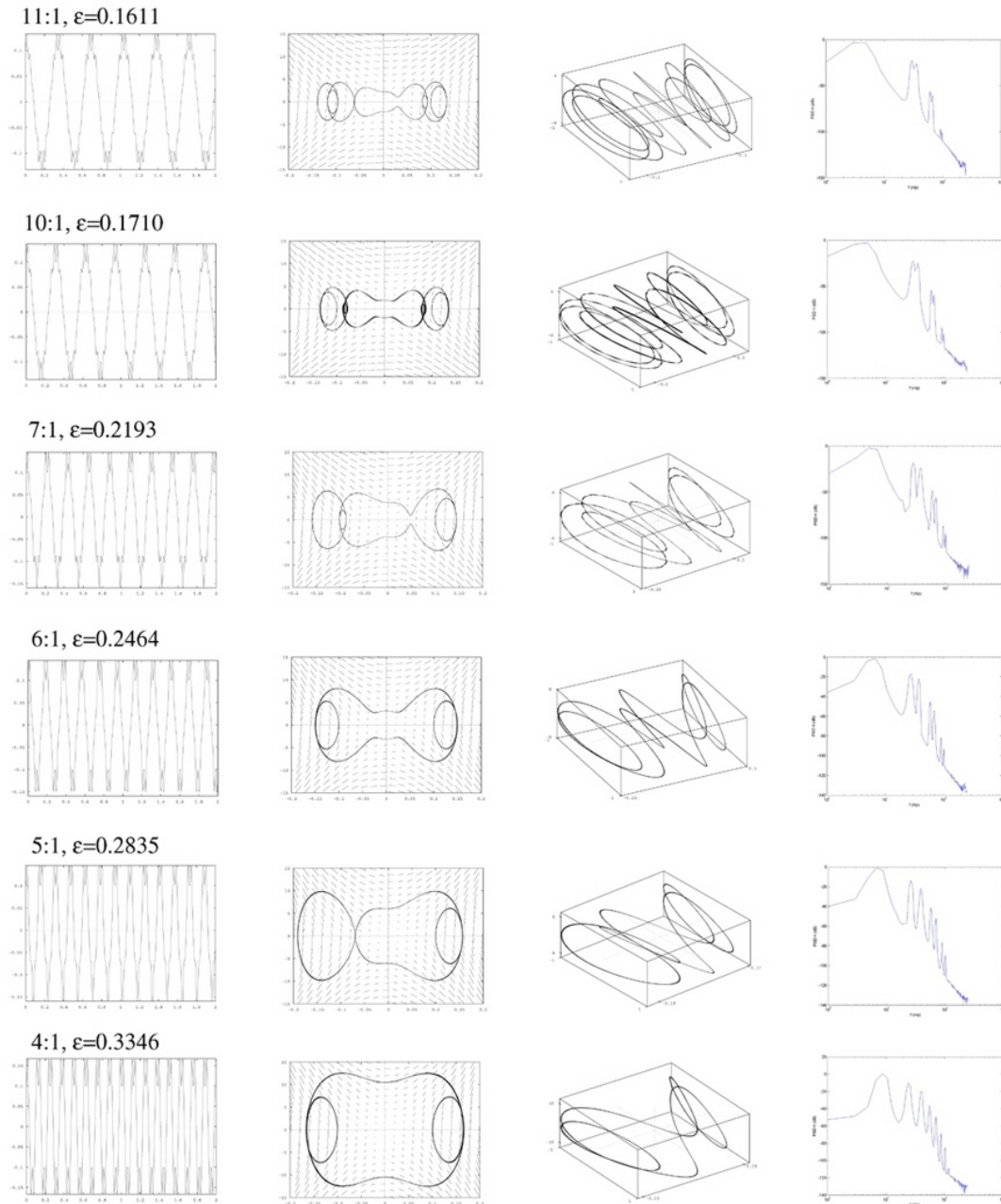


Figure 2.12: (Cont. of 2.11) Numerical simulation results of periodic solutions from varying normalized forcing amplitude  $\epsilon$  with fixed normalized forcing frequency  $\bar{\omega} = 14.2784$ . Graphs from top to bottom show  $\epsilon$  values increase from  $\epsilon = 0.1611$  to  $\epsilon = 0.3346$ . From left to right showing four geometric representations of system response: time trace, phase portrait, 3D phase portrait, and PSD, respectively.

$$\underbrace{\left(\frac{\partial^2}{\partial t^2} + 2\bar{\omega}\frac{\partial^2}{\partial t\partial\tau} + \bar{\omega}^2\frac{\partial^2}{\partial\tau^2}\right)}_{\text{LHS}}\theta(t, \tau; \epsilon) = \underbrace{(1 + \epsilon\bar{\omega}^2 \cos \omega_n\tau)}_{\text{RHS}}\omega_n^2 \sin \theta(t, \tau; \epsilon). \quad (2.66)$$

By expanding LHS(Left-hand-side) and RHS(Right-hand-side) of (2.66) using Taylor series expansion and then compare them with the same  $\epsilon$  order, yields:

$$O\left(\frac{1}{\epsilon^2}\right) : \frac{\partial^2}{\partial\tau^2}\theta_0 = 0, \quad (2.67)$$

$$O\left(\frac{1}{\epsilon}\right) : 2\frac{\partial^2}{\partial t\partial\tau}\theta_0 + k\frac{\partial^2}{\partial\tau^2}\theta_1 = \omega_n^2 [k \cos \omega_n\tau \sin \theta_0], \quad (2.68)$$

$$O(1) : \frac{\partial^2}{\partial t^2}\theta_0 + 2k\frac{\partial^2}{\partial t\partial\tau}\theta_1 + k^2\frac{\partial^2}{\partial\tau^2}\theta_2 = \omega_n^2 [\sin \theta_0 + k^2 \cos \omega_n\tau(\theta_1 \cos \theta_0)], \quad (2.69)$$

$$\begin{aligned} O(\epsilon) : & \frac{\partial^2}{\partial t^2}\theta_1 + 2k\frac{\partial^2}{\partial t\partial\tau}\theta_2 + k^2\frac{\partial^2}{\partial\tau^2}\theta_3 \\ & = \omega_n^2 \left[ \theta_1 \cos \theta_0 + k^2 \cos \omega_n\tau(\theta_2 \cos \theta_0 - \frac{1}{2}\theta_1^2 \sin \theta_0) \right]. \end{aligned} \quad (2.70)$$

Equations (2.67), (2.68), (2.69) and (2.70) all fulfill the governing equation in (2.66). Notice that in above equations we introduced a scaling factor  $k$  which is defined as normalized driving amplitude  $\epsilon$  multiply by normalized driving frequency  $\bar{\omega}$  as

$$k = \epsilon\bar{\omega} \quad (2.71)$$

This  $k$  scale factor is related to the linear stability limit curve  $\epsilon^2\omega^2 = 2gL$  as shown in Figure 2.4. In our system  $k$  has value around 1.2 to be on the stability limit curve and stability condition in our system requires that  $k > 1.2$ .

Since we are looking for bounded solutions  $\theta(t)$  for (2.56), which we may get approximate solutions from solving the equations for  $\theta_0, \theta_1, \theta_2, \dots$  and then combine them using (2.65). The bounded solutions of  $\theta(t)$  require that those equations of  $\theta_0, \theta_1, \theta_2, \dots$  are

also bounded. Using this bounded property we formulated the equations carrying out the integrations of individual equations to fulfill the original equation of motion. In the next sections we show derivations from solving the equations for different  $\epsilon$  orders to get the final approximate solution for (2.56).

### Solutions from Solving $O(\frac{1}{\epsilon^2})$

Starting from the lowest order of  $\epsilon$  equation, (2.67) is a homogeneous  $2^{nd}$  order ordinary differential equation which we may get solutions through direct integrations. We first integrated the equation of order  $O(\frac{1}{\epsilon^2})$  with respect to  $\tau$ , (2.67) becomes

$$\frac{\partial}{\partial \tau} \theta_0(t, \tau) = A(t) \quad (2.72)$$

where new function  $A(t)$  is being introduced from previous integration step which is not a function of  $\tau$ . Making another integration to (2.72) with respect to  $\tau$  yields

$$\theta_0(t, \tau) = A(t)\tau + B(t) \quad (2.73)$$

where new function  $B(t)$  is being introduced from previous integration step. Since we were looking for solutions where  $\theta_0(t, \tau)$  remain bounded as  $t, \tau \rightarrow \infty$ , we must assign  $A(t) \equiv 0$  which leads to

$$\theta_0(t, \tau) = B(t). \quad (2.74)$$

This result shows that the system's slow time response is synchronized with  $B(t)$  and the response is not affected by the fast system time  $\tau$ . So far, we can only conclude that  $B(t)$  is bounded in time and if we are looking for periodic solution of  $\theta(t)$  then  $B(t)$  also needs

to be periodic in time. From carrying out integrations through higher  $\epsilon$  order equations we may find more constraints for  $B(t)$  to fulfill the bounded conditions. We showed derivations from solving higher  $\epsilon$  order equations in the following sections.

### Solutions from Solving $O(\frac{1}{\epsilon})$

From (2.68) we can see that  $O(\frac{1}{\epsilon})$  equation coupled  $\theta_0$  and  $\theta_1$  in a  $2^{nd}$  order ordinary differential equation. The first term in (2.68) can be calculated by making time derivatives to  $\theta_0(t, \tau)$  with respect to  $t, \tau$  yields

$$\frac{\partial^2}{\partial t \partial \tau} \theta_0(t, \tau) = 0. \quad (2.75)$$

Substitute (2.75) and (2.74) into (2.68) yields

$$\frac{\partial^2}{\partial \tau^2} \theta_1 = \omega_n^2 \cos \omega_n \tau \sin B(t). \quad (2.76)$$

Integrate (2.76) with respect to  $\tau$  we get

$$\frac{\partial}{\partial \tau} \theta_1(t, \tau) = \omega_n \sin \omega_n \tau \sin B(t) + C(t) \quad (2.77)$$

where new function  $C(t)$  is being introduced from previous integration step. Making another integration to (2.77) with respect to  $\tau$  yields

$$\theta_1(t, \tau) = -\cos \omega_n \tau \sin B(t) + \tau C(t) + D(t) \quad (2.78)$$

where new function  $D(t)$  is being introduced from previous integration step. Since our goal is to look for solutions that remain bounded as  $t, \tau \rightarrow \infty$ , we may conclude that  $C(t) \equiv 0$

is required to fulfill bounded conditions. Therefore, (2.78) becomes

$$\theta_1(t, \tau) = -\cos \omega_n \tau \sin B(t) + D(t). \quad (2.79)$$

Since  $\omega_n \tau = \omega t$ , we have

$$\theta_1(t) = -\cos \omega t \sin B(t) + D(t) \quad (2.80)$$

Therefore, we can conclude that  $\theta_1$  is a function of two new bounded function  $B(t)$  and  $D(t)$ . In searching for periodic solutions to  $\theta(t)$  requires that  $\theta_0$  and  $\theta_1$  both periodic in time which leads to searching for periodic functions of  $B(t)$  and  $D(t)$ . Next section we continued to carry out integrations to higher  $\epsilon$  order equations in order to find proper functions for  $B(t)$  and  $D(t)$ .

### Solutions from Solving $O(1)$

From (2.69) we can see that  $O(1)$  equation coupled  $\theta_0, \theta_1$  and  $\theta_2$  in a  $2^{nd}$  order ordinary differential equation. We rearranged (2.69) as

$$k^2 \frac{\partial^2}{\partial \tau^2} \theta_2 = -\frac{\partial^2}{\partial t^2} \theta_0 - 2k \frac{\partial^2}{\partial t \partial \tau} \theta_1 + \omega_n^2 [\sin \theta_0 + k^2 \cos \omega_n \tau (\theta_1 \cos \theta_0)]. \quad (2.81)$$

By calculating one of the intermediate terms in (2.81) from taking time derivatives to  $\theta_0(t, \tau)$  with respect to  $t$ , we have

$$\frac{\partial^2}{\partial t^2} \theta_0(t, \tau) = \ddot{B}(t). \quad (2.82)$$

Another intermediate term in (2.81) can be calculated by taking time derivatives to  $\frac{\partial}{\partial \tau} \theta_1(t, \tau)$  with respect to  $t$

$$\frac{\partial^2}{\partial t \partial \tau} \theta_1(t, \tau) = \dot{B}(t) \omega_n \sin \omega_n \tau \cos B(t). \quad (2.83)$$

Substitute  $\theta_0$  and  $\theta_1$  equations in (2.74) and (2.80) into the 4<sup>th</sup> term of (2.81), we have

$$\begin{aligned} k^2 \cos \omega_n \tau (\theta_1 \cos \theta_0) &= k^2 \cos \omega_n \tau (-\cos \omega_n \tau \sin B(t) + D(t)) \cos B(t) \\ &= -k^2 \cos^2 \omega_n \tau \sin B(t) \cos B(t) \\ &\quad + k^2 D(t) \cos \omega_n \tau \cos B(t). \end{aligned} \quad (2.84)$$

We then applied the following trigonometric identities to simplify (2.84)

$$\begin{aligned} \cos^2 \omega_n \tau &= \frac{1}{2} - \frac{1}{2} \cos(2\omega_n \tau), \\ \sin B(t) \cos B(t) &= \frac{1}{2} \sin(2B(t)). \end{aligned}$$

Therefore (2.84) becomes

$$\begin{aligned} &k^2 \cos \omega_n \tau (\theta_1 \cos \theta_0) \\ &= -\frac{k^2}{4} \sin(2B(t)) + \frac{k^2}{4} \cos(2\omega_n \tau) \sin(2B(t)) + k^2 D(t) \cos \omega_n \tau \cos B(t). \end{aligned} \quad (2.85)$$

Substitute (2.82),(2.83) and (2.85) into (2.81), we have

$$\begin{aligned}
k^2 \frac{\partial^2}{\partial \tau^2} \theta_2(t, \tau) &= -\ddot{B}(t) - 2k\dot{B}(t)\omega_n \sin \omega_n \tau \cos B(t) + \omega_n^2 \sin B(t) \\
&\quad - \frac{k^2 \omega_n^2}{4} \sin(2B(t)) + \frac{k^2 \omega_n^2}{4} \cos(2\omega_n \tau) \sin(2B(t)) \\
&\quad + k^2 \omega_n^2 D(t) \cos \omega_n \tau \cos B(t) \\
&= - \underbrace{\left[ \ddot{B}(t) - \omega_n^2 \sin B(t) + \frac{k^2 \omega_n^2}{4} \sin(2B(t)) \right]}_{\text{not function of } \tau} \\
&\quad - 2k\dot{B}(t)\omega_n \sin \omega_n \tau \cos B(t) + \frac{k^2 \omega_n^2}{4} \cos(2\omega_n \tau) \sin(2B(t)) \\
&\quad + \underbrace{k^2 \omega_n^2 D(t) \cos \omega_n \tau \cos B(t)}_{\text{function of } t, \tau}.
\end{aligned} \tag{2.86}$$

From (2.86), bounded conditions lead to the following equation:

$$\ddot{B}(t) - \omega_n^2 \sin B(t) + \frac{k^2 \omega_n^4}{4} \sin(2B(t)) = 0, \tag{2.87}$$

$$D(t) = 0. \tag{2.88}$$

Equation (2.87) is an autonomous  $2^{nd}$  order ordinary differential equation governing the response of  $B(t)$ . Therefore, we may approximate the inverted pendulum's response  $\theta(t)$  by inserting the solution of (2.87) into the first two terms of (2.65)

$$\begin{aligned}
\theta(t) &\cong \theta_0(t) + \epsilon \theta_1(t), \\
&= B(t) - \epsilon \cos \omega t \sin B(t).
\end{aligned} \tag{2.89}$$

We present numerical simulations of (2.87), (2.89) in later sections.

**Solve**  $\ddot{B} - \omega_n^2 \sin B + \frac{k^2 \omega_n^4}{4} \sin(2B) = 0$  **by Energy Equation**

In analyzing (2.87), we introduce the energy equation which we may obtain from multiplying both sides of (2.87) by  $\dot{B}(t)$  as

$$\dot{B}(t)\ddot{B}(t) - \omega_n^2 \dot{B}(t) \sin B(t) + \frac{k^2 \omega_n^4}{4} \dot{B}(t) \sin(2B(t)) = 0. \quad (2.90)$$

From (2.90) we get the following equation

$$\frac{d}{dt} \left[ \underbrace{\left( \frac{1}{2} (\dot{B}(t))^2 \right)}_{\text{Kinetic Energy } T(\dot{B})} + \underbrace{\left( \omega_n^2 \cos B(t) - \frac{k^2 \omega_n^4}{8} \cos(2B(t)) \right)}_{\text{Potential Energy } V(B)} \right] = 0. \quad (2.91)$$

Equation (2.91) fulfills the energy conservation law as

$$T + V = E = \text{constant}, \quad (2.92)$$

where system kinetic energy  $T$  takes the form

$$T(\dot{B}) = \frac{1}{2} (\dot{B}(t))^2 \quad (2.93)$$

and the system potential energy  $V$  takes the form

$$V(B) = 2\omega_n^2 \cos B(t) - \frac{k^2 \omega_n^4}{4} \cos(2B(t)). \quad (2.94)$$

From (2.92) and (2.93) we can also get the following relation for  $\dot{B}$

$$\dot{B}(t) = \pm \sqrt{E - V} \quad (2.95)$$

where  $E - V = T > 0$ . We present results by combining the potential energy graph to the solutions of  $\theta(t)$  from solving  $B(t)$  numerically as shown in Figure 2.13.

### Simulation Results Based on Perturbation Analysis

Through the derivations from perturbation analysis we may transfer the original time-varying equation of motion as in (2.12) to describe the inverted pendulum under periodic forcing into a set of autonomous ordinary differential equations as in (2.87) and (2.89). From solving (2.87) using numerical integration, and plugging the results of  $B(t)$  into (2.89), we may get the inverted pendulum's response due to different forcing parameters. Figure 2.13 documents the inverted pendulum's response with fixed periodic forcing amplitude  $\epsilon = 0.1233$ . Notice that we are now dealing with solving the autonomous system of  $B$  by treating the forcing parameters  $\epsilon$  and  $\omega$  as constants. The advantage of this system is that we can deal with large initial conditions and large system response. In Figure 2.13, each individual sub-graph indicates the condition of applying different forcing frequency and different initial conditions. Each sub-graph has four parts from top to bottom: system time response, system angular velocity response, system phase portrait with initial starting angle, and the potential energy graph at the starting initial conditions. The upper left graph in Figure 2.13 shows under normalized forcing frequency  $\bar{\omega} = 3.4$  the system won't be stable in any initial conditions. The unstable behavior can be seen from its potential energy graph where the maximum potential occurs in its upright vertical position. There are three sub-graphs showing the conditions of  $\bar{\omega} = 10.2$ , the only stable case is when the system starts from initial conditions at  $\theta_0 = 0.5236$  and  $\dot{\theta}_0 = 0$ . These three system have the same system potential energy graph which indicates that the upright vertical position is the local minimum of the potential. As we increase the normalized forcing frequency  $\bar{\omega}$ , we notice that the potential energy graphs change. In some cases the pendulum can be sta-

bilized near its inverted state even when the system doesn't have local minimum potential at its upright vertical position as in the case of  $\bar{\omega} = 20.4, \theta_0 = 0.5236$  and  $\dot{\theta}_0 = 0$ . Under proper conditions, the system will encounter bounded solutions as in  $\bar{\omega} = 17.4, \theta_0 = 0.2356$  and  $\dot{\theta}_0 = 0$ ; in some cases the system responses are near periodic as in  $\bar{\omega} = 20.4, \theta_0 = 0.5236$  and  $\dot{\theta}_0 = 0$ . Our simulation result showed that large periodic system response is possible even with large initial conditions. In the case of  $\bar{\omega} = 20.4, \theta_0 = 0.8727$  and  $\dot{\theta}_0 = 0$ , system started from around  $50^\circ$  initial angles and the pendulum was swinging in its inverted states with system response as large as  $50^\circ$ .

Although our intention in our research wasn't to get quantitative matches between numerical simulations and experiments, our results showed that it is possible to get a close match from fine-tuned system parameters. Figure 2.14 shows one of the results of a comparison where the simulation followed closely to experiment. The top portion of the graph shows the system time trace with the inverted pendulum's angle response with respect to time; bottom portion of the graph shows system phase portrait with the pendulum's angle in the horizontal axis and the pendulum's angular velocity in the vertical axis. Figure 2.14(a) shows the experimental data points of a single degree of freedom inverted pendulum under vertical periodic forcing. The inverted pendulum was swinging in a large angle response with the largest swinging angle around  $50^\circ$ . Both time trace and phase portrait graphs indicate near periodic system behavior and the response showed very little damping effect. Figure 2.14(b) shows the simulation result of applying perturbation technique to nonlinear single degree of freedom inverted pendulum model as in (2.56). The system has normalized forcing amplitude  $\epsilon = 0.136$  and normalized forcing frequency  $\bar{\omega} = 19.3$  with

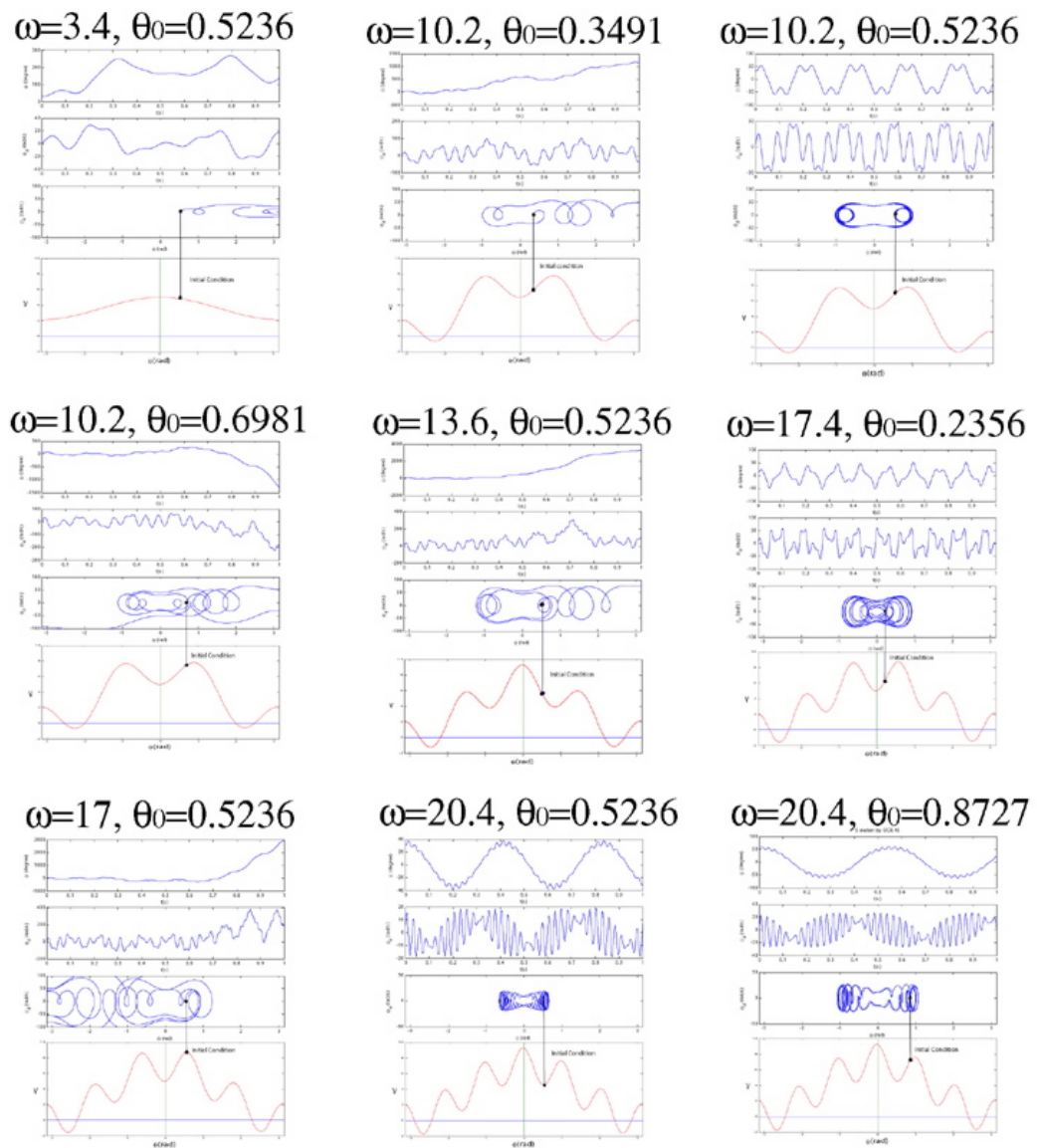


Figure 2.13: Numerical simulation based on perturbation analysis solutions. All simulation is under fixed normalized driving amplitude  $\epsilon = 0.1233$ .

initial conditions  $\theta_0 = 45^\circ$  and  $\dot{\theta}_0 = 0$ .

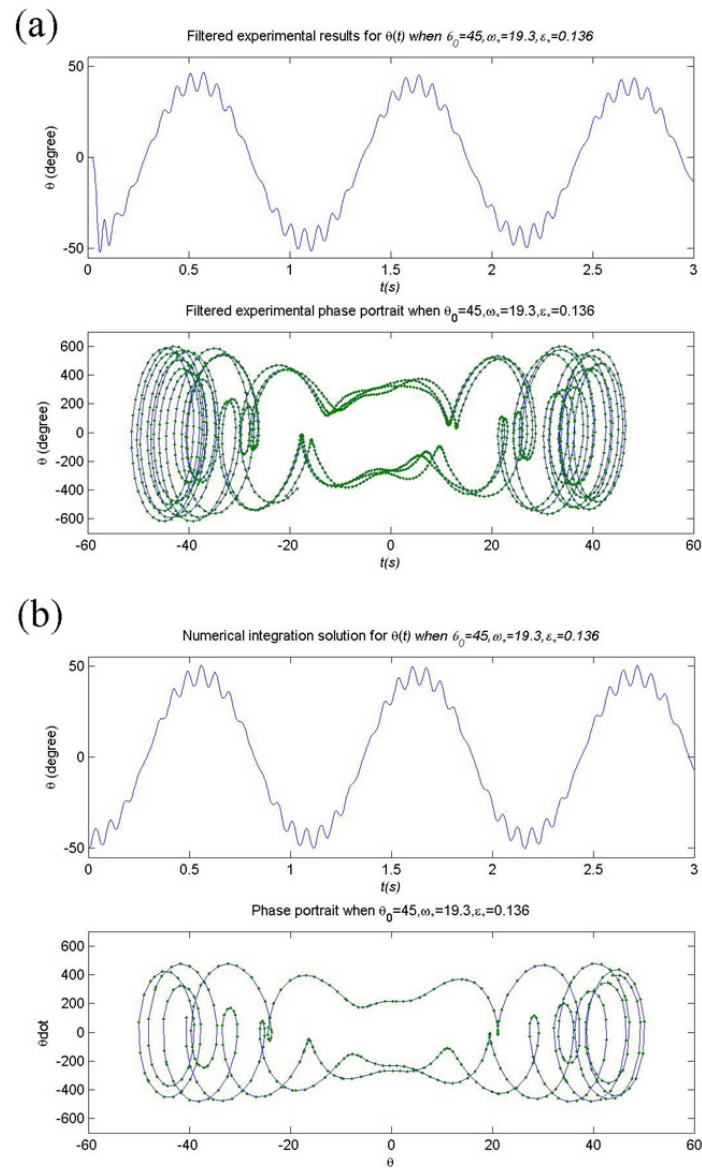


Figure 2.14: Quantitative comparison of the perturbation analysis simulation result to the experimental result. (a) filtered experimental time trace and phase portrait (b) simulation time trace and phase portrait.

## Chapter 3

# Experiments on the $s$ DOF Inverted Pendulum

In order to understand the inverted pendulum dynamics further, we conducted several experiments to compare in detail the results from measuring the responses of the real-life apparatus to the predictions from numerical simulations. In the following sections, we show the material and methods involved in our experiments, later, we present our experimental results and then compare that to our numerical simulation results.

### 3.1 Material and Methods

#### Driving Inverted Pendulum by Loud Speaker

Following our theoretical model as described in (2.12), we conducted  $s$ DOF experiments with experimental apparatus as close to the assumptions in the theoretical model as possible. Recall our  $s$ DOF model as in Figure 2.1, our  $s$ DOF inverted pendulum model

consists of a point mass mounted on a weightless rigid rod which encounters periodic vertical forcing at its base. Since the ideal pendulum setup is not feasible experimentally, an alternate setup with light-weight rigid rod mounted with much heavier tip mass was used instead, as shown in Figure 3.1. The pivot point of the inverted pendulum was made by a commercially available high precision ball bearing. There are two major functions to this ball-bearing setup at its base: one is to minimize the rotational friction while the pendulum is in swinging motion. The other is to keep the pendulum moving on  $XY$  planer motion without any other 3 dimensional effect. As in Figure 2.1, the pendulum consists of CNC machined rigid rod composed of Aluminum alloy with a heavier stainless steel made ball-bearing mounted on its tip. The full pendulum length is measured as  $L = 80.0 \pm 0.1mm$ , we measured its combined center of mass located at  $R = 53.7 \pm 0.1mm$  measured from the base with total weight of  $3.8 \pm 0.1g$ .

The base of the inverted pendulum was mounted at the ball-bearing pivot which was firmly attached to a stand mounted on top of the center cone of the speaker. The speaker was a 15 in diameter commercially available subwoofer loud speaker. This loud speaker is capable of taking up to 140 W RMS signals. The speaker core is composed of 2 in thick voice coil with 40oz of magnet and its impedance rating is  $4\Omega$ . We applied a function generator to generate a sinusoidal wave and amplified it using a 100 W PA power supply to drive the speaker. With this setup, it is capable of generating up to  $50G$  of acceleration to drive the total weight of roughly 10 g inverted pendulum apparatus to oscillate in a sinusoidal motion with forcing amplitude up to 10 mm and forcing frequency up to 30 Hz. The forcing amplitude and forcing frequency can be controlled by the function generator

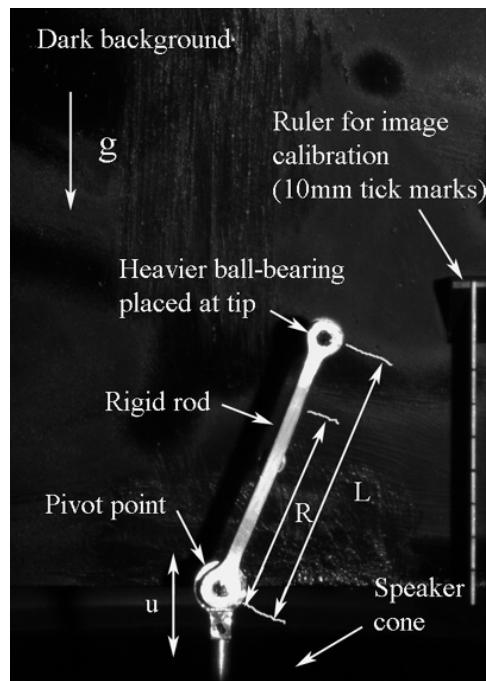


Figure 3.1: Single degree of freedom inverted pendulum experimental setup.

and the amplifier. During each experiment, a pre-assigned forcing amplitude and forcing frequency was applied to drive the speaker and the pendulum base in a sinusoidal vibration while the pendulum was released. Under certain initial conditions, the pendulum stabilizes around its upright position swinging periodically with left and right motion without falling over. We then documented this pendulum motion with different forcing parameters and initial conditions in a systematic way and captured the pendulum motion using a high speed camera.

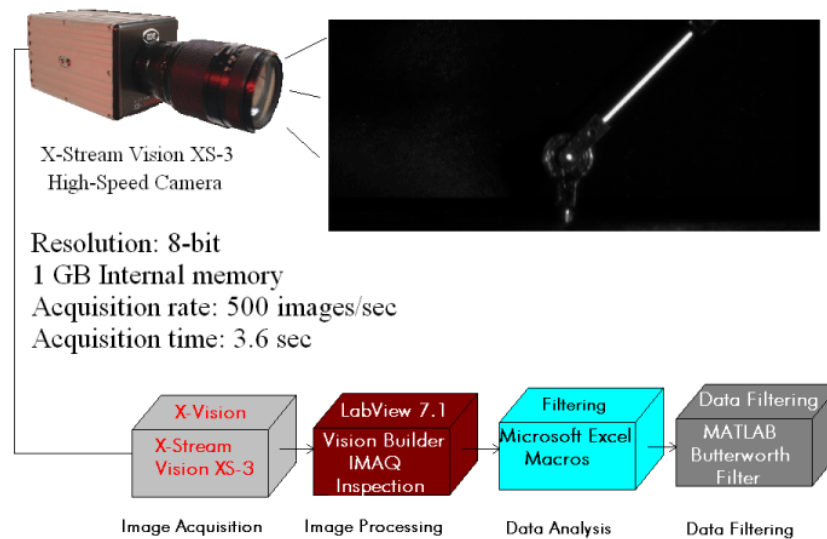


Figure 3.2: Precise experimental measurements from image acquisition and image processing using XS-3 high-speed camera, NI Vision Builder, MS Excel and Matlab.

### Inverted Pendulum Motion Using High Speed Camera

In capturing the dynamics of an inverted pendulum, we are interested in measuring the input of the periodic forcing to the pendulum base and the resulting effect of

the pendulum responses. By applying the optical measuring technique through high speed camera, we measured the pendulum's responses with high precision. Meanwhile, we avoided the problem of changing the sensitive inverted pendulum's dynamics from applying traditional mechanical measuring techniques which usually require some attachments from the sensors to the apparatus which often result in inducing system damping effects. One IDT X-Stream XS-3 high speed and high image resolution camera was used for our experimental measurements. This high speed camera has fixed image memory which we may trade in between of higher image resolution or longer recording time. We set the image resolution to  $1260 \times 288$  pixels with high camera frame rate which was recorded on 1G byte camera memory. The camera is capable of recording 3.6 seconds of data when setting the frame rate to 500 frames per second; 1.8 seconds of data when setting frame rate to 1000 frames per second.

Sensing by applying the optical properties of camera would eliminate additional friction forces which would often be induced by mechanical sensors. However, sensing by the camera requires a large amount of computational power in image processing which results in slower processing time. As shown in Figure 3.2, there were four major steps of image processes involved in our experimental measurements of the inverted pendulum: (a)Image acquisition by XVision using XS-3 high speed camera, (b)Image processing by NI Labview and NI Vision Builder, (c) Data analysis by Microsoft Excel, and (d)Data filtering by Matlab Butterworth filter.

The experimental setup was constructed as shown in Figure 3.3. An Agilent 33220A signal generator was used to generate sinusoidal forcing signal then a 100-Watt

PA amplifier was used to amplify the signal in order to drive the speaker so as to generate periodic vertical forcing to the pendulum base. Notice that the whole speaker setup was mounted to a solid platform in order to minimize the table vibration. The pendulum is capable of adding additional pendulum rods through the ball-bearing joint, therefore higher degree of freedom experiments can be conducted from sharing the same experimental equipment.

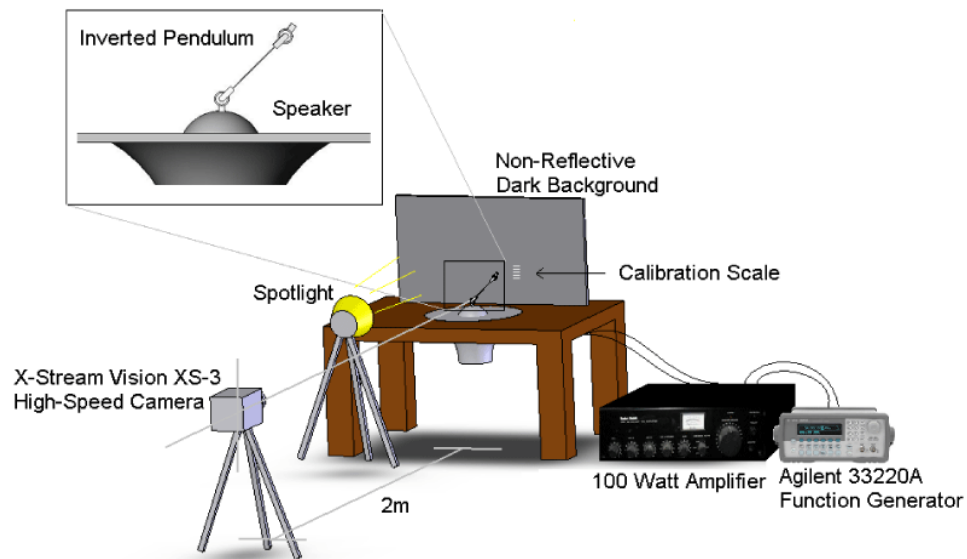


Figure 3.3: Three dimensional view of the SDOF experimental setup.

The motion of the pendulum was recorded by using an IDT X-Stream XS-3 high speed camera. To avoid image distortion from acquisition process, the camera view angle had been set to  $0^\circ$  with respect to the pendulum base and perpendicular to the pendulum's swinging  $XY$  plane. The distance between the camera front lens and the pendulum base was 2 m. The camera was set to acquire 8-bit resolution images in camera speed of 500

images per second and 1000 images per second. In order to enhance the image quality for better image analysis results, the rod of the pendulum and the pivot point on the base were painted with a reflective white paint, while the rest of the apparatus was painted with a non-reflective black coating to reduce glare. A ruler with a reflective white paint on its front face and black coating on the tick marks was mounted in a fixed location vertically onto the same pendulum moving plane. The distance between two tick marks on the ruler was 10 mm away. As shown in Figure 3.1, the ruler had two important functions: one is to calibrate the images captured from high speed camera that we used the tick marks on the ruler to convert the pendulum size from image pixels to physical engineering unit in mm; the other function is to use the ruler to measure the pendulum's angle where parallel to the ruler indicates  $0^\circ$  pendulum angle. Also, there was a DC powered truck headlight used to illuminate the apparatus in order to get better image quality.

### **System Calibration and Image Processing by NI Vision Builder**

Since there were huge number of images captured by high speed camera taken from each experimental trial, it required some image processing steps to convert the image information into proper physical measurements. We applied NI Vision Builder image processing software to get our experimental results. NI Vision Builder can detect color(or brightness) difference from an digital image, the shape of an object defined by different color(or brightness) captured from the camera can then be distinguished. From scanning through a sequence of images from the same shape detecting algorithm in this software, we may get the time evolution of the shape changes which we defined as motion of an object. Figure 3.4 shows a snap shot of a single image of a single degree of freedom inverted pendu-

lum in motion. Notice that the camera being mounted in a  $90^\circ$  angle in Figure 3.4 in order to get wider camera view from different aspect ratio to capture larger pendulum's motion. The high speed camera provide black and white images with gray scale color and gradient brightness to distinguish the shape of the inverted pendulum. We first applied NI Vision Builder to make more contrast to the image to enhance the image quality. The result is shown as in Figure 3.4, the inverted pendulum shows in white color which clearly separated from the black color background. Then we defined an algorithm from NI Vision Builder to detect the shape of the pendulum base which we can assign a moving coordinate to follow the base's motion. We can then get the measurements of the pendulum base's motion in digital pixel coordinate as a function of image frames, later we converted this information into the time trace of the pendulum's motion in engineering unit using mm/s. One of the zoom-in view of the pendulum base's motion is shown in Figure 3.5. Notice that we made use of a ruler with tick marks of 10 mm to calibrate the image which can be seen from the top portion of Figure 3.4. Similarly, we detected the pendulum angle from capturing one of its straight edges in comparison of the vertical straight line provided from the ruler in the fixed location. Those green boxes in Figure 3.4 indicate the regions of interest of the image process. Therefore, all pendulum's responses and the forcing parameters captured from high speed camera can be measured precisely through above image process techniques.

### **Data Analysis and Data Filtering**

Figure 3.5 shows the data points of the zoom-in view of one of the pendulum's base motion. The  $Y$  signal in Figure 3.5 measured the pendulum's vertical motion which indicated that this pendulum was under sinusoidal forcing with amplitude of  $8.5 \pm 0.2$  mm

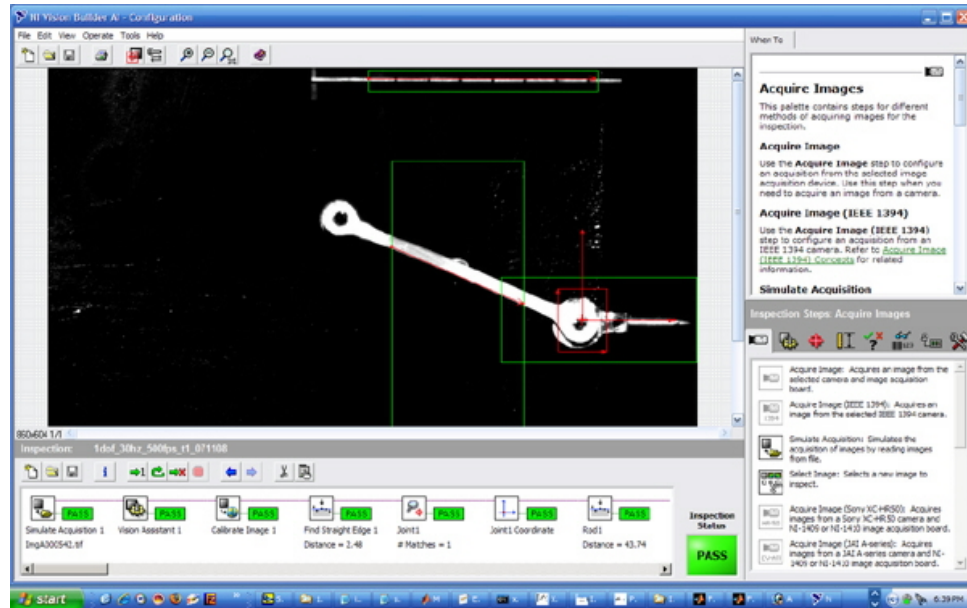


Figure 3.4: NI Vision Bulider software applied to a single degree of freedom experimental setup.

and frequency of  $25.0 \pm 0.1$  Hz. The  $X$  signal in Figure 3.5 measured the pendulum's horizontal motion which indicated the pendulum's base had small horizontal motion  $X = 0.0 \pm 0.1$  mm. Notice that Figure 3.5 indicated that the high speed camera had acquisition rate at 500 frames per second which had 50 images or data points shown within 0.1 second of time period.

There were high frequency noise induced from data acquisition and image processing steps. Experimental raw data cannot be properly analyzed without data filtering. In this paper, we applied Butterworth digital filter using Matlab to convert noisy raw signal into cleaner waveforms. Image data acquisition had sampling frequency at 500 Hz, therefore it's Nyquist frequency was at 250 Hz. We applied  $10^{th}$  order lowpass digital Butterworth filter to all of our experimental data with cutoff frequency being set to 15% of Nyquist

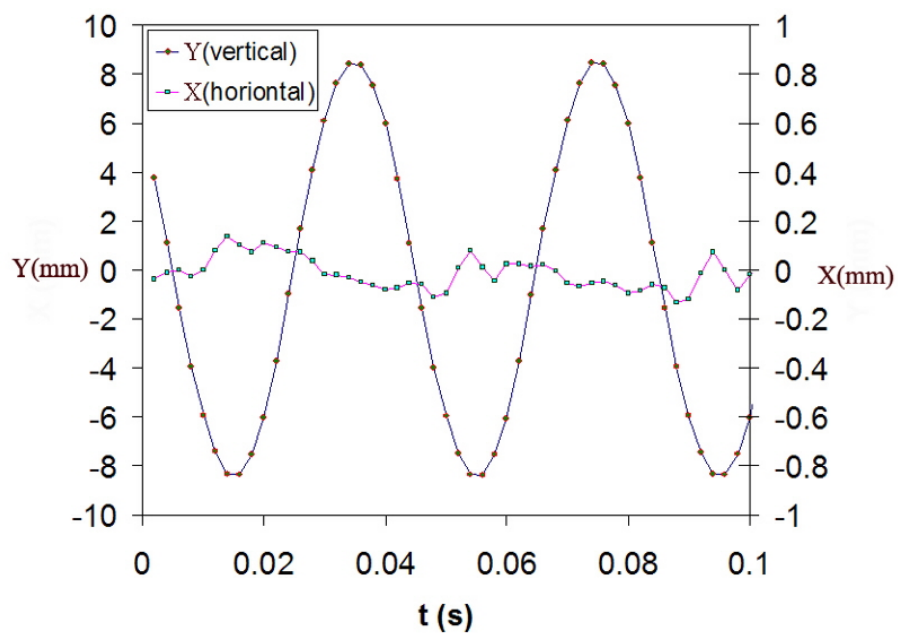


Figure 3.5: Zoom-in view of experimental data of inverted pendulum base motion.  $X$  denotes vertical periodic forcing displacement which has coordinate  $u(t) = \varepsilon \cos \omega t$ ;  $Y$  denotes horizontal motion.

frequency.

### 3.2 Single Degree of Freedom System Experimental Results

Below are graphs of our experimental results on *s*DOF inverted pendulum as described in Figure 3.1. In Figure 3.6, the pendulum was under sinusoidal forcing with amplitude  $10.0 \pm 0.2$  mm and frequency  $25.0 \pm 0.1$  Hz. We normalized the forcing amplitude and forcing frequency by the pendulum's length and its natural frequency in order to compare with our numerical simulation results. The system has normalized amplitude  $\bar{\epsilon} = 0.14 \pm 0.01$  and normalized frequency  $\bar{\omega} = 13.3 \pm 0.2$ . Under 500 Hz of high speed camera acquisition rate, we measured the pendulum's response in high resolution. In part (a) of Figure 3.6 shows the pendulum's vertical forcing with comparison to the pendulum's response. It indicates that the input forcing was in periodic pattern near sinusoidal motion which resulted in a near periodic pendulum response. In part (b),(c),(d),(e),(f) of Figure 3.6 there are two parts of system response, the top graph indicates the raw data points while the bottom indicates the filtered data points by applying Butterworth filter. Notice from the graphs, the filtered data shown much cleaner results compare with raw data, especially in the system phase portrait graph in (e), the raw phase portrait cannot conclude much while the filtered phase portrait shows clear near periodic pattern. There were some damping effect being detected from our measurements as in (c) of Figure 3.6. The system time trace in (c) shows that the inverted pendulum's response had smaller and smaller amplitude in later timing. This damping effect also implied that the pendulum's response may eventually stabilized in its upright vertical position and the system was asymptotically stable with the damping

effect. This result is different compare with our numerical simulation result in which we neglect damping through out. In (e), the system phase portrait shows symmetric pattern which also indicates the frequency ratio  $N_r$  should be an even number. This pendulum was swinging in a special near periodic pattern which we characterized as 14 : 1 frequency ratio pattern. This experimental results matched with our numerical simulation results described in earlier sections. In (f) of Figure 3.6 shows the power spectral density graph to extract the harmonic components of the pendulum response. In (f), it indicates that there was a slow time response greater than 1 Hz and the next obvious peak happened at 25 Hz which is corresponding to the sinusoidal forcing input and the fast system time.

In Figure 3.7, the pendulum was under sinusoidal forcing with amplitude  $8.0 \pm 0.3$  mm and frequency  $25.0 \pm 0.1$  Hz. Similar to previous discussion, we normalized the forcing amplitude and forcing frequency by the pendulum's length and its natural frequency in order to compare with our numerical simulation results. The system has normalized amplitude  $\bar{\epsilon} = 0.11 \pm 0.01$  and normalized frequency  $\bar{\omega} = 13.3 \pm 0.2$ . Under 500 Hz of high speed camera acquisition rate, we measured the pendulum's response in high resolution. In part (a) of Figure 3.7 shows the pendulum's vertical forcing with comparison to the pendulum's response. It indicates that the input forcing was in periodic pattern near sinusoidal motion which resulted in a near periodic pendulum response. In part (b),(c),(d),(e),(f) of Figure 3.7 there are two parts of system response, the top graph indicates the raw data points while the bottom indicates the filtered data points by applying Butterworth filter. Notice from the graphs, the filtered data shown much cleaner results compare with raw data, especially in the system phase portrait graph in (e), the raw phase portrait cannot conclude much

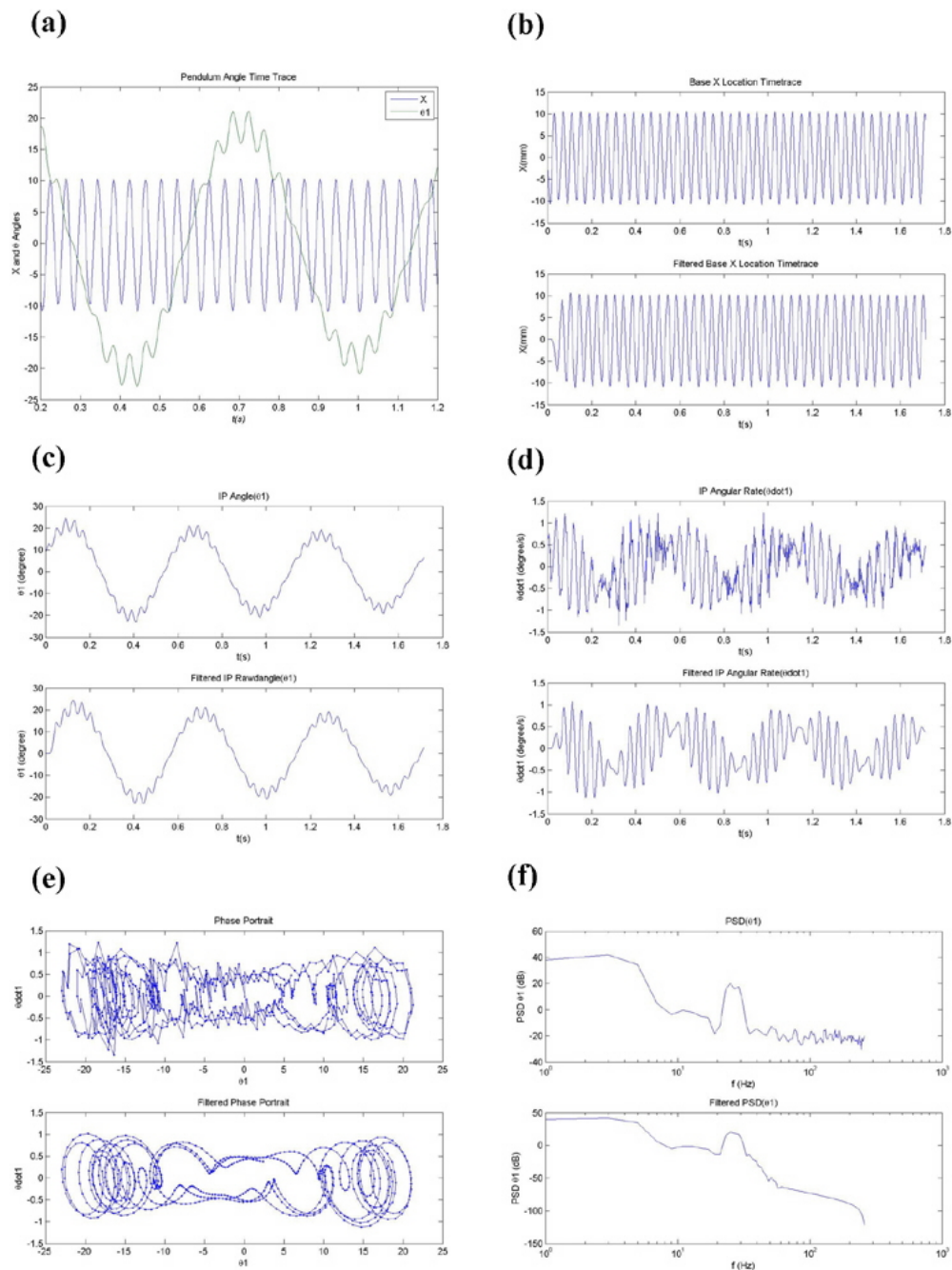


Figure 3.6: Experiment on single degree of freedom pendulum under  $10.0 \pm 0.2$  mm driving amplitude and 25 Hz driving frequency. System has normalized amplitude  $\bar{\varepsilon} = 0.14 \pm 0.01$  and normalized frequency  $\bar{\omega} = 13.3 \pm 0.2$ .

while the filtered phase portrait shows clear near periodic pattern. There were some damping effect being detected from our measurements as in (c) of Figure 3.7. The system time trace in (c) shows that the inverted pendulum's response had smaller and smaller amplitude in later timing. This damping effect also implied that the pendulum's response may eventually stabilized in its upright vertical position and the system was asymptotically stable with the damping effect. This result is different compare with our numerical simulation result in which we neglect damping through out. In (e), the system phase portrait shows symmetric pattern which also indicates the frequency ratio  $N_r$  should be an even number. This pendulum was swinging in a special near periodic pattern which we characterized as 30 : 1 frequency ratio pattern. This experimental results also matched with our numerical simulation results described in earlier sections. In (f) of Figure 3.7 shows the power spectral density graph to extract the harmonic components of the pendulum response. In (f), it indicates that there was a slow time response around 1 Hz and the next obvious peak happened at 25 Hz which is corresponding to the sinusoidal forcing input and the fast system time.

In Figure 3.8, the pendulum was under sinusoidal forcing with amplitude  $6.5 \pm 0.3$  mm and frequency  $30.0 \pm 0.1$  Hz. Similar to previous discussion, we normalized the forcing amplitude and forcing frequency by the pendulum's length and its natural frequency in order to compare with our numerical simulation results. The system has normalized amplitude  $\bar{\epsilon} = 0.09 \pm 0.01$  and normalized frequency  $\bar{\omega} = 15.9 \pm 0.2$ . Under 500 Hz of high speed camera acquisition rate, we measured the pendulum's response in high resolution. In part (a) of Figure 3.8 shows the pendulum's vertical forcing with comparison to the pendulum's response. It indicates that the input forcing was in periodic pattern near sinusoidal motion

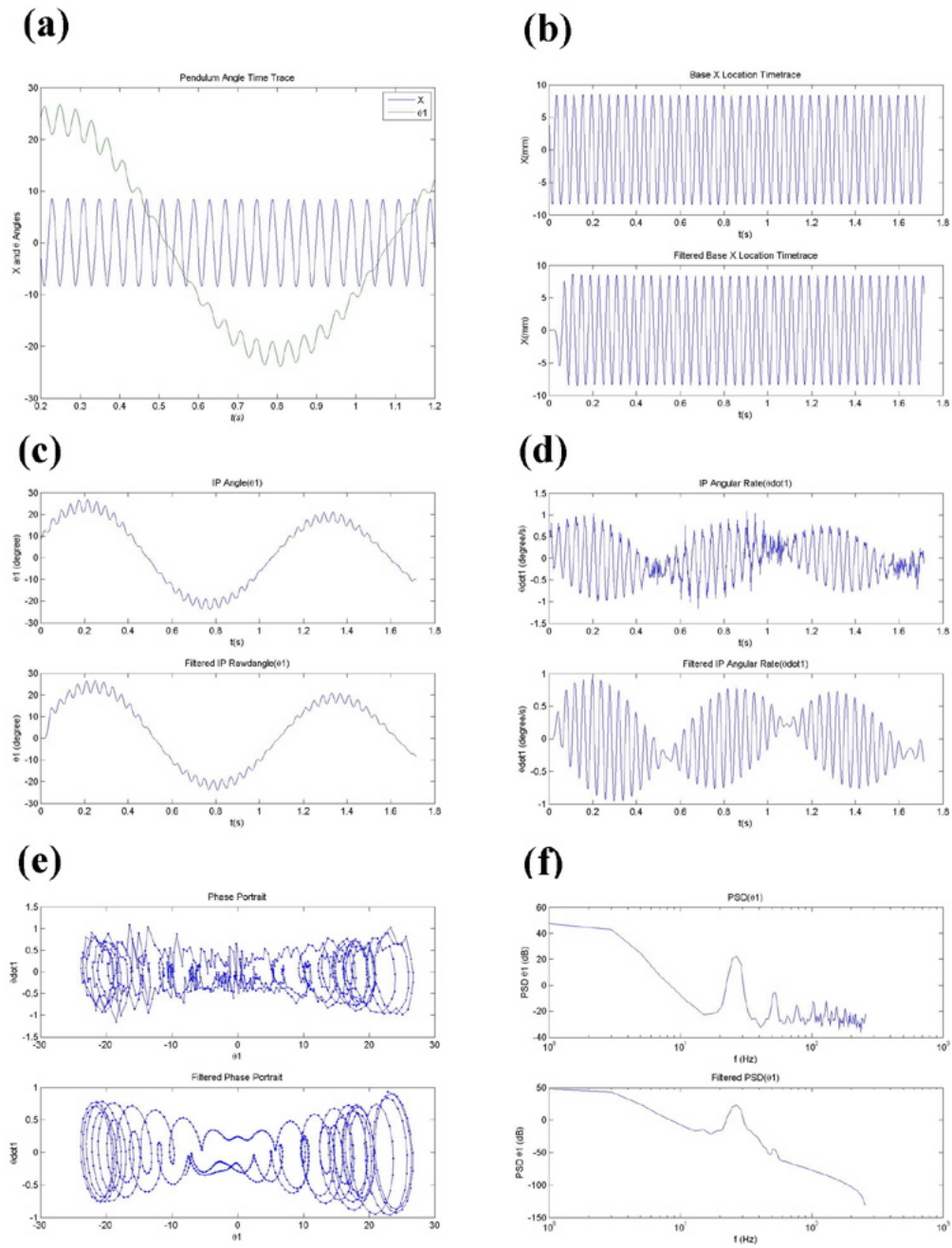


Figure 3.7: Experiment on single degree of freedom pendulum under  $8.0 \pm 0.3$  mm driving amplitude and 25 Hz driving frequency. System has normalized amplitude  $\bar{\epsilon} = 0.11 \pm 0.01$  and normalized frequency  $\bar{\omega} = 13.3 \pm 0.2$ .

which resulted in a near periodic pendulum response. In part (b),(c),(d),(e),(f) of Figure 3.8 there are two parts of system response, the top graph indicates the raw data points while the bottom indicates the filtered data points by applying Butterworth filter. Notice from the graphs, the filtered data shown much cleaner results compare with raw data, especially in the system phase portrait graph in (e), the raw phase portrait cannot conclude much while the filtered phase portrait shows clear near periodic pattern. There were some damping effect being detected from our measurements as in (c) of Figure 3.8. The system time trace in (c) shows that the inverted pendulum's response had smaller and smaller amplitude in later timing. This damping effect also implied that the pendulum's response may eventually stabilized in its upright vertical position and the system was asymptotically stable with the damping effect. This result is different compare with our numerical simulation result in which we neglect damping through out. In (e), the system phase portrait shows symmetric pattern which also indicates the frequency ratio  $N_r$  should be an even number. This pendulum was swinging in a special near periodic pattern which we characterized as 36 : 1 frequency ratio pattern. This experimental results also matched with our numerical simulation results described in earlier sections. In (f) of Figure 3.8 shows the power spectral density graph to extract the harmonic components of the pendulum response. In (f), it indicates that there was a slow time response around 1 Hz and the next obvious peak happened at 30 Hz which is corresponding to the sinusoidal forcing input and the fast system time.

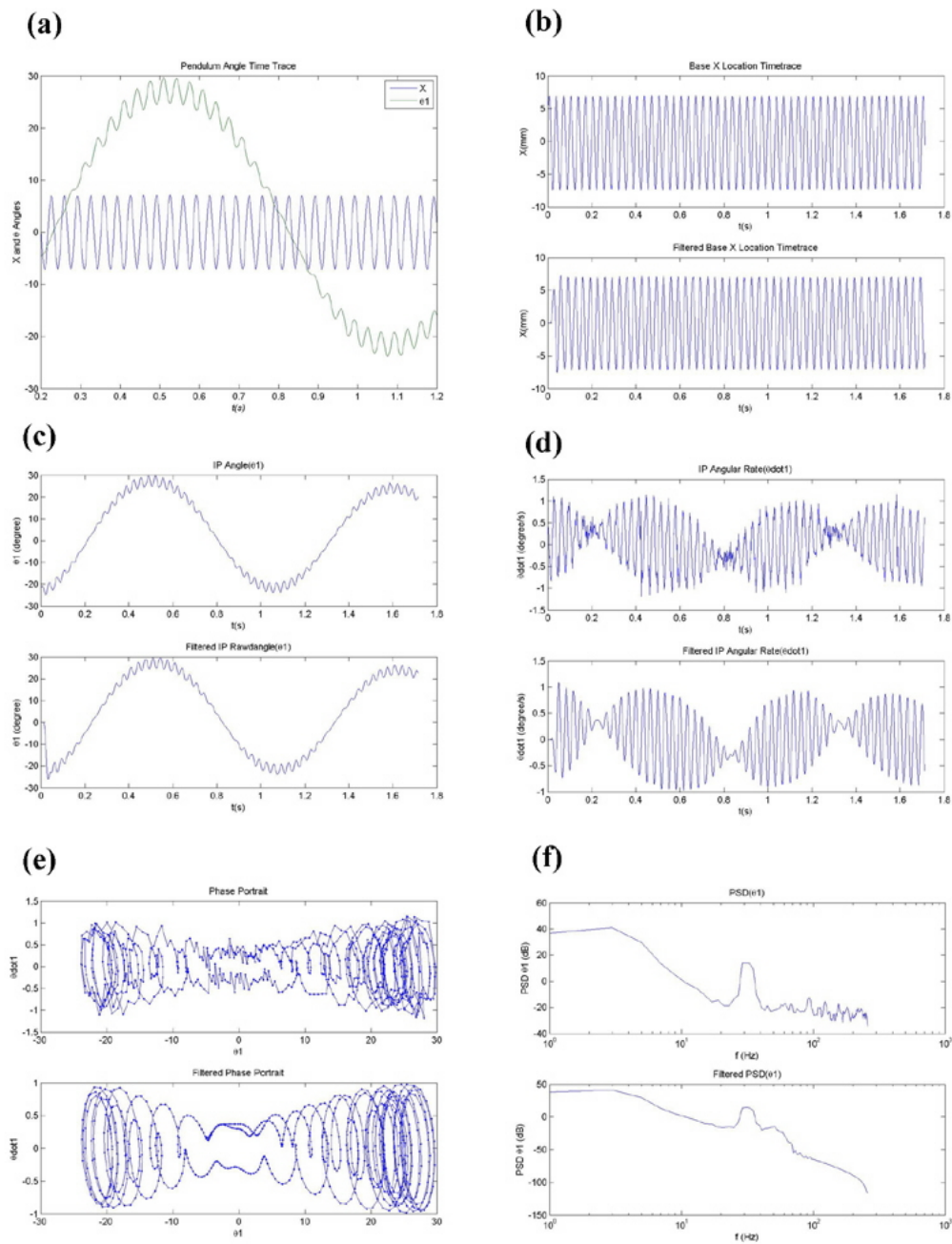


Figure 3.8: Experiment on single degree of freedom pendulum under  $6.5 \pm 0.3$  mm driving amplitude and 30 Hz driving frequency. System has normalized amplitude  $\bar{\epsilon} = 0.09 \pm 0.01$  and normalized frequency  $\bar{\omega} = 15.9 \pm 0.2$ .

## Chapter 4

# Multiple Degree of Freedom

# Inverted Pendulum Model

The multiple degree of freedom model supports different effects than the single degree of freedom case. In this paper, we first considered the general  $n$  degree of freedom inverted pendulum model under periodic vertical forcing at its base. In later sections, we validated  $s$ DOF and 2DOF models from assigning  $n = 1$  and  $n = 2$  to our  $n$  degree of freedom inverted pendulum model.

### 4.1 Formulate $n$ DOF System Equation of Motion From Lagrangian Approach

Consider a  $n$ DOF inverted pendulum as shown in Figure 4.1 under planer motion with respect to a fixed two dimensional coordinate  $X - Y$ . The inverted pendulum consists of  $n$  point masses which connect to each other by  $n$  rigid weightless rods. Assume each

joint is free to rotate on the  $X - Y$  plane without any friction or damping force. The base of the inverted pendulum is subject to vertical oscillatory forcing with vertical periodic displacement  $h(t) = \varepsilon \cos \omega t$ . For convenience we setup a sub-coordinate  $x - y$  which has its origin  $(x_0, y_0)$  located on the inverted pendulum's base. The  $n$  masses labelled from the first joint counting from the base as  $m_1, m_2, \dots, m_k, \dots, m_n$  with length of their rods label as  $l_1, l_2, \dots, l_k, \dots, l_n$ . Each point mass has their coordinate with respect to the inertial frame written as  $(x_1, y_1), (x_2, y_2), \dots, (x_k, y_k), \dots, (x_n, y_n)$ . The inverted pendulum's motion can be described by the time evolution of the angles of the pendulum rods with respect to upright vertical position of the inertial frame and the pendulum's angles are labelled as  $\theta_1(t), \theta_2(t), \theta_3(t), \dots, \theta_n(t)$  respectively. The whole system is under the Earth's gravitational acceleration  $g$  which is point downward.

We can write the coordinate of each mass as

$$x_1 = x_0 + l_1 \sin \theta_1,$$

$$y_1 = y_0 + h(t) + l_1 \cos \theta_1,$$

$$x_2 = x_0 + l_1 \sin \theta_1 + l_2 \sin \theta_2,$$

$$y_2 = y_0 + h(t) + l_1 \cos \theta_1 + l_2 \cos \theta_2,$$

...

$$x_n = x_0 + l_1 \sin \theta_1 + \dots + l_n \sin \theta_n = \sum_{i=1}^n l_i \sin \theta_i,$$

$$y_n = y_0 + h(t) + l_1 \cos \theta_1 + \dots + l_n \cos \theta_n = h(t) + \sum_{i=1}^n l_i \cos \theta_i.$$

Taking time derivatives to the above equations we may get velocity components of each joint as

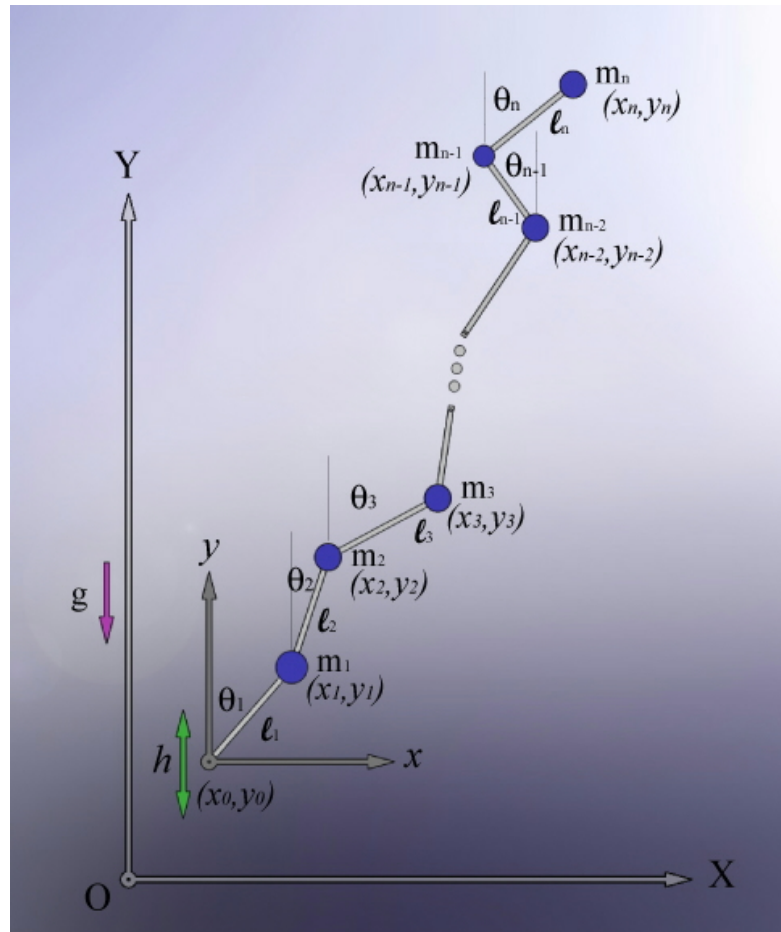


Figure 4.1: Geometric relationship of general case nDOF inverted pendulum. under vertical oscillatory forcing at its base

$$\begin{aligned}
\dot{x}_1 &= l_1 \dot{\theta}_1 \cos \theta_1, \\
\dot{y}_1 &= \dot{h}(t) - l_1 \dot{\theta}_1 \sin \theta_1, \\
\dot{x}_2 &= l_1 \dot{\theta}_1 \cos \theta_1 + l_2 \dot{\theta}_2 \cos \theta_2, \\
\dot{y}_2 &= \dot{h}(t) - l_1 \dot{\theta}_1 \sin \theta_1 - l_2 \dot{\theta}_2 \sin \theta_2, \\
&\dots \\
\dot{x}_n &= l_1 \dot{\theta}_1 \cos \theta_1 + l_2 \dot{\theta}_2 \cos \theta_2 + \dots + l_n \dot{\theta}_n \cos \theta_n = \sum_{i=1}^n l_i \dot{\theta}_i \cos \theta_i, \\
\dot{y}_n &= \dot{h}(t) - l_1 \dot{\theta}_1 \sin \theta_1 - l_2 \dot{\theta}_2 \sin \theta_2 - \dots - l_n \dot{\theta}_n \sin \theta_n = \dot{h}(t) - \sum_{i=1}^n l_i \dot{\theta}_i \sin \theta_i.
\end{aligned}$$

Therefore, the potential energy for  $n$ -DOF inverted pendulum can be expressed as

$$\begin{aligned}
V_n &= m_1 g y_1 + m_2 g y_2 + \dots + m_n g y_n, \\
&= g \left[ h(t) \sum_{i=1}^n m_i + \sum_{i=1}^n \sum_{j=1}^n m_j l_i \cos \theta_i \right].
\end{aligned} \tag{4.1}$$

Kinetic energy for  $n$ -DOF inverted pendulum can be expressed as

$$\begin{aligned}
T_n &= \frac{m_1}{2} (\dot{x}_1^2 + \dot{y}_1^2) + \frac{m_2}{2} (\dot{x}_2^2 + \dot{y}_2^2) + \dots + \frac{m_n}{2} (\dot{x}_n^2 + \dot{y}_n^2), \\
&= \frac{1}{2} \sum_{i=1}^n m_i \left[ \begin{aligned} &\dot{h}^2(t) - 2\dot{h}(t) \sum_{j=1}^i l_j \dot{\theta}_j \sin \theta_j \\ &+ 2 \sum_{j=1}^{i-1} l_j l_{j+1} \dot{\theta}_j \dot{\theta}_{j+1} \cos(\theta_j - \theta_{j+1}) + 2l_i l_1 \dot{\theta}_i \dot{\theta}_1 \cos(\theta_i - \theta_1) + \sum_{j=1}^i l_j^2 \dot{\theta}_j^2 \end{aligned} \right].
\end{aligned} \tag{4.2}$$

The inverted pendulum's equation of motion can then be derived by means of Lagrange's equation applying energy conservation law. For  $n$ -DOF system it requires  $n$  sets of Lagrange's equations to describe the whole system's dynamic. We may write the  $k^{th}$  Lagrange's equation as

$$\frac{d}{dt} \left( \frac{\partial L_n}{\partial \dot{\theta}_k} \right) - \frac{\partial L_n}{\partial \theta_k} = 0. \quad (4.3)$$

The system has  $n$  states  $\theta_1, \theta_2, \theta_3, \dots, \theta_n$ . In (4.3),  $\theta_k$  denotes the  $k^{th}$  component of the states and  $\dot{\theta}_k$  denotes the  $k^{th}$  angular velocity component. The Lagrangian function defined as  $L_n = T_n - V_n$  which is simply the system kinetic energy subtracts by the system potential energy. Lagrange's equation describes the motion generated from the system kinetic energy will later become the system potential energy; the system potential energy will also transfer perfectly into kinetic energy then some motions being introduced. Lagrange's equation is bases on the energy conservation law where no energy being generated nor dissipated in a system. Unlike the Lagrange's equation as in (2.2) described in earlier section that the vertical forcing being treated as nonconservative forces, our new system has the vertical forcing shown explicitly inside its kinetic energy. Dealing with conservative Lagrange's equation will benefit from solving only homogeneous differential equations which results in much lighter calculation cost. Refer to [62] and [61], Weibel and Baillieul introduced a more compact form of Lagrangian equation to their  $n$  degree of freedom normal pendulum ( $\theta_k$  angles are measured from downward vertical) under a rapidly forced cart on an inclined plane. We applied the compact form of Lagrangian equation to our  $n$ -DOF inverted pendulum as follow:

$$L_n(Q, \dot{Q}; v) = \underbrace{\frac{1}{2} \dot{Q}^T M(Q) \dot{Q} + v A(Q)^T \dot{Q}}_{\text{Kinetic Energy}} - \underbrace{V(Q)}_{\text{Potential Energy}}. \quad (4.4)$$

The Lagrangian equation shown in (4.4) has no difference compare with the Lagrangian function calculated from our previous derivation on system kinetic energy and potential energy in (4.2) and (4.1) respectively. However, detail break down components of

system kinetic energy variation can be shown in more clear way in (4.4). As described in (4.4), the system kinetic energy is composed of two parts: the effect of system inertial and the effect of vertical periodic forcing. Here  $Q^T = [ \theta_1 \ \theta_2 \ \theta_3 \ \dots \ \theta_n ] \in \mathbb{R}^n$  denotes the states of the system.  $\dot{Q}$  is time derivative of  $Q$  denotes the angular velocity of the states.  $v$  is the velocity component due to vertical periodic forcing and is described as

$$v(t) = \dot{h}(t) = -\varepsilon\omega \sin \omega t. \quad (4.5)$$

$M(Q) \in \mathbb{R}^{n \times n}$  is a state-dependent inertia tensor can be described in matrix form as:

$$M(Q) = \begin{bmatrix} M_{11}(\theta) & M_{12}(\theta) & \cdot & \cdot & M_{1n}(\theta) \\ M_{21}(\theta) & \cdot & & & \cdot \\ \cdot & & \cdot & & \cdot \\ \cdot & & & \cdot & \cdot \\ M_{n1}(\theta) & \cdot & \cdot & \cdot & M_{nn}(\theta) \end{bmatrix} \quad (4.6)$$

where the components inside can be described as

$$M_{ij}(\theta) = \left( \sum_{k=\max(i,j)}^n m_k \right) l_i l_j \cos(\theta_i - \theta_j). \quad (4.7)$$

$A(Q) \in \mathbb{R}^n$  is known as Coriolis coupling vector which describes the vertical forcing affect the kinetic energy of the system.

$$A(Q)^T = \begin{bmatrix} A_1(\theta) & A_2(\theta) & A_3(\theta) & \dots & A_n(\theta) \end{bmatrix} \quad (4.8)$$

where the components inside can be described as

$$A_i(\theta) = \left( \sum_{k=1}^n m_k \right) l_i \sin \theta_i. \quad (4.9)$$

The system potential energy  $V(Q) \in \mathbb{R}$  depends only on the states of system and can be described as

$$V(Q) = \sum_{i=1}^n \left[ \left( \sum_{k=i}^n m_k \right) gl_i (\cos \theta_i - 1) \right]. \quad (4.10)$$

Although the general Lagrangian equation (4.4) is not necessarily conserved for arbitrary forcing input  $v$ , the system can be considered conserved under periodic forcing. This had been pointed out by Weibel and Baillieul in [62],[61]. Our system only concern on the effect of periodic forcing where  $v(t+T) = v(t)$  for some  $T > 0$ . In [62] and [61], Weibel and Baillieul introduced the concept of controller Hamiltonian  $H(Q, P; v)$  corresponding to (4.4) via the Legendre transformation  $H(Q, P; v) = P^T \dot{Q} - L_n$  where  $P^T = \begin{bmatrix} P_1 & P_2 & P_3 & \dots & P_n \end{bmatrix}$  are canonical momenta defined by  $P = \frac{\partial L_n}{\partial \dot{Q}}$ . They concluded that for periodic forcing the controller Hamiltonian  $H(Q, P; v)$  can be averaged over one period of  $v(t)$  to obtain the averaged Hamiltonian which results in a proper Hamiltonian described as  $\frac{\partial H}{\partial t} = 0$ . The system can then be considered conserved thru averaging principle.

In later sections, we will first verify the single degree of freedom model by applying  $n = 1$  to our  $n$  degree of freedom model and compare that to our earlier work as shown in (2.12). Two degree of freedom system will then being introduced after by applying  $n = 2$  to our  $n$  degree of freedom model. Results on numerical simulation and experimentation of two degree of freedom system will be shown in later chapters and detailed comparison will then be performed.

## 4.2 Validate the Single Degree of Freedom Inverted Pendulum Model

Apply  $n = 1$  to (4.6), (4.8) and (4.10), we have

$$Q^T = [\theta_1], \quad (4.11)$$

$$M(Q) = [M_{11}(\theta_1)] = m_1 l_1^2, \quad (4.12)$$

$$A(Q) = [A_1(\theta_1)] = m_1 l_1 \sin \theta_1, \quad (4.13)$$

$$V(Q) = m_1 g l_1 (\cos \theta_1 - 1). \quad (4.14)$$

Therefore, the single degree of freedom system Lagrangian equation can be expressed as

$$L_1(Q, \dot{Q}; v) = \frac{1}{2} m_1 l_1^2 \dot{\theta}_1^2 - (\varepsilon \omega \sin \omega t) (m_1 l_1 \sin \theta_1) \dot{\theta}_1 - m_1 g l_1 (\cos \theta_1 - 1). \quad (4.15)$$

Derive  $\frac{\partial L_1}{\partial \theta_1}$ ,  $\frac{\partial L_1}{\partial \dot{\theta}_1}$  and  $\frac{d}{dt} \left( \frac{\partial L_1}{\partial \dot{\theta}_1} \right)$  as follow:

$$\frac{\partial L_1}{\partial \theta_1} = -m_1 l_1 \dot{\theta}_1 (\varepsilon \omega \sin \omega t) \cos \theta_1 + m_1 g l_1 \sin \theta_1, \quad (4.16)$$

$$\frac{\partial L_1}{\partial \dot{\theta}_1} = m_1 l_1^2 \dot{\theta}_1 - (\varepsilon \omega \sin \omega t) m_1 l_1 \sin \theta_1, \quad (4.17)$$

$$\frac{d}{dt} \left( \frac{\partial L_1}{\partial \dot{\theta}_1} \right) = m_1 l_1^2 \ddot{\theta}_1 - (\varepsilon \omega^2 \cos \omega t) m_1 l_1 \sin \theta_1 - (\varepsilon \omega \sin \omega t) m_1 l_1 \dot{\theta}_1 \cos \theta_1, \quad (4.18)$$

The Lagrange's equation becomes

$$\frac{d}{dt} \left( \frac{\partial L_1}{\partial \dot{\theta}_1} \right) - \frac{\partial L_1}{\partial \theta_1} = m_1 l_1^2 \ddot{\theta}_1 - m_1 l_1 (g + \varepsilon \omega^2 \cos \omega t) \sin \theta_1 = 0. \quad (4.19)$$

We may divide both sides of (4.19) by  $m_1 l_1^2$  to make its leading coefficient equal to 1 yields

$$\ddot{\theta}_1 - (g + \varepsilon \omega^2 \cos \omega t) \frac{1}{l_1} \sin \theta_1 = 0. \quad (4.20)$$

The equation of motion in (4.20) is the same as in (2.12) derived from earlier sections.

### 4.3 Two Degree of Freedom Inverted Pendulum Model

Apply  $n = 2$  to (4.6), (4.8) and (4.10), we have

$$Q^T = \begin{bmatrix} \theta_1 & \theta_2 \end{bmatrix}, \quad (4.21)$$

$$\begin{aligned} M(Q) &= \begin{bmatrix} M_{11}(\theta) & M_{12}(\theta) \\ M_{13}(\theta) & M_{14}(\theta) \end{bmatrix} \\ &= \begin{bmatrix} (m_1 + m_2)l_1^2 & m_2l_1l_2 \cos(\theta_1 - \theta_2) \\ m_2l_1l_2 \cos(\theta_1 - \theta_2) & m_2l_2^2 \end{bmatrix}, \end{aligned} \quad (4.22)$$

$$\begin{aligned} A(Q) &= \begin{bmatrix} A_1 & A_2 \end{bmatrix} \\ &= \begin{bmatrix} (m_1 + m_2)l_1 \sin \theta_1 & m_2l_2 \sin \theta_2 \end{bmatrix}, \end{aligned} \quad (4.23)$$

$$V(Q) = (m_1 + m_2)gl_1(\cos \theta_1 - 1) + m_2gl_2(\cos \theta_2 - 1). \quad (4.24)$$

Substitute (4.21), (4.22), (4.23) and (4.24) into (4.4), the Lagrangian function of

two degree of freedom inverted pendulum model can be expressed as

$$\begin{aligned}
L_2(Q, \dot{Q}; v) &= \frac{1}{2} \begin{bmatrix} \dot{\theta}_1 & \dot{\theta}_2 \end{bmatrix} \begin{bmatrix} M_{11}(\theta) & M_{12}(\theta) \\ M_{13}(\theta) & M_{14}(\theta) \end{bmatrix} \begin{bmatrix} \dot{\theta}_1 \\ \dot{\theta}_2 \end{bmatrix} \\
&\quad + v \begin{bmatrix} A_1 & A_2 \end{bmatrix} \begin{bmatrix} \dot{\theta}_1 \\ \dot{\theta}_2 \end{bmatrix} \\
&\quad - V(Q), \\
&= \frac{1}{2} (m_1 + m_2) l_1^2 \dot{\theta}_1^2 + m_2 l_1 l_2 \dot{\theta}_1 \dot{\theta}_2 \cos(\theta_1 - \theta_2) + \frac{1}{2} m_2 l_2^2 \dot{\theta}_2^2 \\
&\quad - (\varepsilon \omega \sin \omega t) \left[ (m_1 + m_2) l_1 \dot{\theta}_1 \sin \theta_1 + m_2 l_2 \dot{\theta}_2 \sin \theta_2 \right] \\
&\quad - [(m_1 + m_2) g l_1 (\cos \theta_1 - 1) + m_2 g l_2 (\cos \theta_2 - 1)]. \tag{4.25}
\end{aligned}$$

Derive  $\frac{\partial L_2}{\partial \theta_1}$ ,  $\frac{\partial L_2}{\partial \dot{\theta}_1}$  and  $\frac{d}{dt} \left( \frac{\partial L_2}{\partial \dot{\theta}_1} \right)$  as follow:

$$\begin{aligned}
\frac{\partial L_2}{\partial \theta_1} &= -m_2 l_1 l_2 \dot{\theta}_1 \dot{\theta}_2 \sin(\theta_1 - \theta_2) - (\varepsilon \omega \sin \omega t) (m_1 + m_2) l_1 \dot{\theta}_1 \cos \theta_1 \\
&\quad + (m_1 + m_2) g l_1 \sin \theta_1, \tag{4.26}
\end{aligned}$$

$$\begin{aligned}
\frac{\partial L_2}{\partial \dot{\theta}_1} &= (m_1 + m_2) l_1^2 \dot{\theta}_1 + m_2 l_1 l_2 \dot{\theta}_2 \cos(\theta_1 - \theta_2) \\
&\quad - (\varepsilon \omega \sin \omega t) (m_1 + m_2) l_1 \sin \theta_1, \tag{4.27}
\end{aligned}$$

$$\begin{aligned}
\frac{d}{dt} \left( \frac{\partial L_2}{\partial \dot{\theta}_1} \right) &= (m_1 + m_2) l_1^2 \ddot{\theta}_1 + m_2 l_1 l_2 \ddot{\theta}_2 \cos(\theta_1 - \theta_2) \\
&\quad - m_2 l_1 l_2 \dot{\theta}_2 (\dot{\theta}_1 - \dot{\theta}_2) \sin(\theta_1 - \theta_2) \\
&\quad - (\varepsilon \omega^2 \cos \omega t) (m_1 + m_2) l_1 \sin \theta_1 \\
&\quad - (\varepsilon \omega \sin \omega t) (m_1 + m_2) l_1 \dot{\theta}_1 \cos \theta_1. \tag{4.28}
\end{aligned}$$

The first set of Lagrange's equation becomes

$$\begin{aligned}
\frac{d}{dt} \left( \frac{\partial L_2}{\partial \dot{\theta}_1} \right) - \frac{\partial L_2}{\partial \theta_1} &= (m_1 + m_2) l_1^2 \ddot{\theta}_1 - (g + \varepsilon \omega^2 \cos \omega t) (m_1 + m_2) l_1 \sin \theta_1 \\
&\quad + m_2 l_1 l_2 \left[ \ddot{\theta}_2 \cos (\theta_1 - \theta_2) + \dot{\theta}_2^2 \sin (\theta_1 - \theta_2) \right] \\
&= 0.
\end{aligned} \tag{4.29}$$

We may divide both sides of (4.29) by  $(m_1 + m_2) l_1^2$  to make its leading term  $\ddot{\theta}_1$  coefficient equal to 1 yields

$$\ddot{\theta}_1 - (g + \varepsilon \omega^2 \cos \omega t) \frac{1}{l_1} \sin \theta_1 + \frac{m_2 l_2}{(m_1 + m_2) l_1} \left[ \ddot{\theta}_2 \cos (\theta_1 - \theta_2) + \dot{\theta}_2^2 \sin (\theta_1 - \theta_2) \right] = 0. \tag{4.30}$$

Similarly, we may derive  $\frac{\partial L_2}{\partial \theta_2}$ ,  $\frac{\partial L_2}{\partial \dot{\theta}_2}$  and  $\frac{d}{dt} \left( \frac{\partial L_2}{\partial \dot{\theta}_2} \right)$  as follow:

$$\begin{aligned}
\frac{\partial L_2}{\partial \theta_2} &= m_2 l_1 l_2 \dot{\theta}_1 \dot{\theta}_2 \sin (\theta_1 - \theta_2) - (\varepsilon \omega \sin \omega t) m_2 l_2 \dot{\theta}_2 \cos \theta_2 \\
&\quad + m_2 g l_2 \sin \theta_2,
\end{aligned} \tag{4.31}$$

$$\frac{\partial L_2}{\partial \dot{\theta}_2} = m_2 l_1 l_2 \dot{\theta}_1 \cos (\theta_1 - \theta_2) + m_2 l_2^2 \dot{\theta}_2 - (\varepsilon \omega \sin \omega t) m_2 l_2 \sin \theta_2, \tag{4.32}$$

$$\begin{aligned}
\frac{d}{dt} \left( \frac{\partial L_2}{\partial \dot{\theta}_2} \right) &= m_2 l_1 l_2 \ddot{\theta}_1 \cos (\theta_1 - \theta_2) - m_2 l_1 l_2 \dot{\theta}_1 \left( \dot{\theta}_1 - \dot{\theta}_2 \right) \sin (\theta_1 - \theta_2) \\
&\quad + m_2 l_2^2 \ddot{\theta}_2 - (\varepsilon \omega^2 \cos \omega t) m_2 l_2 \sin \theta_2 \\
&\quad - (\varepsilon \omega \sin \omega t) m_2 l_2 \dot{\theta}_2 \cos \theta_2.
\end{aligned} \tag{4.33}$$

The second set of Lagrange's equation becomes

$$\begin{aligned}
\frac{d}{dt} \left( \frac{\partial L_2}{\partial \dot{\theta}_2} \right) - \frac{\partial L_2}{\partial \theta_2} &= m_2 l_1 l_2 \ddot{\theta}_1 \cos (\theta_1 - \theta_2) - m_2 l_1 l_2 \dot{\theta}_1^2 \sin (\theta_1 - \theta_2) \\
&\quad + m_2 l_2^2 \ddot{\theta}_2 - (\varepsilon \omega^2 \cos \omega t) m_2 l_2 \sin \theta_2 - m_2 g l_2 \sin \theta_2 \\
&= 0.
\end{aligned} \tag{4.34}$$

We may divide both sides of (4.34) by  $m_2 l_2^2$  to make its leading term  $\ddot{\theta}_2$  coefficient equal to 1 yields

$$\ddot{\theta}_2 - (g + \varepsilon \omega^2 \cos \omega t) \frac{1}{l_2} \sin \theta_2 + \frac{l_1}{l_2} \left[ \ddot{\theta}_1 \cos(\theta_1 - \theta_2) - \dot{\theta}_1^2 \sin(\theta_1 - \theta_2) \right] = 0. \quad (4.35)$$

Therefore, two sets of equations (4.30) and (4.35) describe the dynamic of two degree of freedom inverted pendulum under vertical periodic forcing. However, these two sets of equations are not written in a conventional form which has two highest order states in the same equation. For the convenience of applying conventional numerical simulation tools, we may further simplified two sets of equations (4.30) and (4.35) into general formats. First set of simplified equation can be obtained from (4.30) subtract (4.35) multiple by  $\frac{l_2}{l_1} \frac{m_2}{(m_1+m_2)}$  and then divide both sides of equation by its leading coefficient  $1 - \left( \frac{m_2}{m_1+m_2} \right) \cos^2(\theta_1 - \theta_2)$ , yields

$$\ddot{\theta}_1 - (g + \varepsilon \omega^2 \cos \omega t) (\Lambda_{11} \sin \theta_1 + \Lambda_{12} \sin \theta_2) + \Lambda_{13} \dot{\theta}_1^2 + \Lambda_{14} \dot{\theta}_2^2 = 0. \quad (4.36)$$

The coefficients inside (4.36) are

$$\Lambda_{11} = \frac{\frac{1}{l_1}}{\left[ 1 - \left( \frac{m_2}{m_1+m_2} \right) \cos^2(\theta_1 - \theta_2) \right]}, \quad (4.37)$$

$$\Lambda_{12} = \frac{\frac{1}{l_1} \frac{m_2}{(m_1+m_2)} \cos(\theta_1 - \theta_2)}{\left[ 1 - \left( \frac{m_2}{m_1+m_2} \right) \cos^2(\theta_1 - \theta_2) \right]}, \quad (4.38)$$

$$\Lambda_{13} = \frac{\frac{m_2}{(m_1+m_2)} \cos(\theta_1 - \theta_2) \sin(\theta_1 - \theta_2)}{\left[ 1 - \left( \frac{m_2}{m_1+m_2} \right) \cos^2(\theta_1 - \theta_2) \right]}, \quad (4.39)$$

$$\Lambda_{14} = \frac{\frac{l_2}{l_1} \frac{m_2}{(m_1+m_2)} \sin(\theta_1 - \theta_2)}{\left[ 1 - \left( \frac{m_2}{m_1+m_2} \right) \cos^2(\theta_1 - \theta_2) \right]}. \quad (4.40)$$

Second set of simplified equation can be obtained from (4.35) subtract (4.30) multiple by  $\frac{l_1}{l_2}$  and then divide both sides of equation by its leading coefficient  $1 - \left(\frac{m_2}{m_1+m_2}\right) \cos^2(\theta_1 - \theta_2)$ , yields

$$\ddot{\theta}_2 - (g + \varepsilon\omega^2 \cos \omega t) (\Lambda_{21} \sin \theta_1 + \Lambda_{22} \sin \theta_2) + \Lambda_{23} \dot{\theta}_1^2 + \Lambda_{24} \dot{\theta}_2^2 = 0. \quad (4.41)$$

The coefficients inside (4.41) are

$$\Lambda_{21} = \frac{\frac{1}{l_2}}{\left[1 - \left(\frac{m_2}{m_1+m_2}\right) \cos^2(\theta_1 - \theta_2)\right]}, \quad (4.42)$$

$$\Lambda_{22} = \frac{\frac{1}{l_2} \cos(\theta_1 - \theta_2)}{\left[1 - \left(\frac{m_2}{m_1+m_2}\right) \cos^2(\theta_1 - \theta_2)\right]}, \quad (4.43)$$

$$\Lambda_{23} = \frac{-\frac{l_1}{l_2} \sin(\theta_1 - \theta_2)}{\left[1 - \left(\frac{m_2}{m_1+m_2}\right) \cos^2(\theta_1 - \theta_2)\right]}, \quad (4.44)$$

$$\Lambda_{24} = \frac{-\frac{m_2}{(m_1+m_2)} \cos(\theta_1 - \theta_2) \sin(\theta_1 - \theta_2)}{\left[1 - \left(\frac{m_2}{m_1+m_2}\right) \cos^2(\theta_1 - \theta_2)\right]}. \quad (4.45)$$

Equations (4.36) and (4.41) describe the dynamic of two degree of freedom inverted pendulum under vertical periodic forcing at its base.

## 4.4 Coefficients of 2DOF Inverted Pendulum Equation of Motion

The equation of motion of 2DOF inverted pendulum under periodic vertical forcing is described by (4.36) and (4.41). These two sets of  $2^{nd}$  order nonlinear ordinary differential equations has coupled time-varying coefficients  $\Lambda_{11}, \Lambda_{12}, \Lambda_{21}, \Lambda_{22}$  due to periodic forcing. In addition, there are kinetic energy terms being induced through the interaction of two

pendulums' motion to each other, their coefficients are  $\Lambda_{13}$ ,  $\Lambda_{14}$ ,  $\Lambda_{23}$ , and  $\Lambda_{24}$ . Notice that all coefficients are state-dependent and they all depend on the difference between two pendulum angles  $\theta_1 - \theta_2$ . Due to  $\sin(\theta_1 - \theta_2)$  term in the coefficients of  $\Lambda_{13}$ ,  $\Lambda_{14}$ ,  $\Lambda_{23}$ , and  $\Lambda_{24}$ , their values are always small since the angle  $\theta_1 - \theta_2$  is always small when pendulum is stabilized in its inverted states. We may also notice that all coefficients in the system equation of motion share the same denominator as  $1 - \left(\frac{m_2}{m_1+m_2}\right) \cos^2(\theta_1 - \theta_2)$ . This denominator has value smaller than unity at all conditions which is also state-dependent

$$0 < \frac{m_1}{m_1 + m_2} \leq 1 - \left(\frac{m_2}{m_1 + m_2}\right) \cos^2(\theta_1 - \theta_2) \leq 1. \quad (4.46)$$

Since all parameters has positive values  $m_1, m_2, l_1, l_2 > 0$ , the coefficient  $\Lambda_{11}$  in the first set of equation of motion (4.36) is always larger than  $\Lambda_{12}$  because

$$\frac{1}{l_1} > \frac{1}{l_1} \frac{m_2}{(m_1 + m_2)} \cos(\theta_1 - \theta_2) \quad (4.47)$$

due to the facts that  $\frac{m_2}{(m_1+m_2)} < 1$  and  $-1 < \cos(\theta_1 - \theta_2) < 1$ . The coefficient  $\Lambda_{11}$  always has positive value. From (4.37) and (4.38), we can also get the following relationship:

$$-\frac{m_2}{(m_1 + m_2)} \Lambda_{11} \leq \Lambda_{12} \leq \frac{m_2}{(m_1 + m_2)} \Lambda_{11} \quad (4.48)$$

which shows the limit of  $\Lambda_{12}$  values. Similarly, the coefficient  $\Lambda_{21}$  in the second set of equation of motion (4.41) is always larger than  $\Lambda_{22}$ . From (4.39) and (4.45) we can get the following relationship:

$$\Lambda_{13} = -\Lambda_{24} \quad (4.49)$$

which states that  $\Lambda_{13}$  has the same quantity as  $\Lambda_{24}$  but has reverse sign. Notice that if we set  $m_2 \rightarrow 0$ , then  $\Lambda_{12}, \Lambda_{13}, \Lambda_{14}$  approach zero value which results in the same equation of motion as in single degree of freedom model (2.13). This is the special case of the 2DOF inverted pendulum.

Two degree of freedom pendulum has two distinct modes of vibration when it is stabilized in its inverted state under vertical periodic forcing. Figure 4.2 shows two modes of vibration. The graph on the left shows two pendulums swinging in the same direction where  $\dot{\theta}_1$  and  $\dot{\theta}_2$  have the same sign, we named this kind of vibration as mode 1 type. On the other hand, the graph on the right shows two pendulums swinging in the opposite directions where  $\dot{\theta}_1$  and  $\dot{\theta}_2$  have different signs, we named this kind of vibration as mode 2 type. Although these two types of vibration modes have different pendulum responses they share the same equation of motion sets as in (4.36) and (4.41).

## 4.5 Numerical Integration on Nonlinear 2DOF Inverted Pendulum Model

Introduce new system states as  $x_1 = \theta_1, x_2 = \theta_2, x_3 = \dot{\theta}_1, x_4 = \dot{\theta}_2$  and two additional states  $u = \cos \omega t$  and  $v = \sin \omega t$  that adapt to periodic forcing terms, then nonlinear 2DOF system equation of motion (4.36) and (4.41) becomes

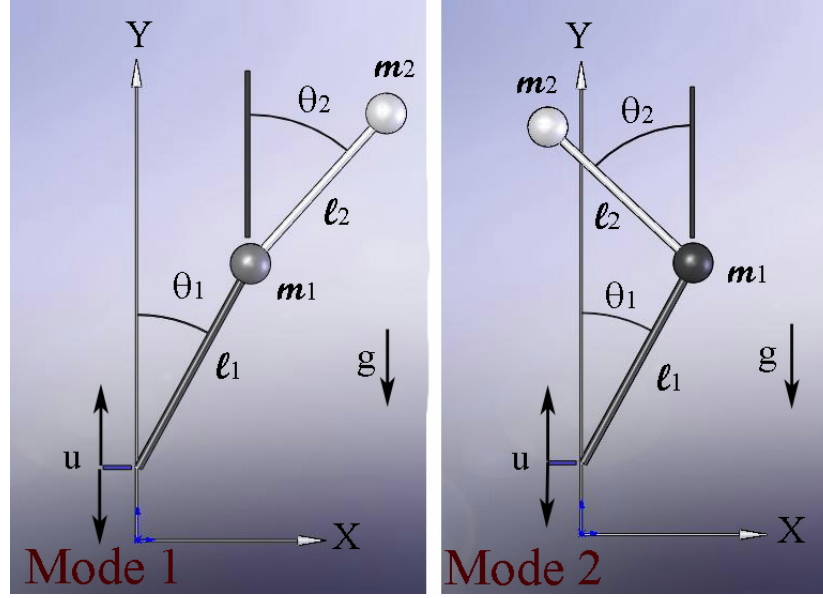


Figure 4.2: Simplified two degree of freedom inverted pendulum model with two point masses mounted on two rigid rods. Two modes of vibration shown on graph: Mode 1(left) and Mode 2(right).

$$\begin{aligned}
 \dot{x}_1 &= x_3, \\
 \dot{x}_2 &= x_4, \\
 \dot{x}_3 &= (g + \varepsilon\omega^2 u) (\Lambda_{11} \sin x_1 + \Lambda_{12} \sin x_2) - (\Lambda_{13}x_3^2 + \Lambda_{14}x_4^2), \\
 \dot{x}_4 &= (g + \varepsilon\omega^2 u) (\Lambda_{21} \sin x_1 + \Lambda_{22} \sin x_2) - (\Lambda_{23}x_3^2 + \Lambda_{24}x_4^2), \\
 \dot{u} &= u(1 - u^2 - v^2) - \omega v, \\
 \dot{v} &= v(1 - u^2 - v^2) + \omega u.
 \end{aligned} \tag{4.50}$$

All coefficients inside (4.50) are the same definitions as in equations from (4.37) to (4.45).

We may apply numerical integration technique through parameter continuation code using 4<sup>th</sup> order Runge-Kutta scheme to (4.50). Two simulation results are shown in Figure 4.3

and Figure 4.4. Both simulation results were obtained from applying the same system parameters:  $m_1 = 0.0038, m_2 = 0.0019, l_1 = 0.0537, l_2 = 0.0251$ . Figure 4.3 shows that system is under mode 1 vibration where the first pendulum is swinging at the same direction as the second pendulum. Figure 4.4 shows that system is under mode 2 vibration where the first pendulum is swinging at opposite directions compare to the second pendulum. Both simulation results came from the same vertical periodic forcing to the pendulum base which has periodic forcing amplitude  $\varepsilon = 0.00593$  and forcing frequency  $\omega = 250$  rad/s. The only difference in getting these two distinct responses from the same equation of motion sets are applying different initial conditions to (4.50). Mode 1 response or Figure 4.3 has initial conditions  $\theta_{10} = 0.05, \dot{\theta}_{10} = 0$  and  $\theta_{20} = 0.1, \dot{\theta}_{20} = 0$ ; Mode 2 response or Figure 4.4 has initial conditions  $\theta_{10} = 0.1, \dot{\theta}_{10} = 0$  and  $\theta_{20} = -0.101, \dot{\theta}_{20} = 0$ .

As shown in Figure 4.3, the inverted pendulum has bounded response. It's time trace represents near periodic behavior and the first pendulum swings at the same direction as the second pendulum which indicated mode 1 vibration. Both of its phase portraits show bounded orbits which we may conclude as quasiperiodic behavior. Unlike single degree of freedom inverted pendulum case whose phase portrait has zero nullclines in both vertical and horizontal directions, the 2DOF inverted pendulum has non-zero vertical nullcline if it starts from non-zero initial conditions. The starting vertical nullcline location in  $\theta_1 - \dot{\theta}_1$  plane depends on the initial condition of the second pendulum while the starting vertical nullcline location in  $\theta_2 - \dot{\theta}_2$  plane depends on the initial conditions of the first pendulum. In fact, those vertical nullclines obtained from the nonlinear model were not perfectly straight, their curvatures depended on the coefficients  $\Lambda_{13}, \Lambda_{14}, \Lambda_{23}, \Lambda_{24}$ . The 3D phase portrait in

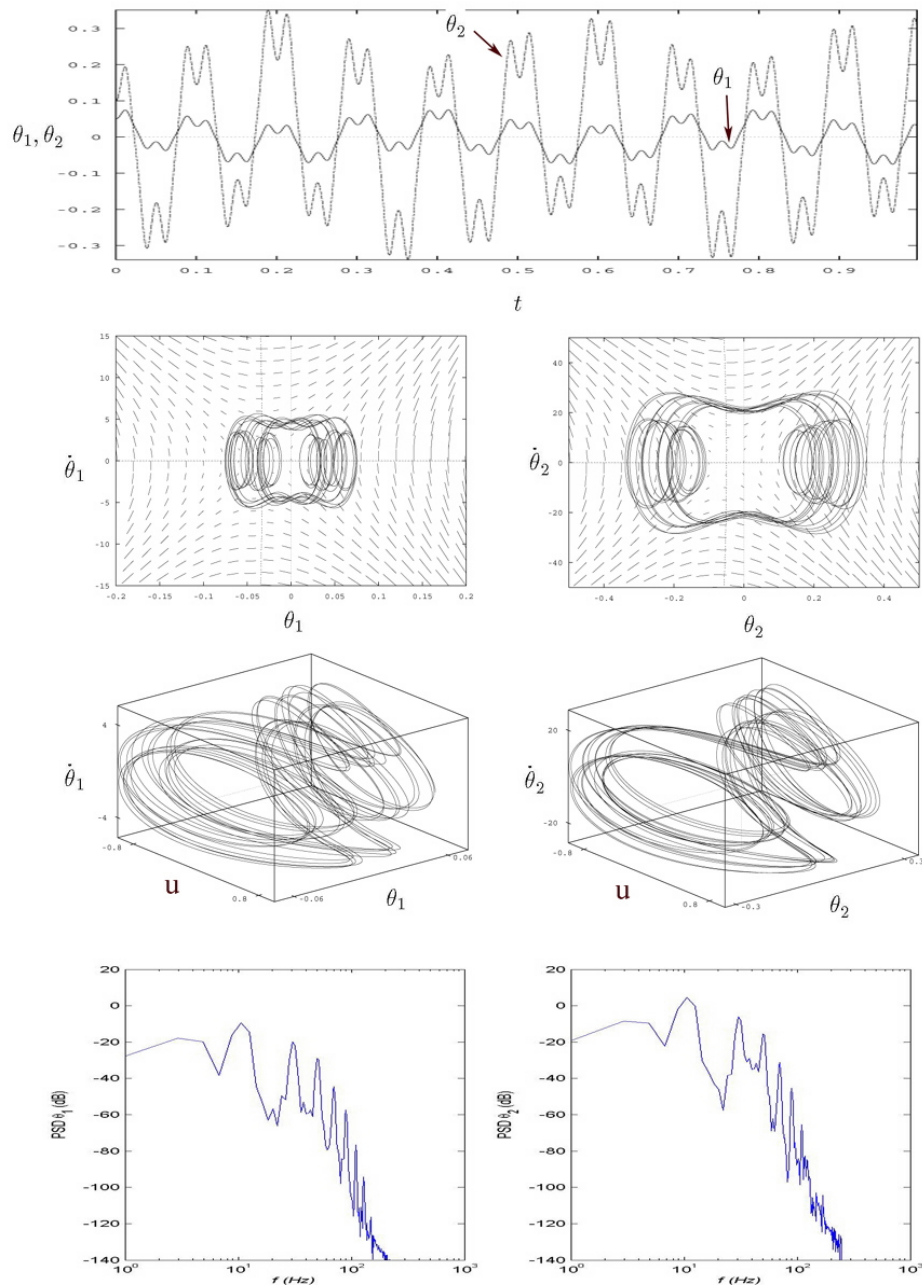


Figure 4.3: 2DOF inverted pendulum under mode 1 vibration with vertical periodic forcing amplitude  $\varepsilon = 0.00593$  and forcing frequency  $\omega = 250$  rad/s. Initial conditions are  $\theta_{1_0} = 0.05, \dot{\theta}_{1_0} = 0$  and  $\theta_{2_0} = 0.1, \dot{\theta}_{2_0} = 0$ .

Figure 4.3 shown that their orbits were close to 4 : 1 periodic ratio. The power spectral density graph shown that the system response had already past period-doubling bifurcation, there were multiple harmonic components higher than the forcing frequency which was  $\omega = 250 \text{ rad/s} \approx 39.8 \text{ Hz}$ . Compare to Figure 4.3, when applying different initial conditions to the same 2DOF inverted pendulum model with the same forcing as in (4.50) we can get totally different pendulum response as in Figure 4.4 which indicates the 2DOF inverted pendulum is now under mode 2 vibration. In Figure 4.4 the pendulum response can only be concluded as bounded, the periodic effect is not obvious. It's time trace shown the first pendulum swings at different directions compare with the second pendulum which indicated mode 2 vibration. Both of its phase portraits and its  $3D$  phase portrait shown bounded behavior. Notice that although two power spectral density graphs in Figure 4.3 and Figure 4.4 showed similar patterns. However, in Figure 4.3 it showed the dominated harmonic component located at around 10 Hz; while in Figure 4.4 the dominated harmonic component had been shifted to lower frequency at around 2 Hz.

None of our simulation results shown clear periodic behavior in 2DOF inverted pendulum using full nonlinear model as described in (4.50). This can be explained as the induced kinetic terms affected the steadiness of their phase portrait orbits and caused them to fluctuate regardless that their coefficients  $\Lambda_{13}, \Lambda_{14}, \Lambda_{23}, \Lambda_{24}$  are always small.

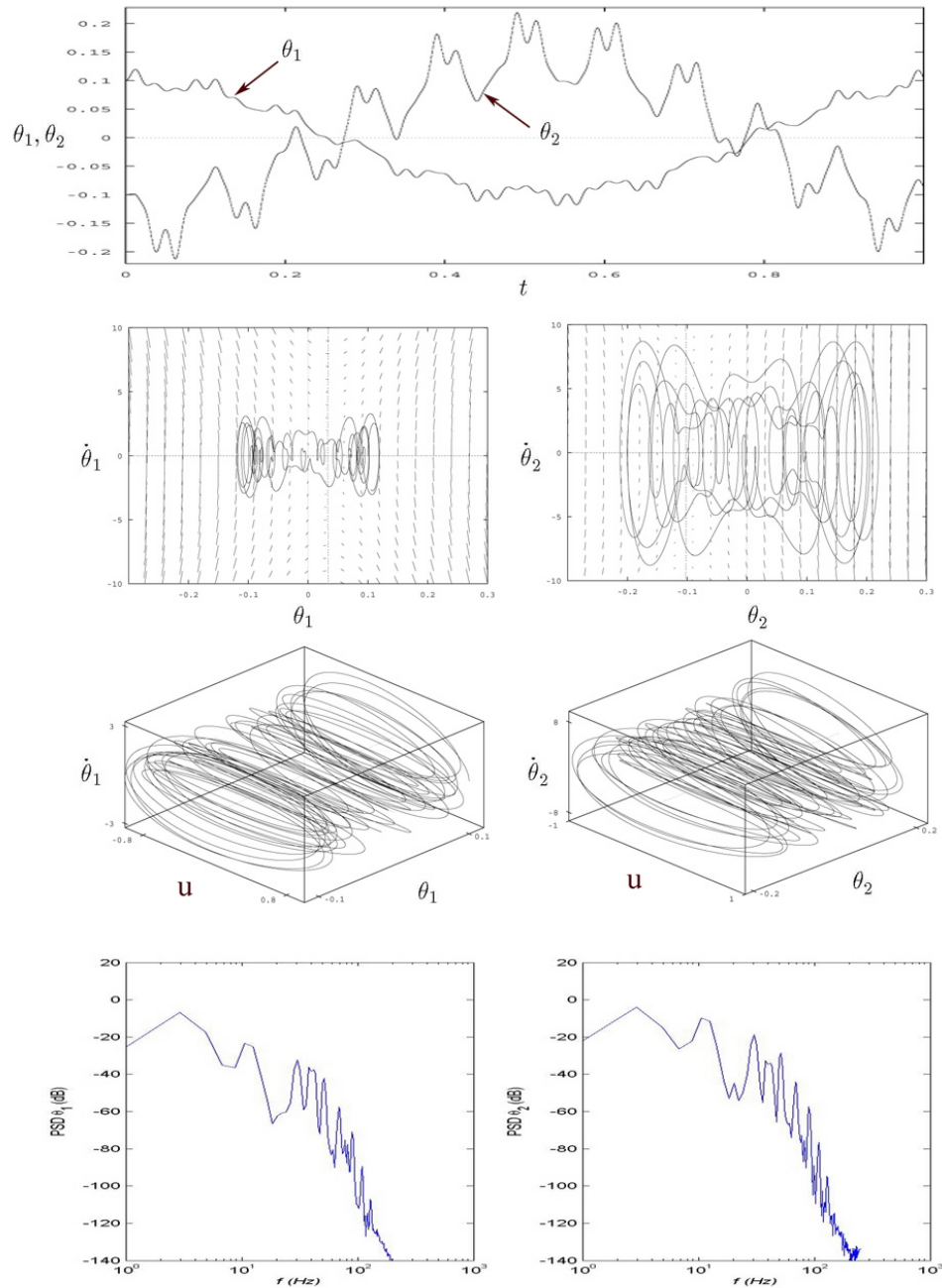


Figure 4.4: When applying different initial conditions to the same 2DOF inverted pendulum model we can get mode 2 vibration with the same vertical periodic forcing amplitude  $\varepsilon = 0.00593$  and forcing frequency  $\omega = 250$  rad/s. Initial conditions are  $\theta_{1_0} = 0.1, \dot{\theta}_{1_0} = 0$  and  $\theta_{2_0} = -0.101, \dot{\theta}_{2_0} = 0$ .

## 4.6 Small Angle Assumption to Obtain Linear 2DOF Inverted Pendulum Model

To obtain clear periodic orbits in a 2DOF case, we may linearize its nonlinear model by applying small angle assumptions to pendulum angles. Under the condition of small  $\theta_1$  and  $\theta_2$  angles as  $\theta_1 \rightarrow 0$  and  $\theta_2 \rightarrow 0$ , we may get the following approximations:

$$\begin{aligned}
 \sin \theta_1 &\rightarrow \theta_1, \\
 \sin \theta_2 &\rightarrow \theta_2, \\
 \cos \theta_1 &\rightarrow 1, \\
 \cos \theta_2 &\rightarrow 1,
 \end{aligned} \tag{4.51}$$

and

$$\begin{aligned}
 \sin (\theta_1 - \theta_2) &\rightarrow (\theta_1 - \theta_2), \\
 \cos (\theta_1 - \theta_2) &\rightarrow 1, \\
 \cos^2 (\theta_1 - \theta_2) &\rightarrow 1.
 \end{aligned} \tag{4.52}$$

Therefore, we may obtain the simplified system equation of motion as

$$\ddot{\theta}_1 - (g + \varepsilon\omega^2 \cos \omega t) (\Lambda_{11}\theta_1 + \Lambda_{12}\theta_2) + \Lambda_{13}\dot{\theta}_1^2 + \Lambda_{14}\dot{\theta}_2^2 = 0, \tag{4.53}$$

$$\ddot{\theta}_2 - (g + \varepsilon\omega^2 \cos \omega t) (\Lambda_{21}\theta_1 + \Lambda_{22}\theta_2) + \Lambda_{23}\dot{\theta}_1^2 + \Lambda_{24}\dot{\theta}_2^2 = 0. \tag{4.54}$$

where the new coefficients can be simplified as

$$\Lambda_{11} \rightarrow \frac{m_1 + m_2}{m_1 l_1}, \quad (4.55)$$

$$\Lambda_{12} \rightarrow \frac{m_2}{m_1 l_1}, \quad (4.56)$$

$$\Lambda_{13} \rightarrow \frac{m_2}{m_1} (\theta_1 - \theta_2), \quad (4.57)$$

$$\Lambda_{14} \rightarrow \frac{m_2 l_2}{m_1 l_1} (\theta_1 - \theta_2), \quad (4.58)$$

and

$$\Lambda_{21} \rightarrow \frac{m_1 + m_2}{m_1 l_2}, \quad (4.59)$$

$$\Lambda_{22} \rightarrow \frac{m_1 + m_2}{m_1 l_2}, \quad (4.60)$$

$$\Lambda_{23} \rightarrow -\frac{(m_1 + m_2) l_1}{m_1 l_2} (\theta_1 - \theta_2), \quad (4.61)$$

$$\Lambda_{24} \rightarrow -\frac{m_2}{m_1} (\theta_1 - \theta_2). \quad (4.62)$$

Since  $\theta_1$  and  $\theta_2$  are both small, the coefficients  $\Lambda_{13}, \Lambda_{14}, \Lambda_{23}, \Lambda_{24}$  are also small.

We may then neglect those induced kinetic terms due to  $\Lambda_{13}, \Lambda_{14}, \Lambda_{23}, \Lambda_{24} \rightarrow 0$  to obtain

linear system equation of motion as:

$$\ddot{\theta}_1 - (g + \varepsilon \omega^2 \cos \omega t) (\Lambda_{11} \theta_1 + \Lambda_{12} \theta_2) = 0 \quad (4.63)$$

$$\ddot{\theta}_2 - (g + \varepsilon \omega^2 \cos \omega t) (\Lambda_{21} \theta_1 + \Lambda_{22} \theta_2) = 0 \quad (4.64)$$

with new system coefficients

$$\Lambda_{11} = \frac{m_1 + m_2}{m_1 l_1}, \quad (4.65)$$

$$\Lambda_{12} = \frac{m_2}{m_1 l_1}, \quad (4.66)$$

$$\Lambda_{21} = \frac{m_1 + m_2}{m_1 l_2}, \quad (4.67)$$

$$\Lambda_{22} = \frac{m_1 + m_2}{m_1 l_2}. \quad (4.68)$$

Apply change of variables of  $x_1 = \theta_1$ ,  $x_2 = \theta_2$ ,  $x_3 = \dot{\theta}_1$ ,  $x_4 = \dot{\theta}_2$ , the linear system equation of motion can be described in matrix form as

$$\begin{bmatrix} \dot{x}_1 \\ \dot{x}_2 \\ \dot{x}_3 \\ \dot{x}_4 \end{bmatrix} = \begin{bmatrix} 0 & 0 & 1 & 0 \\ 0 & 0 & 0 & 1 \\ \Delta(t)\Lambda_{11} & \Delta(t)\Lambda_{12} & 0 & 0 \\ \Delta(t)\Lambda_{21} & \Delta(t)\Lambda_{22} & 0 & 0 \end{bmatrix} \begin{bmatrix} x_1 \\ x_2 \\ x_3 \\ x_4 \end{bmatrix}. \quad (4.69)$$

Equation (4.69) takes the form  $\dot{X} = A(t)X$  which is a first order ordinary differential equation with time-periodic coefficient. The time-periodic property is coming from the vertical periodic forcing  $\ddot{h}(t) = \varepsilon\omega^2 \cos \omega t$  which is included inside  $\Delta(t)$  as  $\Delta(t) = g + \varepsilon\omega^2 \cos \omega t$ . Equation (4.69) is similar to (2.50) which indicates that Floquet theory and Hill's equation can be applied to check the stability of this 2DOF linear time-periodic system. It is possible to obtain clear periodic orbits from simulating the linear 2DOF inverted pendulum model in (4.69) since one of the effect of causing fluctuations in nonlinear model has been removed from making the coefficients of  $\dot{\theta}_1^2$  and  $\dot{\theta}_2^2$  equal to zero.

Since there are two modes of vibration in the 2DOF inverted pendulum response, we may apply the same technique as in solving the nonlinear model (4.50) numerically which requires to assign two different types of initial conditions: assign  $\theta_{1_0}$  and  $\theta_{2_0}$  the same sign

and  $\dot{\theta}_{1_0} = \dot{\theta}_{2_0} = 0$  to get mode 1 vibration; assign  $\theta_{2_0}$  reverse sign to  $\theta_{1_0}$  and  $\dot{\theta}_{1_0} = \dot{\theta}_{2_0} = 0$  to get mode 2 vibration. Notice that in mode 2 case when we reverse sign of two initial angles, it also requires that coefficients  $\Lambda_{21}, \Lambda_{22}$  in second set of equation of motion (4.64) reverse their signs as shown in (4.70) and (4.71).

$$\Lambda_{21} = -\frac{m_1 + m_2}{m_1 l_2}, \quad (4.70)$$

$$\Lambda_{22} = -\frac{m_1 + m_2}{m_1 l_2}. \quad (4.71)$$

Our goal in numerical simulation on 2DOF linear inverted pendulum model is to characterize the type of periodic solutions similarly to the single degree of freedom case presented in earlier chapter of this paper. We applied the same parameter continuation simulation code as being used in sDOF case by integrating the ordinary differential equations numerically through 4<sup>th</sup> order Runge-Kutta scheme. The simulation results of two modes of vibration on 2DOF linear inverted pendulum under periodic forcing is presented in the following sections. Similar to sDOF case, four different kinds of geometric realization of system response are being used to present our data: system time traces, system phase portrait, three dimensional view of system phase portrait compare to input forcing, and system's power spectral density diagram.

## **Simulation Results on Linear 2DOF Inverted Pendulum Model under Mode 1 Vibration**

Since our goal in numerical simulation is to characterize different types of periodic solutions due to different periodic forcing, we applied a set of generic coefficients as  $\Lambda_{11} =$

1.5,  $\Lambda_{12} = 0.6$ ,  $\Lambda_{21} = 0.6$ ,  $\Lambda_{22} = 0.6$  to our 2DOF linear model as described in (4.63) and (4.64). All simulations were under the same initial conditions as  $\theta_{1_0} = 0.1$ ,  $\dot{\theta}_{1_0} = 0$  and  $\theta_{2_0} = 0.3$ ,  $\dot{\theta}_{2_0} = 0$ . Two periodic solution results are shown in Figure 4.5 and Figure 4.6. The system responses indicate that both system were under mode 1 vibration. We used the same four geometric representations: time trace, phase portrait, 3D phase portrait, and power spectral density graph, to present our simulation results. The left hand side graph set indicates the first degree of freedom pendulum's response while right hand side graph set indicates the second degree of freedom pendulum's response. In Figure 4.5, with periodic input forcing amplitude  $\varepsilon = 0.2138$  and forcing frequency  $\omega = 200$  it shows that pendulum was under 4 : 1 frequency ratio. It's phase portraits represent symmetric periodic orbits with their vertical nullclines located in non-zero positions. The power spectral density graph extracts multiple peaks in various frequencies locations and the largest peak happened in the lowest frequency at around 10 Hz.

In Figure 4.6, with periodic input forcing amplitude  $\varepsilon = 0.03025$  and forcing frequency  $\omega = 200$  it shows that pendulum was under 35 : 1 frequency ratio. It's phase portraits have asymmetric periodic orbits and their vertical nullclines located in non-zero positions. The power spectral density graph extracts 3 clear peaks with the dominated harmonic component located below 1 Hz denotes as system slow time and second peak corresponding to the periodic forcing around 32 Hz denotes as system fast time. The third peak has frequency about twice as large as the second peak which located within the range of 60 Hz  $\sim$  70 Hz.

Compare with periodic response as shown in Figure 4.6, under slightly different

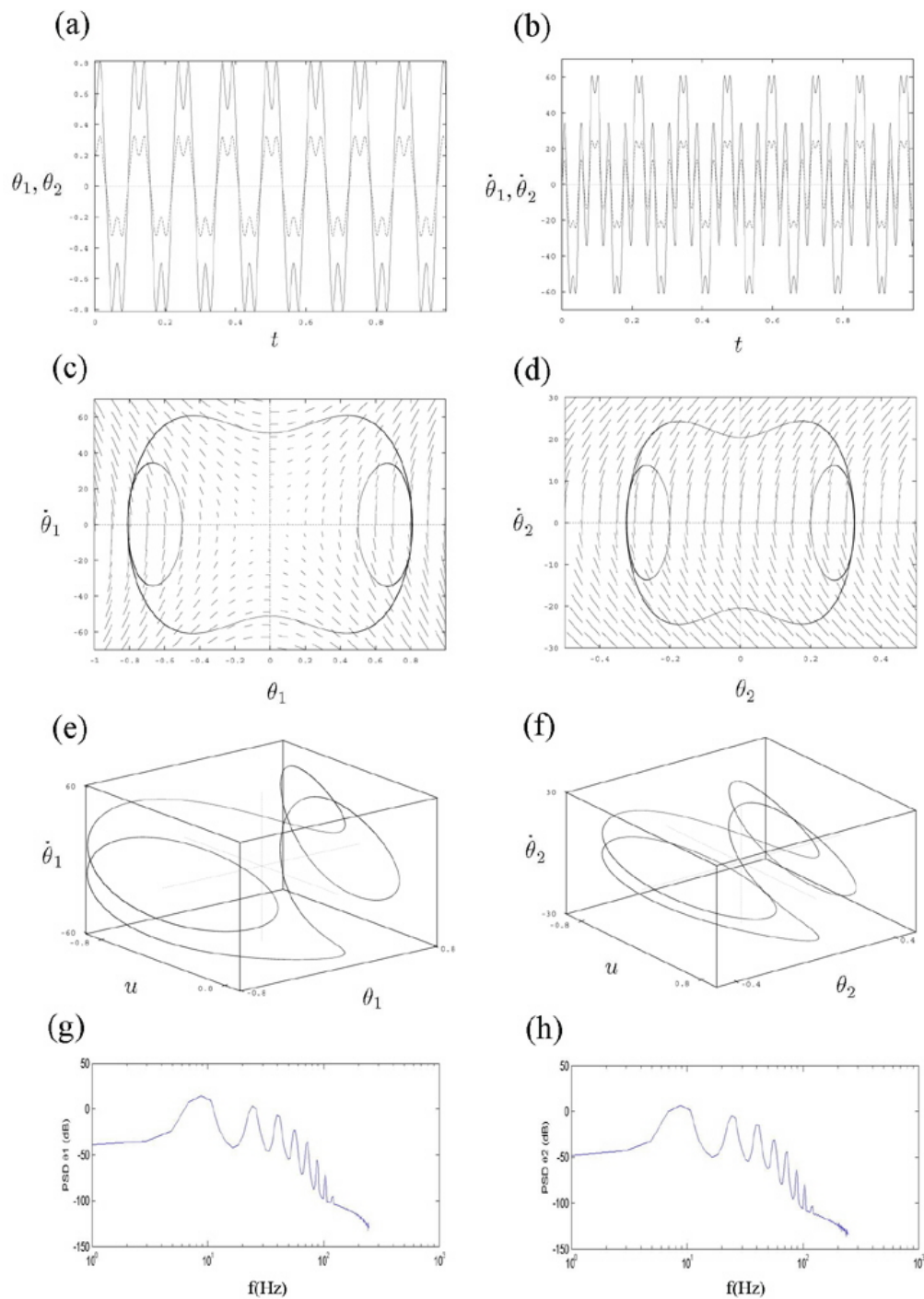


Figure 4.5: 2DOF inverted pendulum under mode 1 vibration. The periodic input forcing amplitude was  $\varepsilon = 0.2138$  and the forcing frequency was  $\omega = 200$ .

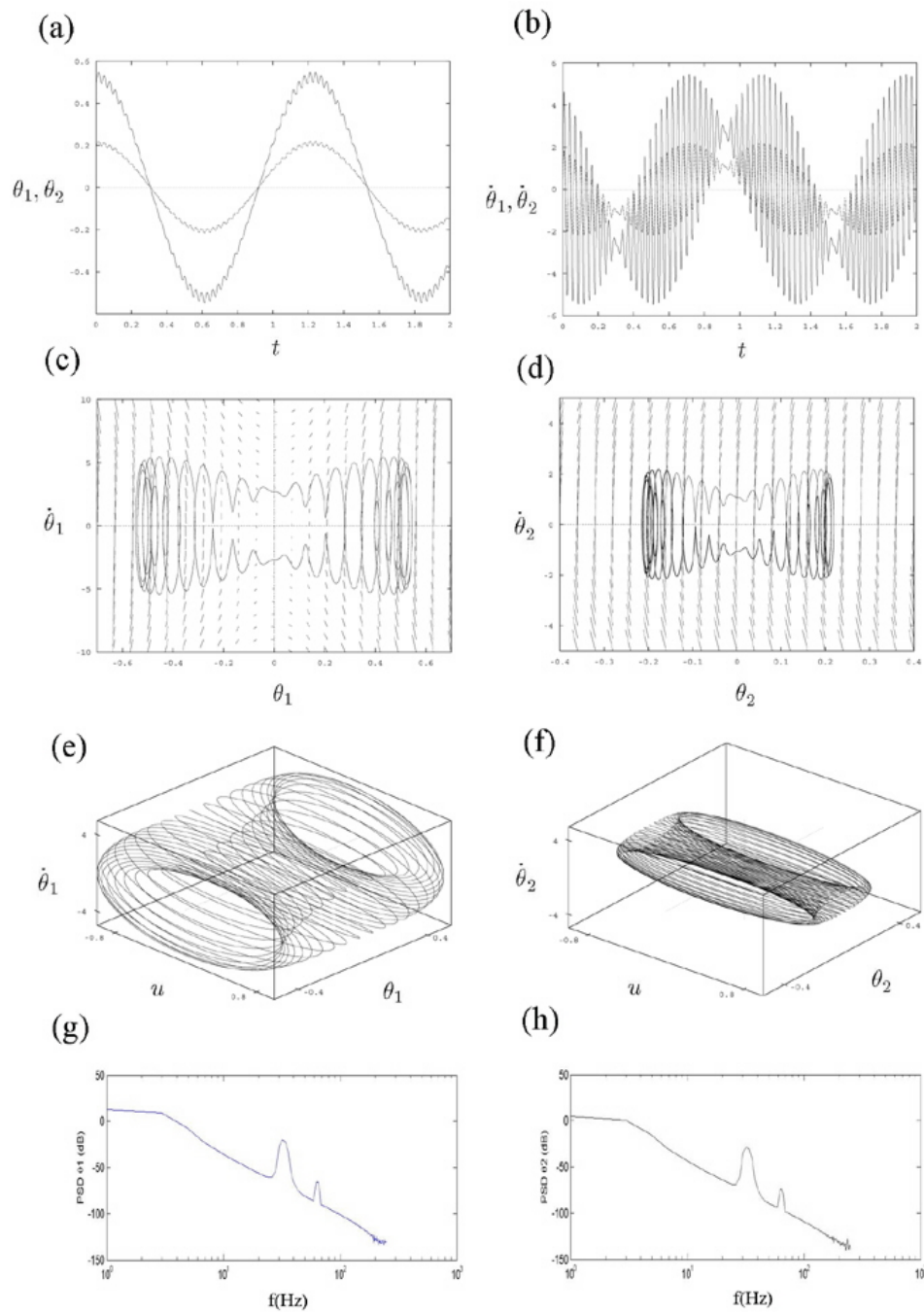


Figure 4.6: 2DOF inverted pendulum under mode 1 vibration. The periodic input forcing amplitude was  $\varepsilon = 0.03025$  and the forcing frequency was  $\omega = 200$ .

periodic input forcing amplitude  $\varepsilon = 0.03023$ , the pendulum's response doesn't repeat itself exactly as in previous periodic case. Instead, the system showed quasiperiodic behavior as in Figure 4.7. In part (a) of Figure 4.7, we presented time trace to a longer period of 10 seconds in order to see long term signal drift. It's phase portraits show that the system response still remain bounded but the orbits in the phase portrait occupy more area inside. Their 3D phase portraits also occupy more area in the graph. The power spectral density graph is almost identical to the previous case as shown in Figure 4.6 which extracts 3 clear peaks with the dominated low frequency harmonic component located below 1 Hz denotes as system slow time and second peak corresponding to the periodic forcing around 32 Hz denotes as system fast time. The third peak has frequency about twice as large as the second peak which located within the range of 60 Hz  $\sim$  70 Hz.

## **Simulation Results on Linear 2DOF Inverted Pendulum Model under Mode 2 Vibration**

Similar to the simulation results on linear 2DOF inverted pendulum model under mode 1 vibration, we applied a set of generic coefficients to simulate mode 2 vibration as  $\Lambda_{11} = 1.5, \Lambda_{12} = 0.6, \Lambda_{21} = -0.6, \Lambda_{22} = -0.6$  to our 2DOF linear model as described in (4.63) and (4.64). All simulations were under the same initial conditions as  $\theta_{1_0} = 0.1, \dot{\theta}_{1_0} = 0$  and  $\theta_{2_0} = -0.05, \dot{\theta}_{2_0} = 0$ . Four periodic solution results are shown in Figure 4.8 , Figure 4.9, Figure 4.9, and Figure 4.11. The system responses indicate that they were under mode 2 vibration. We used the same four geometric representations: time trace, phase portrait, 3D phase portrait, and power spectral density graph, to present our simulation results. The left hand side graph set indicates the first degree of freedom pendulum's response while

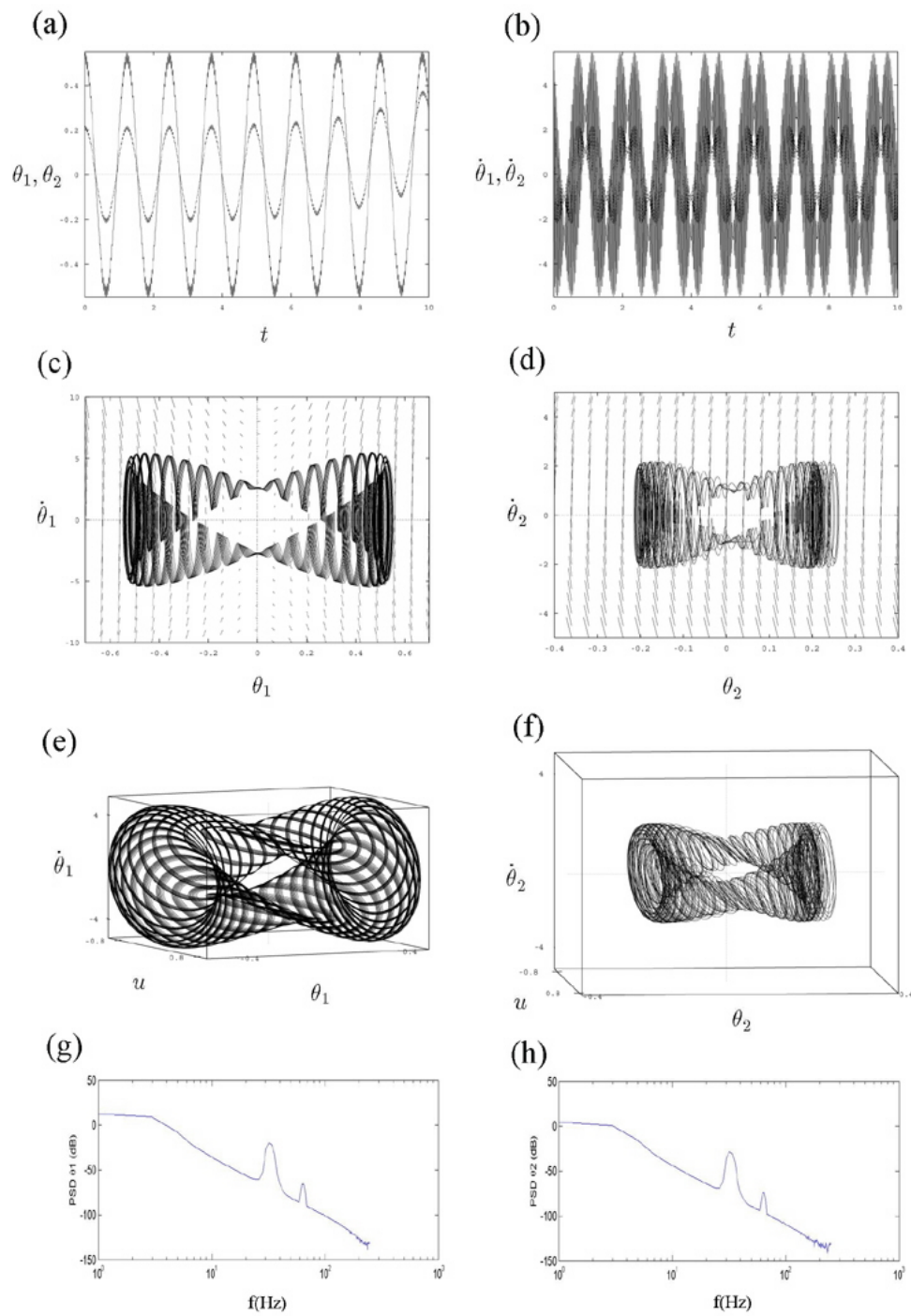


Figure 4.7: 2DOF inverted pendulum under mode 1 vibration. The periodic input forcing amplitude was  $\varepsilon = 0.03023$  and the forcing frequency was  $\omega = 200$ . The inverted pendulum shows quasiperiodic response.

right hand side graph set indicates the second degree of freedom pendulum's response. In Figure 4.8, with periodic input forcing amplitude  $\varepsilon = 0.2138$  and forcing frequency  $\omega = 200$  it shows that pendulum was under 4 : 1 frequency ratio. This is the same result as shown in mode 1 case as in Figure 4.5. It's phase portraits represent symmetric periodic orbits with their vertical nullclines located in non-zero positions. Notice that the second degree of freedom phase portrait has its non-zero nullcline moved to the opposite location compare to mode 1 case as in Figure 4.5. The power spectral density graph extracts multiple peaks in various frequencies locations and the largest peak happened in the lowest frequency at around 10 Hz.

In Figure 4.9, with periodic input forcing amplitude  $\varepsilon = 0.1514$  and forcing frequency  $\omega = 200$  it shows that pendulum was under 6 : 1 frequency ratio. It's phase portraits have symmetric periodic orbits and their vertical nullclines located in non-zero positions. The power spectral density graph extracts multiple peaks with the dominated low frequency harmonic component located around 6 Hz denotes as system slow time.

In Figure 4.10, with periodic input forcing amplitude  $\varepsilon = 0.11637$  and forcing frequency  $\omega = 200$  it shows that pendulum was under 8 : 1 frequency ratio. It's phase portraits have symmetric periodic orbits and their vertical nullclines located in non-zero positions. The power spectral density graph extracts multiple peaks similar to 6 : 1 case with the dominated low frequency harmonic component moved to even lower frequency around 4 Hz denotes as system slow time.

In Figure 4.11, with periodic input forcing amplitude  $\varepsilon = 0.05037$  and forcing frequency  $\omega = 200$  it shows that pendulum was under 18 : 1 frequency ratio. It's phase

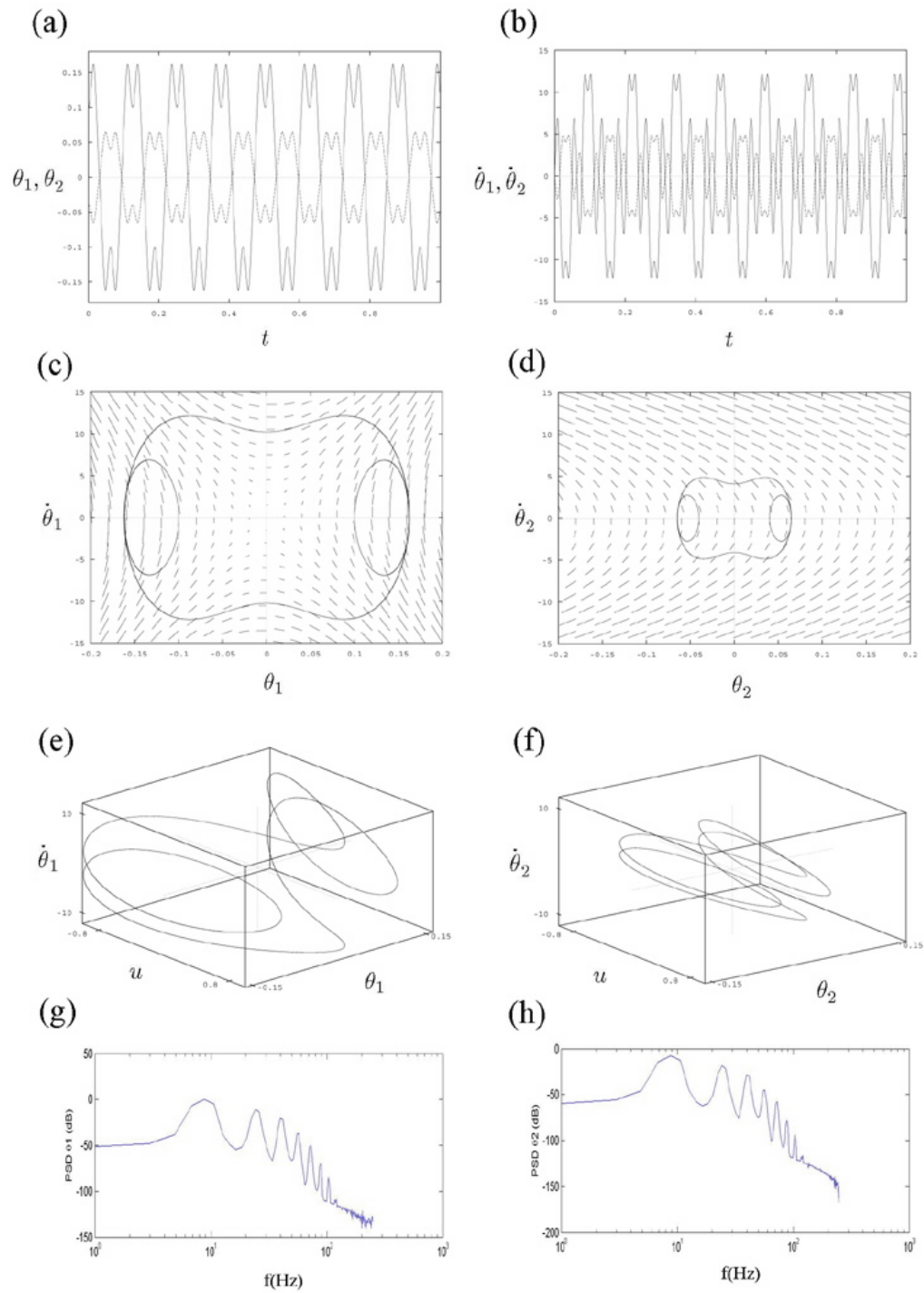


Figure 4.8: 2DOF inverted pendulum under mode 2 vibration. The periodic input forcing amplitude was  $\varepsilon = 0.2138$  and the forcing frequency was  $\omega = 200$ .

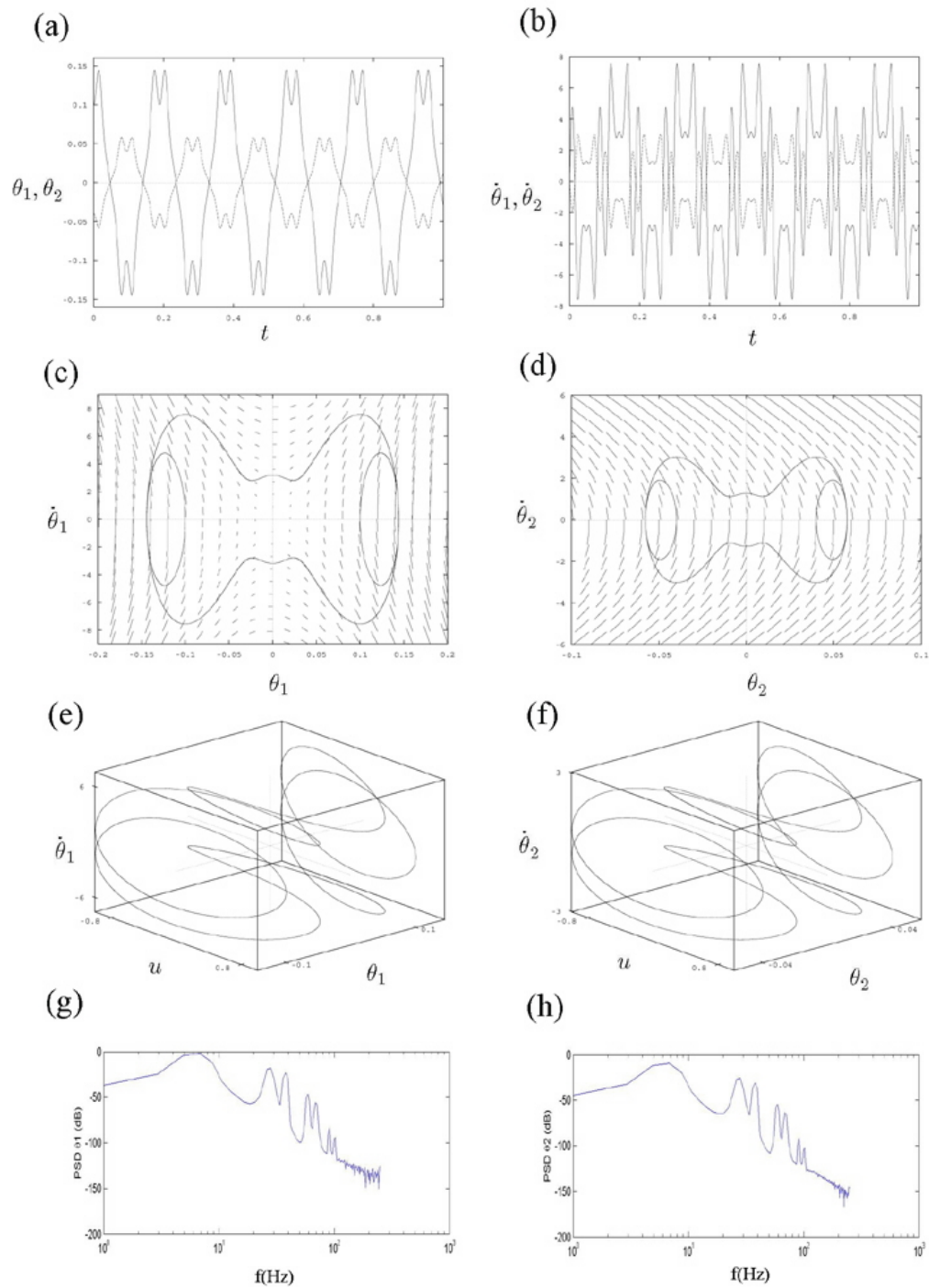


Figure 4.9: 2DOF inverted pendulum under mode 2 vibration. The periodic input forcing amplitude was  $\varepsilon = 0.1514$  and the forcing frequency was  $\omega = 200$ .

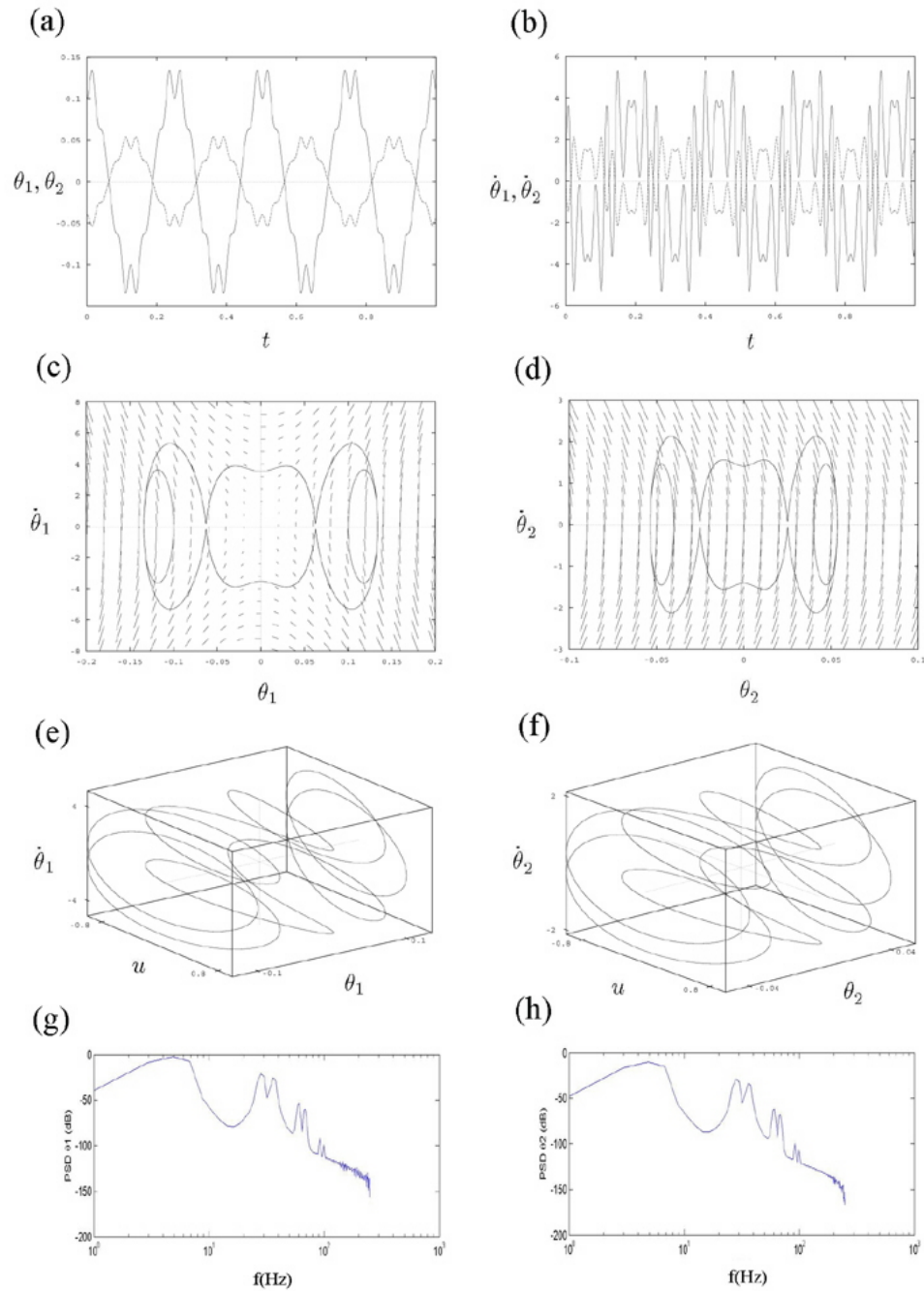


Figure 4.10: 2DOF inverted pendulum under mode 2 vibration. The periodic input forcing amplitude was  $\varepsilon = 0.11637$  and the forcing frequency was  $\omega = 200$ .

portraits have symmetric periodic orbits and their vertical nullclines located in non-zero positions. The power spectral density graph extracts 3 clear peaks with the dominated low frequency harmonic component moved to even lower frequency around 1.5 Hz denotes as system slow time. The second peaks located at around 32 Hz corresponding to periodic forcing frequency and the system fast time. The third peak has frequency about twice as large as the second peak which located within the range of 60 Hz  $\sim$  70 Hz.

Compare with periodic response as shown in Figure 4.11, under slightly different periodic input forcing amplitude  $\varepsilon = 0.0500$ , the pendulum's response doesn't repeat itself exactly as in previous periodic case. Instead, the system showed quasiperiodic behavior as in Figure 4.12. In part (a) of Figure 4.12, we presented time trace to a longer period of 10 seconds in order to see long term signal drift. It's phase portraits show that the system response still remain bounded but the orbits in the phase portrait occupy more area inside. Their 3D phase portraits also occupy more area in the graph. The power spectral density graph is almost identical to the previous case as shown in Figure 4.11 which extracts 3 clear peaks with the dominated low frequency harmonic component located around 1.5 Hz denotes as system slow time and second peak corresponding to the periodic forcing around 32 Hz denotes as system fast time. The third peak has frequency about twice as large as the second peak which located within the range of 60 Hz  $\sim$  70 Hz.

Compare with periodic response as shown in Figure 4.8, under different periodic input forcing amplitude  $\varepsilon = 0.2600$ , the pendulum's response still performed near periodic behavior as in Figure 4.13. In order to see long term signal drift we presented time trace to a longer period of 20 seconds as shown in part (a) of Figure 4.13. It's phase portraits

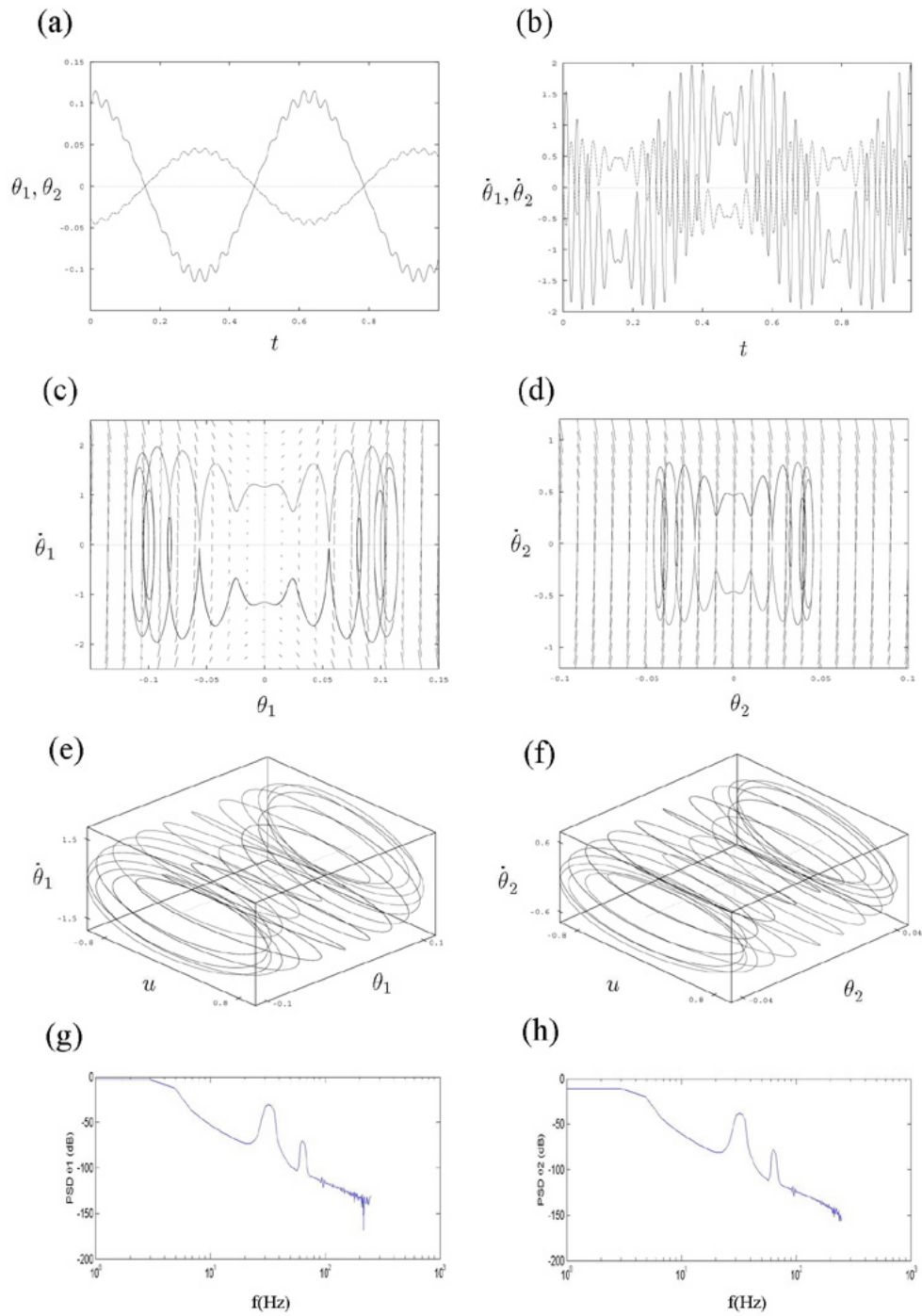


Figure 4.11: 2DOF inverted pendulum under mode 2 vibration. The periodic input forcing amplitude was  $\varepsilon = 0.05037$  and the forcing frequency was  $\omega = 200$ .

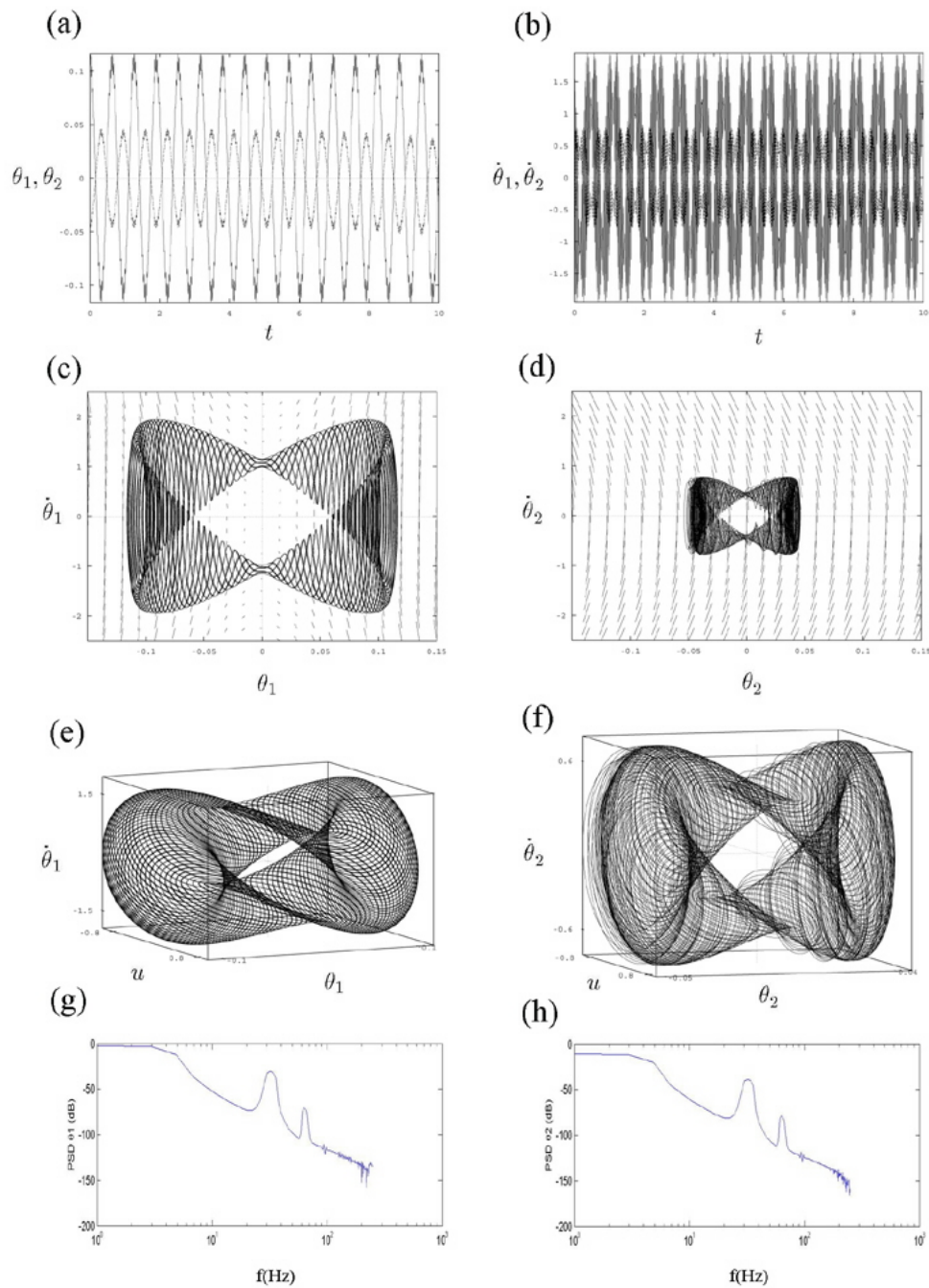


Figure 4.12: 2DOF inverted pendulum under mode 2 vibration. The periodic input forcing amplitude was  $\varepsilon = 0.05$  and the forcing frequency was  $\omega = 200$ . The inverted pendulum shows quasiperiodic response.

showed wider periodic orbits in 4 : 1 frequency ratio as in part (c),(d) of Figure 4.13 and the phase portrait orbits were symmetric with non-zero vertical nullclines. The power spectral density graphs are almost identical to the previous case as shown in Figure 4.8 which extract multiple peaks in various frequencies locations and the largest peak happened in the lowest frequency at around 10 Hz.

### **Numerical simulation result comparison**

From analyzing the response of linear 2DOF inverted pendulum model we found two modes of vibration from different initial conditions. However, in searching for periodic solutions inside the stable region around pendulum's inverted state, our simulation results showed similar patterns from comparing these two modes. Therefore we choose only one mode of simulation results in presenting graph comparison from different forcing amplitude while keeping forcing frequency fixed. Figure 4.14 presents the periodic solutions of system phase portrait comparison of the same 2DOF linear model under increasing forcing amplitudes. Notice that in Figure 4.14 we applied the same periodic forcing frequency  $\omega = 200$  rad/s which is equivalent to about 32 Hz throughout. From upper left to lower right of Figure 4.14, we applied ascending input periodic forcing amplitudes from  $\varepsilon = 0.04015$  to  $\varepsilon = 0.259$ . Their phase portraits show different periodic orbits and their frequency ratios have descending orders from increasing  $\varepsilon$ . Notice that we don't list all of the periodic solutions, only 9 graphs being chosen that we can display them in a systematic way. The lowest frequency ratio that we got from simulation results is 4 : 1.

Corresponding to the phase portrait comparison graphs as in Figure 4.14, in Figure 4.15 we show their power spectral density graphs in relative graph locations according to

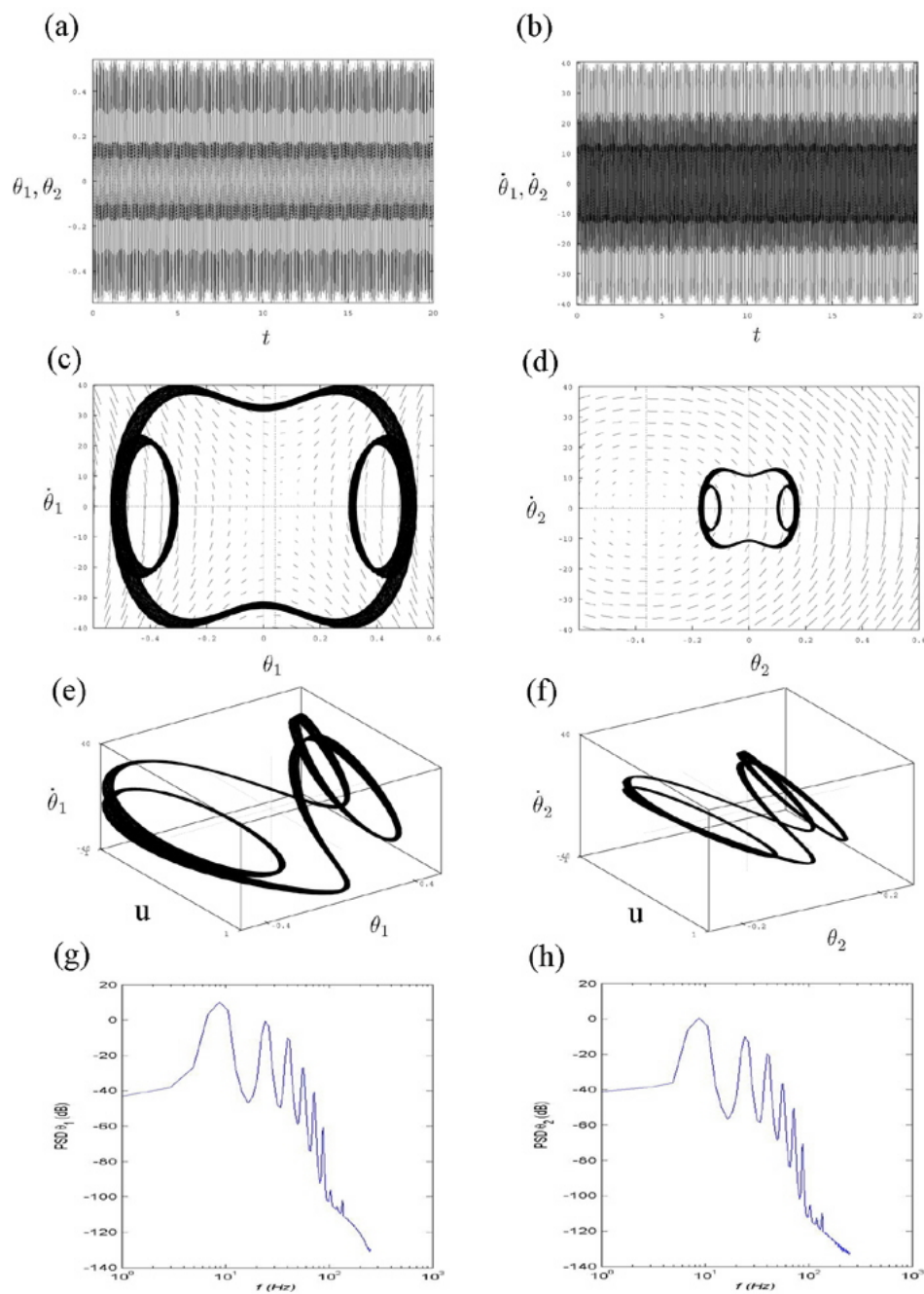


Figure 4.13: 2DOF inverted pendulum under mode 2 vibration. The periodic input forcing amplitude was  $\varepsilon = 0.26$  and the forcing frequency was  $\omega = 200$ . The inverted pendulum shows near periodic response.

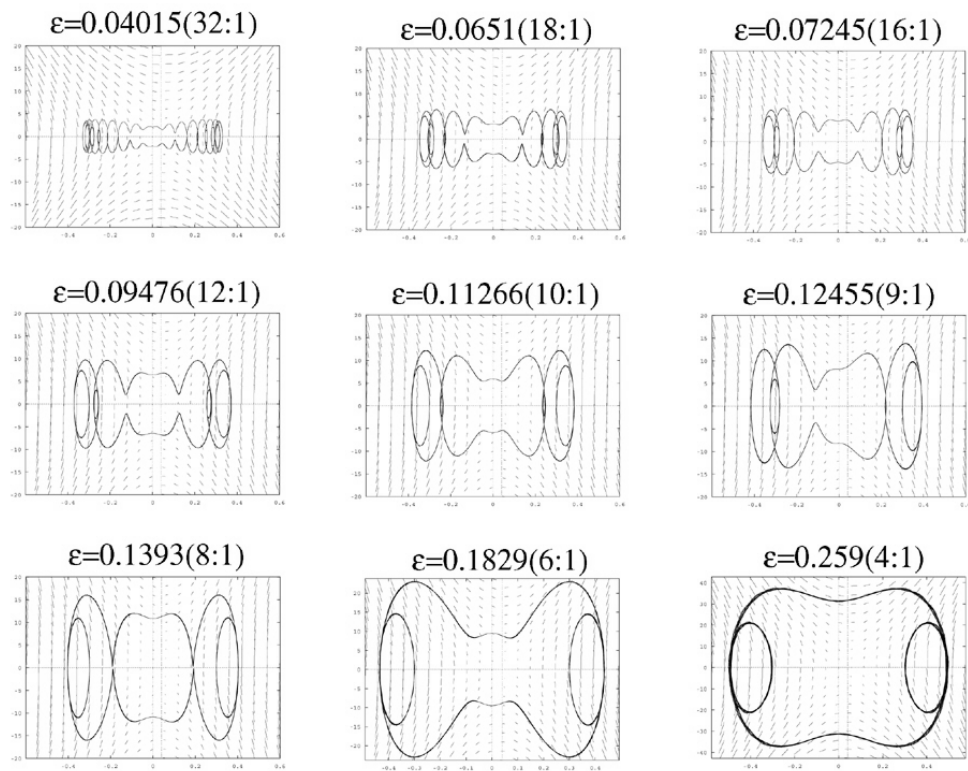


Figure 4.14: Phase portrait comparison of periodic solutions on numerical simulation using linear 2DOF inverted pendulum model. From upper left to lower right, the forcing amplitude has ascending values which result in descending frequency ratio.

the same ascending order of periodic forcing amplitudes from  $\varepsilon = 0.04015$  to  $\varepsilon = 0.259$ . From upper left graph of Figure 4.15, the system is under low periodic forcing amplitude at  $\varepsilon = 0.04015$  and its power spectral density graph shows 3 clear peaks. The largest peak happened at the lowest frequency location around 3 Hz which is referred as slow time of the system. The second peak has frequency around 30 Hz which follows the periodic forcing frequency which is also referred as fast time of system. The third peak has about double frequency compare to the second one. As we increased the periodic forcing amplitude  $\varepsilon$ , the slow time response moved to slightly higher frequencies and the second and third peaks eventually split into two new frequencies in their neighborhood. Also notice that there were higher frequency peaks (the fourth peak) grew in higher periodic forcing amplitude case as in  $\varepsilon = 0.09476$ . This fourth peak has frequency about 3 times larger than the second peak located at around 100 Hz. In Figure 4.15, we can also see that the fourth peak split into two frequencies in the higher forcing amplitude cases.

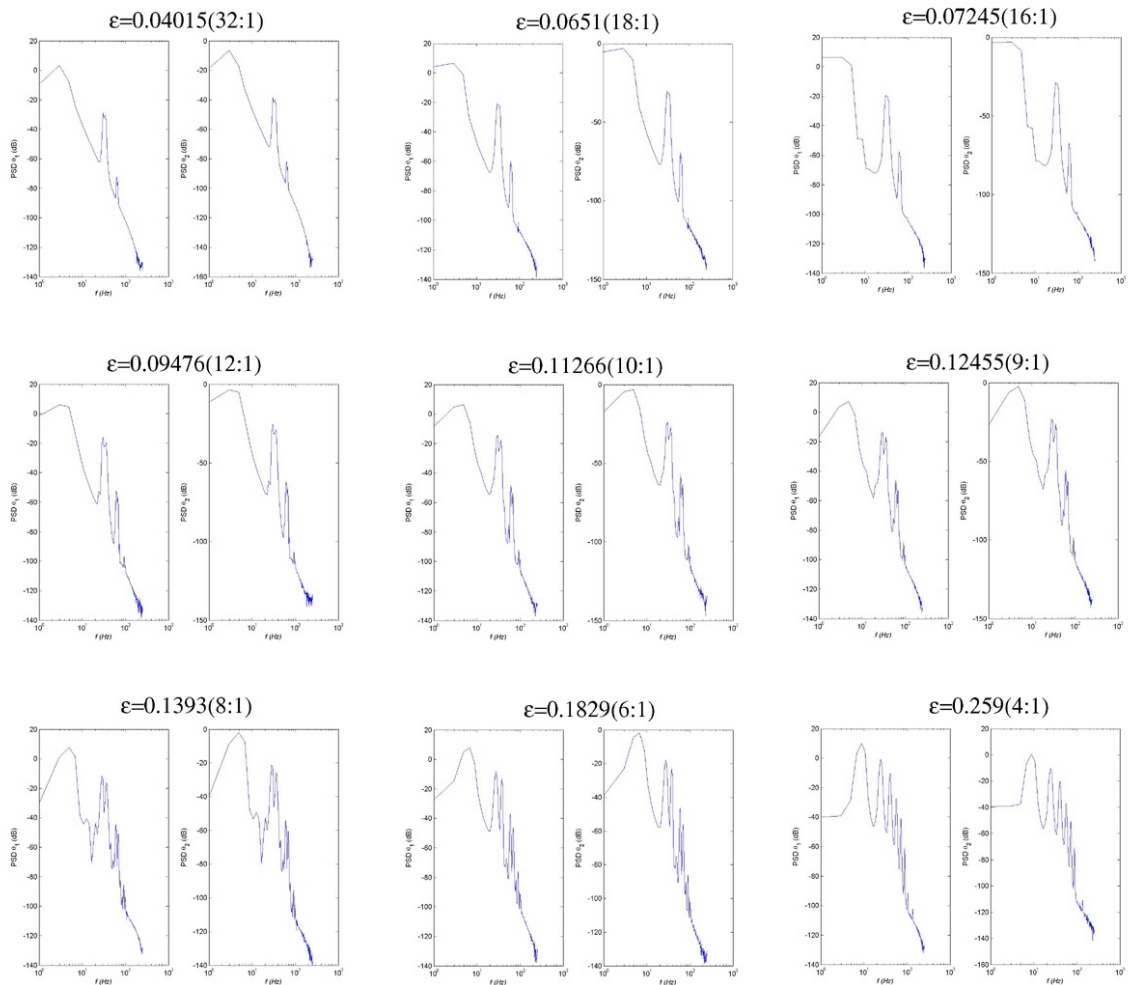


Figure 4.15: Power spectral density comparison of periodic solutions on numerical simulation using linear 2DOF inverted pendulum model. From upper left to lower right, the forcing amplitude has ascending values which result in descending frequency ratio.

## Chapter 5

# Experiments on the 2DOF Inverted Pendulum

### 5.1 Material and Methods for 2DOF Experimentations

As described in our 2DOF model as in Figure 4.2, two degree of freedom inverted pendulum experimental results also showed two modes of vibration. Figure 5.1 shows the snap shots of our experimental setup while the 2DOF pendulum was stabilized in a swinging motion around its upright vertical position under periodic forcing. On the left graph of Figure 5.1 the 2DOF inverted pendulum was under mode 1 vibration; on the right graph of Figure 5.1 the 2DOF inverted pendulum was under mode 2 vibration. Similar to our sDOF experimental setup, our 2DOF apparatus has its base mounted to a stand which is firmly mounted on the center cone of the speaker. In Figure 5.1, the base of the pendulum is labelled as 'Joint 1', in which the attachment is a ball-bearing made of stainless steel. The

first pendulum rod labelled as  $L_1$ , which is the same  $s$ DOF pendulum rod as in Figure 3.1. The first pendulum rod  $L_1$  measured as  $L_1 = 80.0 \pm 0.1mm$ . On top of the first pendulum rod  $L_1$  we added another pendulum rod  $L_2$  using another ball-bearing joint labelled as 'Joint 2' to make 2DOF setup. The second pendulum rod  $L_2$  measured as  $L_2 = 40.0 \pm 0.1mm$ . All ball-bearing used in our experimental setup are free to rotate on the pendulum  $XY$  plane. Each stainless steel made ball-bearing has heavier weight compare with pendulum rods in order to fulfill our theoretical model as described in Figure 4.2. Proper lubrication was used on all ball-bearings before we ran each experiment to ensure that the damping effect due to pendulum joint friction was minimized. We used the same speaker, function generator and amplifier setup as in  $s$ DOF experimentations as shown in Figure 3.3 to our 2DOF apparatus. During experiment the speaker cone was in a sinusoidal vertical motion  $u(t) = \varepsilon \cos \omega t$  to move the pendulum base where its forcing amplitude  $\varepsilon$  and forcing frequency  $\omega$  can be controlled by the function generator and the amplifier.

Similar to  $s$ DOF experiments, we applied a systematic way to drive the 2DOF pendulum base to appropriate forcing amplitude  $\varepsilon$  and forcing frequency  $\omega$  while released the pendulum from some initial conditions. All pendulum's swinging motion on the  $XY$  plane was captured using high speed camera with frame rate 500 frames per second. A ruler with  $10mm$  space tick marks on it was located at a fixed location on the right side of the background which we used to calibrate the pendulum physical size from the images captured from high speed camera. We mounted this ruler carefully to ensure that the ruler's straight line was aligned to the vertical direction as close as possible. For convenience, we

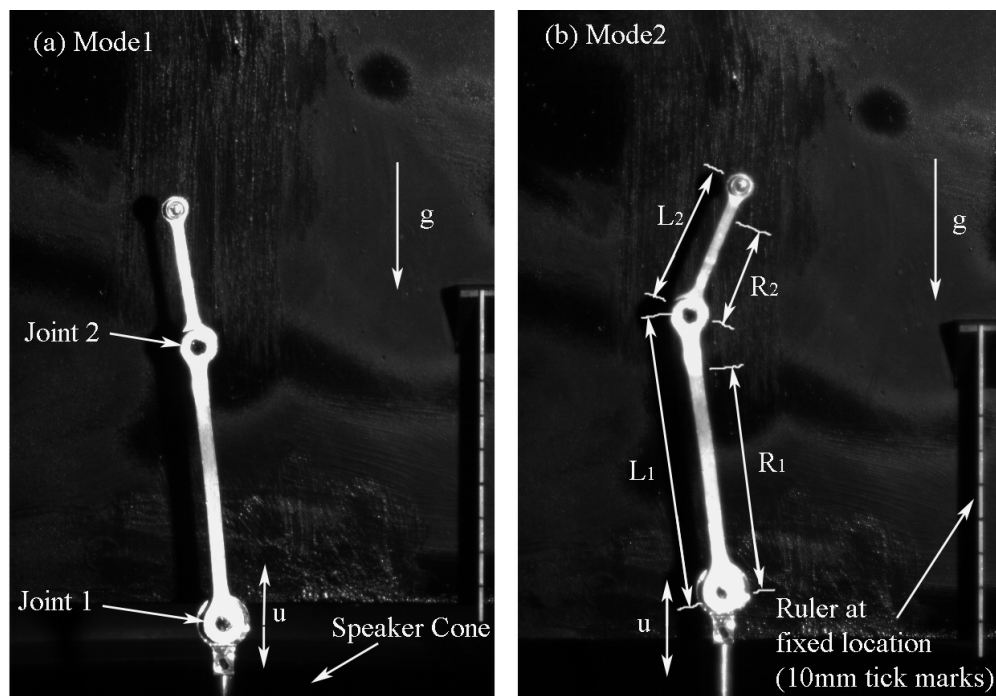


Figure 5.1: Two degree of freedom inverted pendulum experimental setup. (a) Mode 1 vibration. (b) Mode 2 vibration.

rotated the high speed camera with  $90^\circ$  angle which the images' wide aspect ratio could fit in more pendulum's swinging motion in camera view even when the pendulum was swinging in large angle motion. With new image aspect ratio on 2DOF setup, single image takes  $860 \times 604$  pixels of image resolution which is enough for a 1G byte of computer memory to capture up to 1.7 seconds of data. After we captured a sequence of images taking from high speed camera we used the same image processing tools, NI Vision Builder, as in sDOF case to measure 2DOF inverted pendulum's motion in a precise way. Figure 5.2 shows a screen shot of the NI Vision Builder used on a PC. Instead of vertical motion as in real experiments, the 2DOF inverted pendulum graph in Figure 5.2 shows horizontal motion due to  $90^\circ$  rotation of the camera where the gravitational acceleration  $g$  is now on a horizontal position pointing to the right. There were many regions of interest shown in Figure 5.2 in a red-color or green-color boxes which indicate the pendulum motion was measured from following the motion of the pendulum shape in the sequence of images captured from high speed camera. Individual pendulum angles can be measured from comparing the the difference of the pendulum's straight edge to the straight edge of the ruler mounted on the background. The pendulum's response can then be obtained from the evolution of pendulum angles change in different frame sequences of images. This pendulum response measurements were in high precision since the high speed camera was capturing in a high frame rate as 500 frames per second which resulted in high resolution time traces.

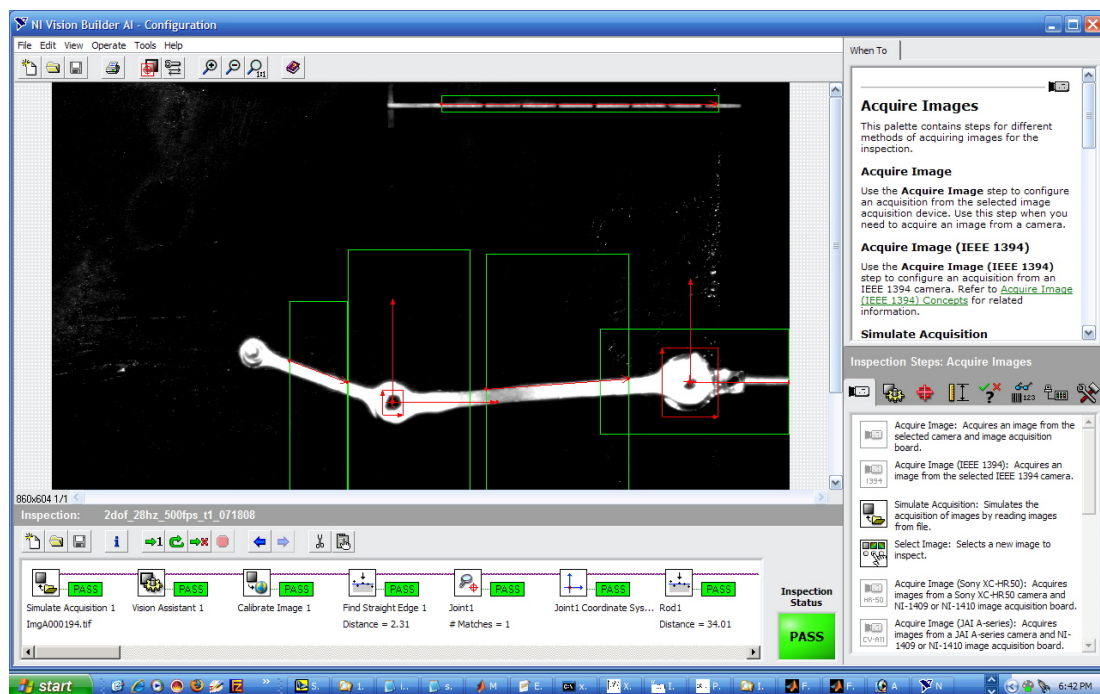


Figure 5.2: NI Vision Builder on two degree of freedom experimental setup.

## 5.2 2DOF System Experimental Results

Our 2DOF experimentations also showed two modes of vibration. Figure 5.3, 5.4 and 5.5 present our experimental results of 2DOF inverted pendulum under mode 1 vibration; Figure 5.6, 5.7 and 5.8 present our experimental results of 2DOF inverted pendulum under mode 2 vibration. Notice that there always exist the upright vertical mode when the pendulum doesn't swing as in Figure 5.9, 5.10 and 5.11. We didn't discuss the upright vertical mode much since our research interest was in searching for multiple frequency periodic responses of an inverted pendulum under periodic forcing. However, from stability point of view, the upright vertical mode is the asymptotic solution for the two modes of vibration in a stable condition when the system encounter damping effect.

### Experimental Results on 2DOF Mode 1 Vibration

In Figure 5.3, part (a) shows the input periodic forcing which we present the raw data on top graph and the filtered data at the bottom. We applied the same Butterworth low pass filter as described in *s*DOF case. The periodic forcing amplitude was  $\varepsilon = 0.0085 \pm 0.0005$  m while the periodic forcing frequency was  $\omega = 30.0 \pm 0.1$  Hz. We started from some initial conditions away from upright vertical position and this 2DOF pendulum was swinging under mode 1 vibration around its inverted position. In part (b) graph, we also measured the horizontal motion of the pendulum base in order to make sure that there is little effect from the horizontal direction to fulfill our assumption. The horizontal motion measured as  $y = 0.0 \pm 0.2$  mm which is negligible compare the amplitude of vertical forcing. In part (c) graph, two inverted pendulum rods' response present in time traces with comparison of the

input periodic forcing. This shows that two pendulum rods are in mode 1 vibration where their motions are in the same directions. Notice that the damping effect can also be seen from graph in part (c) where two pendulum's maximum swinging amplitude decreased in later timing. Graph in part (d) shows the angular velocity of two pendulum rods, their motions also show in a synchronize directions and a detail zoom-in view can be seen from part (f) graph. Part (e) graph shows a zoom-in view of part (c) which indicates that fast time response of two pendulum rods synchronize with the input periodic forcing frequency at  $\omega = 30.0 \pm 0.1$  Hz.

Figure 5.4 presents the same 2DOF experimental results as in Figure 5.3 in a different manner. We separated Figure 5.4 in left and right portions where left graphs present the response of the first pendulum rod while right graphs present the response of the second pendulum rod. All graphs were shown in comparison of its raw data points(top) to filtered data(bottom). Notice that in part (e) and (f), the phase portrait generated from raw data points were not recognizable without data filtering. We measured this 2DOF inverted pendulum response as 36 : 1 frequency ratio. Mode 1 pendulum response is very much alike the *s*DOF case. This can be seen from adding stiffness to joint 2 of our 2DOF model to become a *s*DOF model. The power spectral density graphs of 2DOF inverted pendulum in Figure 5.5 also show similar results as in *s*DOF case. Top portion of graphs indicate raw experimental data while the bottom graphs are filtered data. There are two clear peaks in our PSD graph in Figure 5.5, the largest peak happened at low frequency around 1 Hz which corresponds to the system slow time, the second peak located at around 30 Hz which corresponds to periodic forcing frequency.

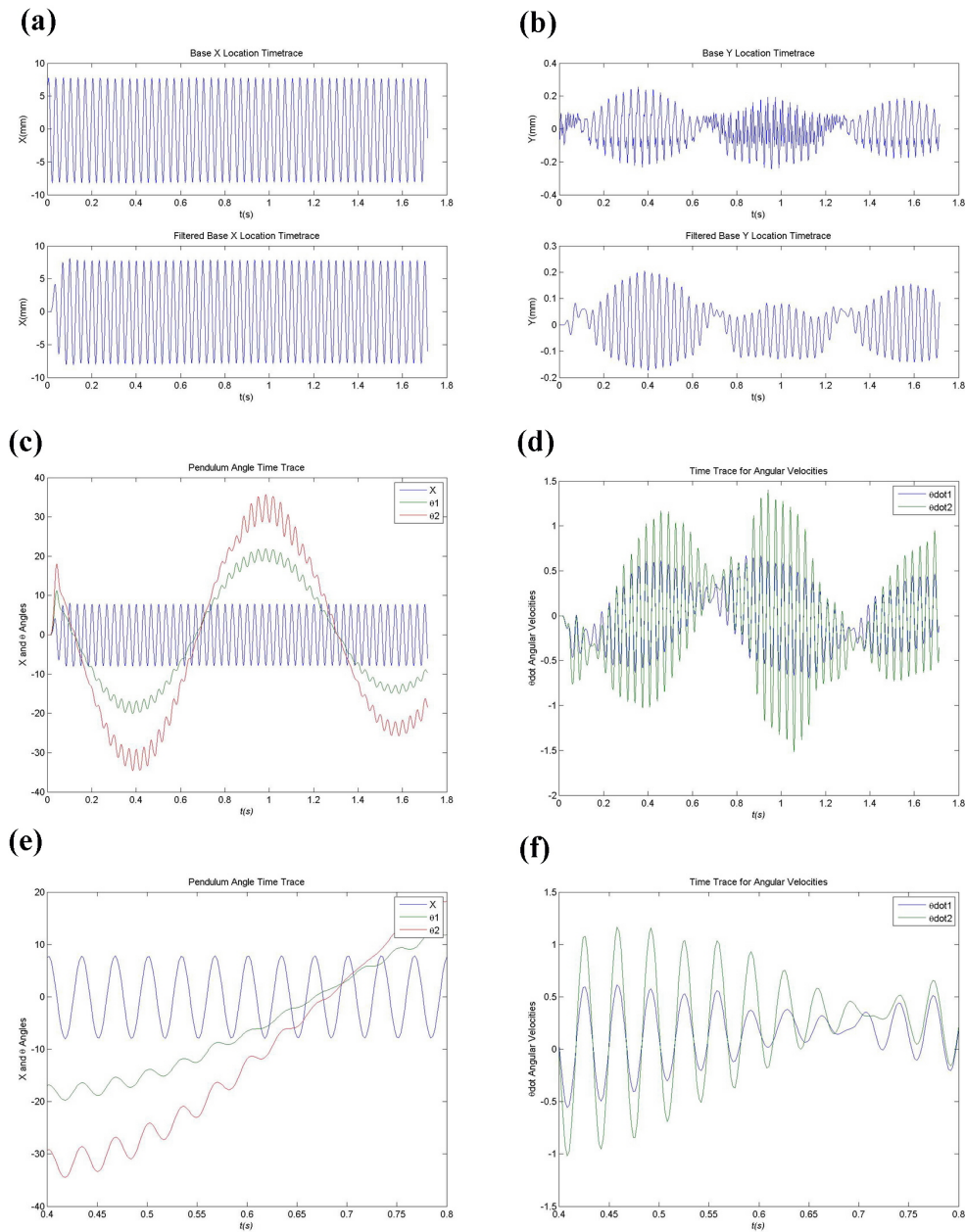


Figure 5.3: Experimental result on 2DOF inverted pendulum under periodic forcing amplitude  $\varepsilon = 0.0085 \pm 0.0005$  m and periodic forcing frequency  $\omega = 30.0 \pm 0.1$  Hz. System is under mode 1 vibration. (a)periodic forcing (b)pendulum base horizontal movement (c)time traces of system response (d)time traces of system angular velocity (e)time traces zoom-in view of system response (f)time traces zoom-in view of system angular velocity.

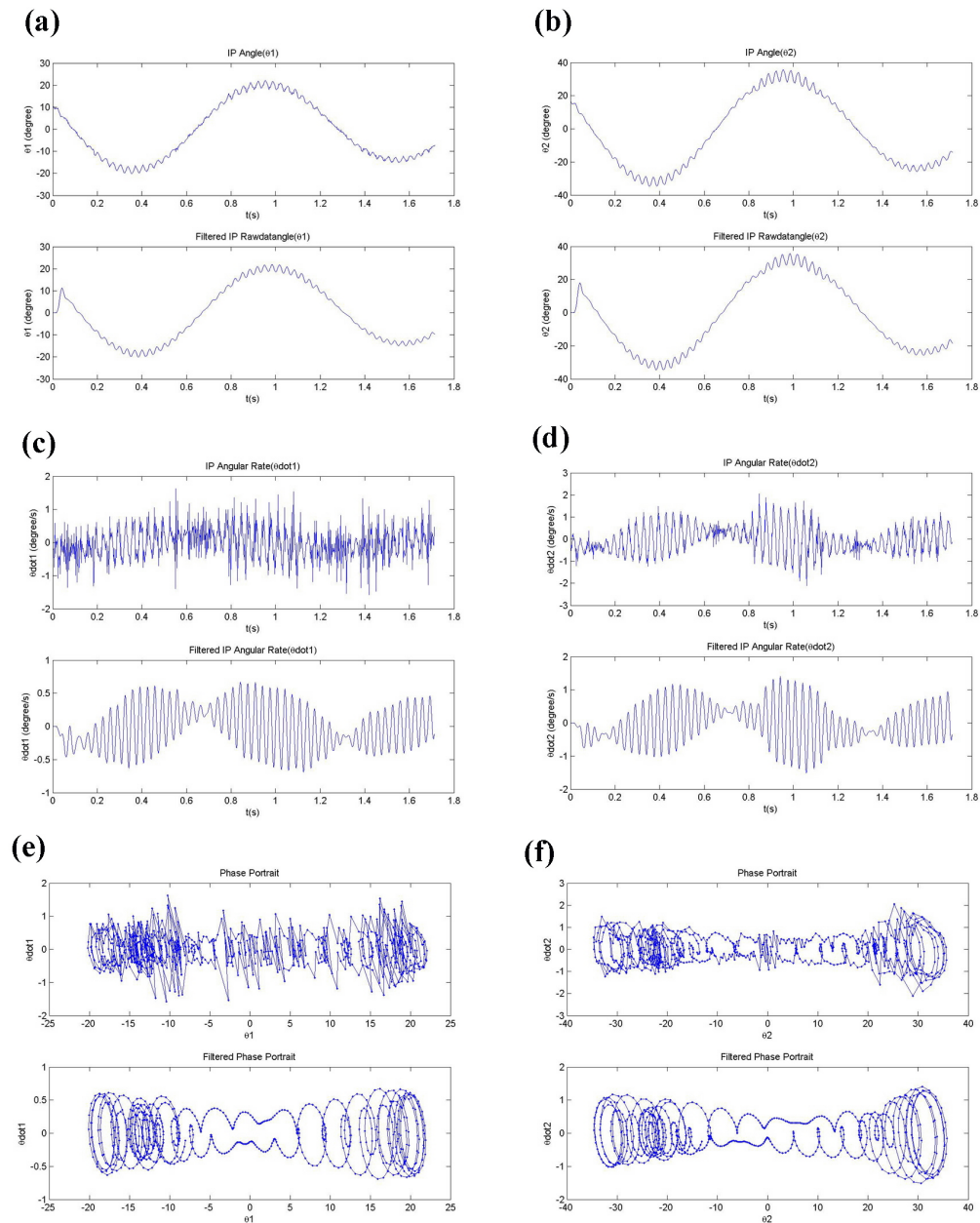


Figure 5.4: Experimental result on 2DOF inverted pendulum under periodic forcing amplitude  $\varepsilon = 0.0085 \pm 0.0005$  m and periodic forcing frequency  $\omega = 30.0 \pm 0.1$  Hz. System is under mode 1 vibration. Left graphs indicate the system response of the first pendulum; right graphs indicate the system response of the second pendulum.

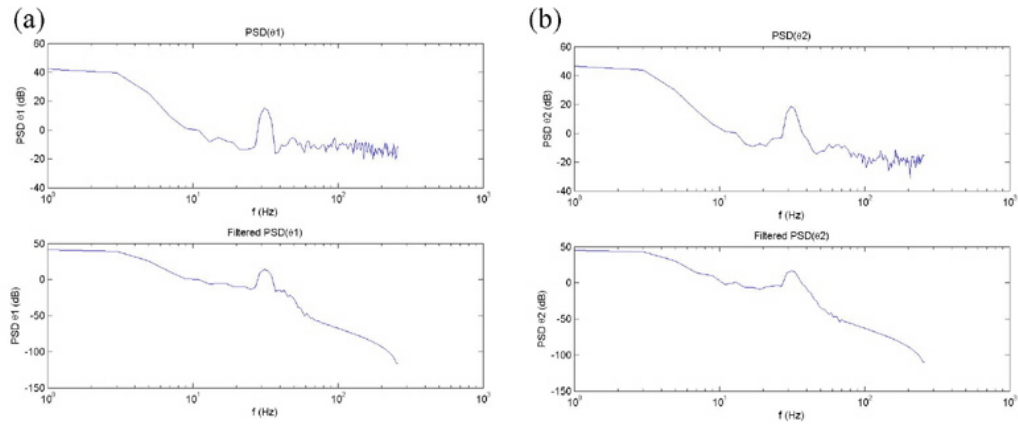


Figure 5.5: Power spectral density graphs of 2DOF inverted pendulum under periodic forcing amplitude  $\varepsilon = 0.0085 \pm 0.0005$  m and periodic forcing frequency  $\omega = 30.0 \pm 0.1$  Hz. System is under mode 1 vibration. (a)PSD for the first pendulum (b)PSD for the second pendulum.

## Experimental Results on 2DOF Mode 2 Vibration

In Figure 5.6, part (a) shows the input periodic forcing which we present the raw data on top graph and the filtered data at the bottom. We applied the same Butterworth low pass filter as described in  $s$ DOF case. Notice that our input forcing shows periodic pattern in part (a) graph, however, it is not a harmonic function as  $u(t) = \varepsilon \cos \omega t$ . There were two forcing amplitudes appeared in the time traces. This phenomenon happened in all our 2DOF mode 2 experimentations. One possible explanation on this phenomenon is that it may exceed our speaker's driving capability while the 2DOF inverted pendulum is under mode 2 vibration. Due to this effect we enlarge the measuring uncertainty on forcing amplitude as  $\varepsilon = 0.008 \pm 0.003$  m with the periodic forcing frequency as  $\omega = 30.0 \pm 0.1$  Hz. In part (b) graph, we also measured the horizontal motion of the pendulum base in order to make sure that there is little effect from the horizontal direction to fulfill our assumption.

The horizontal motion measured as  $y = 0.0 \pm 0.2$  mm which is negligible compare the amplitude of vertical forcing. In part (c) graph, two inverted pendulum rods' response present in time traces with comparison of the input periodic forcing. This shows that two pendulum rods are in mode 2 vibration where their motions are in the opposite directions. Unlike mode 1 case which has obvious damping effect, mode 2 vibration only show little damping effect as can be seen from part (c) graph. Graph in part (d) shows the angular velocity of two pendulum rods, their motions also show in opposite directions and a detail zoom-in view can be seen from part (f) graph. Part (e) graph shows a zoom-in view of part (c).

Figure 5.7 presents the same 2DOF experimental results as in Figure 5.6 in a different manner. We separated Figure 5.7 in left and right portions where left graphs present the response of the first pendulum rod while right graphs present the response of the second pendulum rod. All graphs were shown in comparison of its raw data points(top) to filtered data(bottom). Notice that in part (e), the phase portrait generated from raw data points were not recognizable without data filtering. Our experimental results in 2DOF mode 2 vibration case doesn't match with our numerical simulation results due to different forcing inputs. Under this usual forcing input, our experimental result showed frequency ratio near 2 : 1 which we couldn't find from any of our simulation result provided only harmonic forcing input.

The power spectral density graphs of 2DOF inverted pendulum in Figure 5.8 show multiple peaks in various frequency locations. Top portion of graphs indicate raw experimental data while the bottom graphs are filtered data.

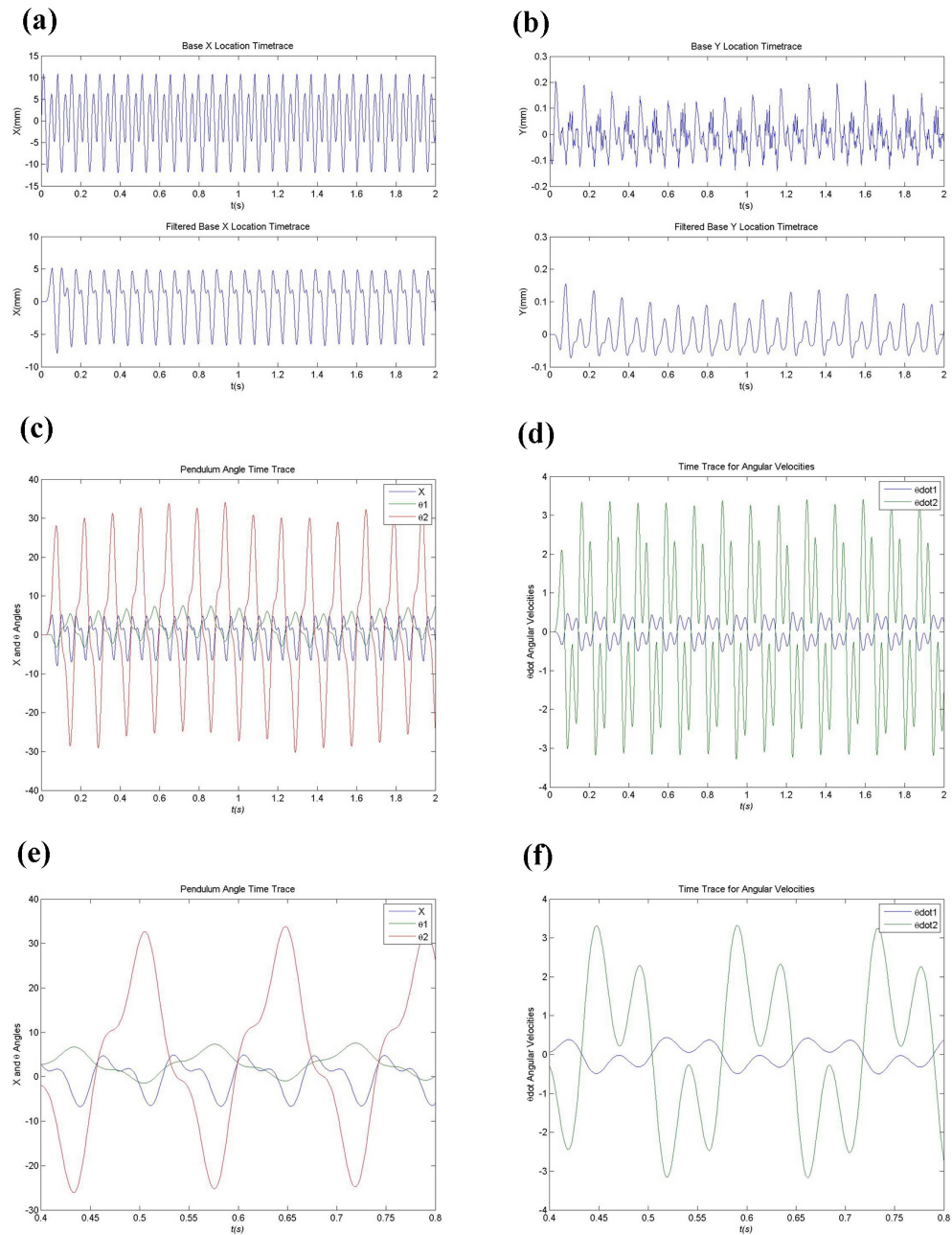


Figure 5.6: Experimental result on 2DOF inverted pendulum under periodic vertical forcing. The forcing frequency was  $\omega = 28.0 \pm 0.1$  Hz. System is under mode 2 vibration. Notice that the input forcing was not harmonic which had two forcing amplitudes involved.

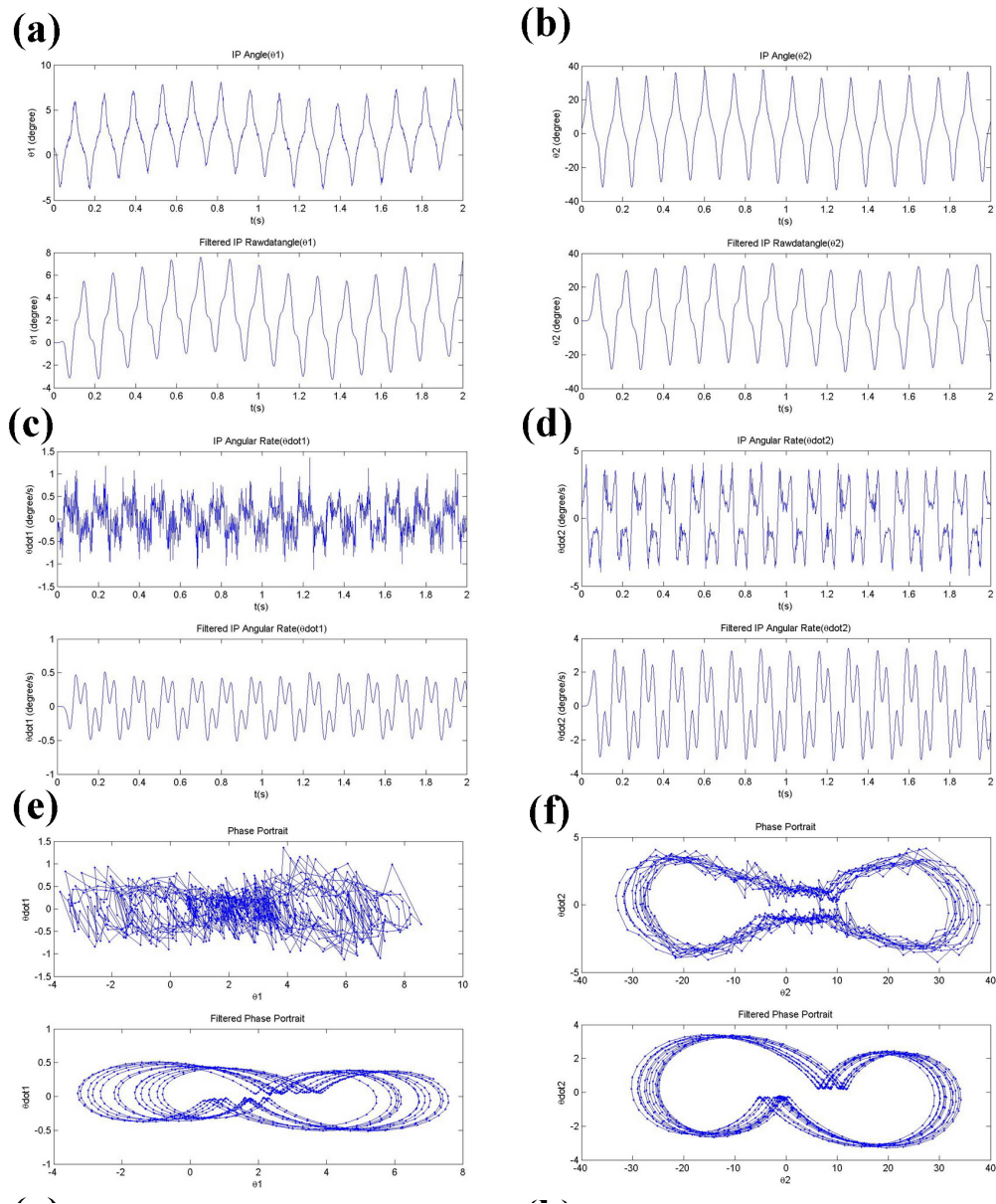


Figure 5.7: Experimental result on 2DOF inverted pendulum under periodic vertical forcing. The forcing frequency was  $\omega = 28.0 \pm 0.1$  Hz. System is under mode 2 vibration. Left graphs indicate the system response of the first pendulum; right graphs indicate the system response of the second pendulum.

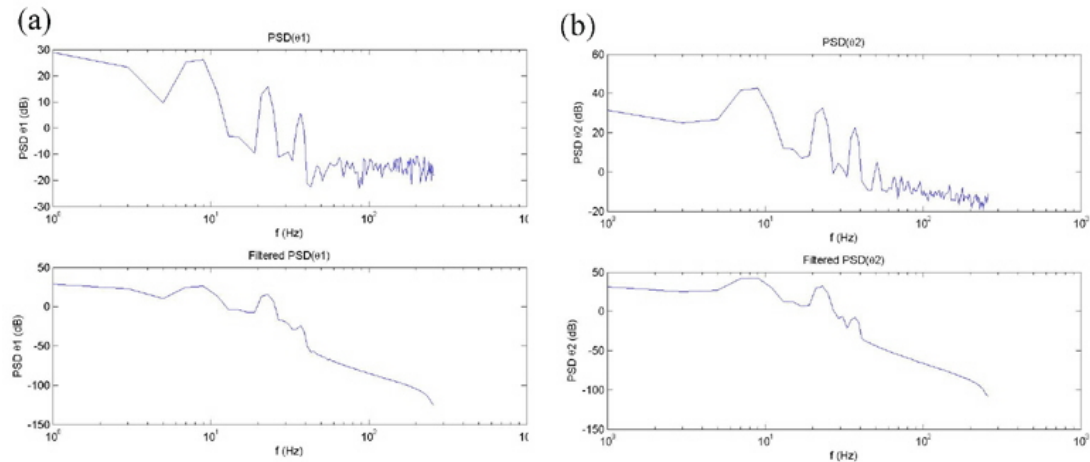


Figure 5.8: Power spectral density graphs of 2DOF inverted pendulum under periodic vertical forcing. The forcing frequency was  $\omega = 28.0 \pm 0.1$  Hz. System is under mode 2 vibration. (a)PSD for the first pendulum (b)PSD for the second pendulum.

## Experimental Results on 2DOF Upright Vertical Mode

Figure 5.9 presents the 2DOF pendulum stabilized in its upright vertical position. This can be obtained from assigning the initial conditions as close to zero as possible at start up. In part (a) shows the input periodic forcing which we present the raw data on top graph and the filtered data at the bottom. We applied the same Butterworth low pass filter as described in *sDOF* case. In part (b) graph, we measured the horizontal motion of the pendulum base as  $y = 0.0 \pm 0.1$  mm. In part (c) graph, two inverted pendulum rods' response present in time traces with comparison of the input periodic forcing. This graph indicates that two pendulum rods were in near vertical position without swinging. Same effect can be seen from part (d) where two pendulum rods' angular velocity were small. Same conclusions can be seen in zoom-in view in part (e) and (f).

Figure 5.10 presents the same 2DOF experimental results as in Figure 5.9 in a

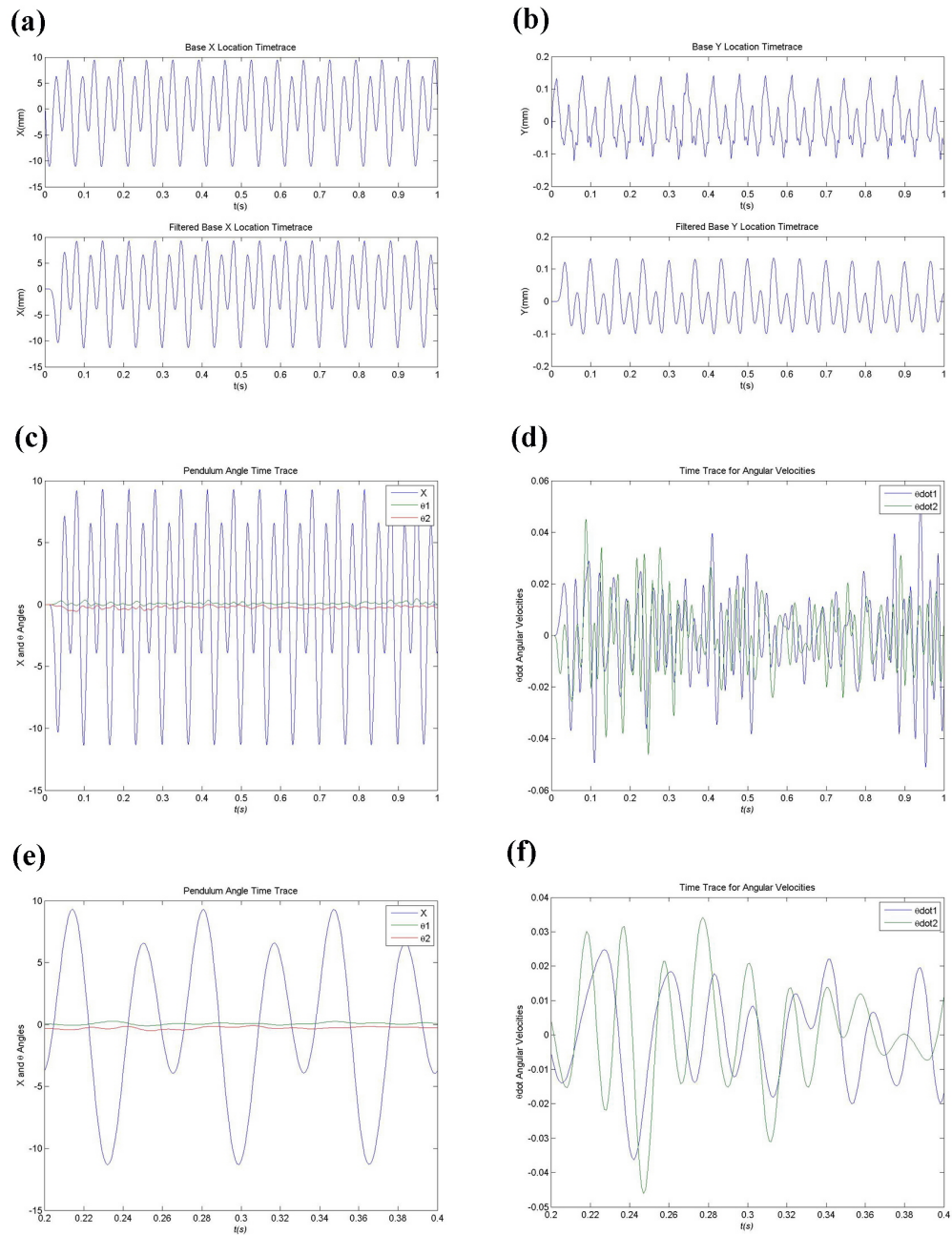


Figure 5.9: Experimental result on 2DOF inverted pendulum under periodic vertical forcing with 0 initial condition. The forcing frequency was  $\omega = 30.0 \pm 0.1$  Hz. Notice that the input forcing was not harmonic which had two forcing amplitudes involved.

different manner. We separated Figure 5.10 in left and right portions where left graphs present the response of the first pendulum rod while right graphs present the response of the second pendulum rod. All graphs were shown in comparison of its raw data points(top) to filtered data(bottom). Notice that in part (e) and (f), their phase portrait graphs indicate that two pendulum rods stayed in their upright vertical position with very little movement. Under upright vertical mode of 2DOF inverted pendulum, it's power spectral density graphs as in Figure 5.11 cannot conclude any harmonic peak.

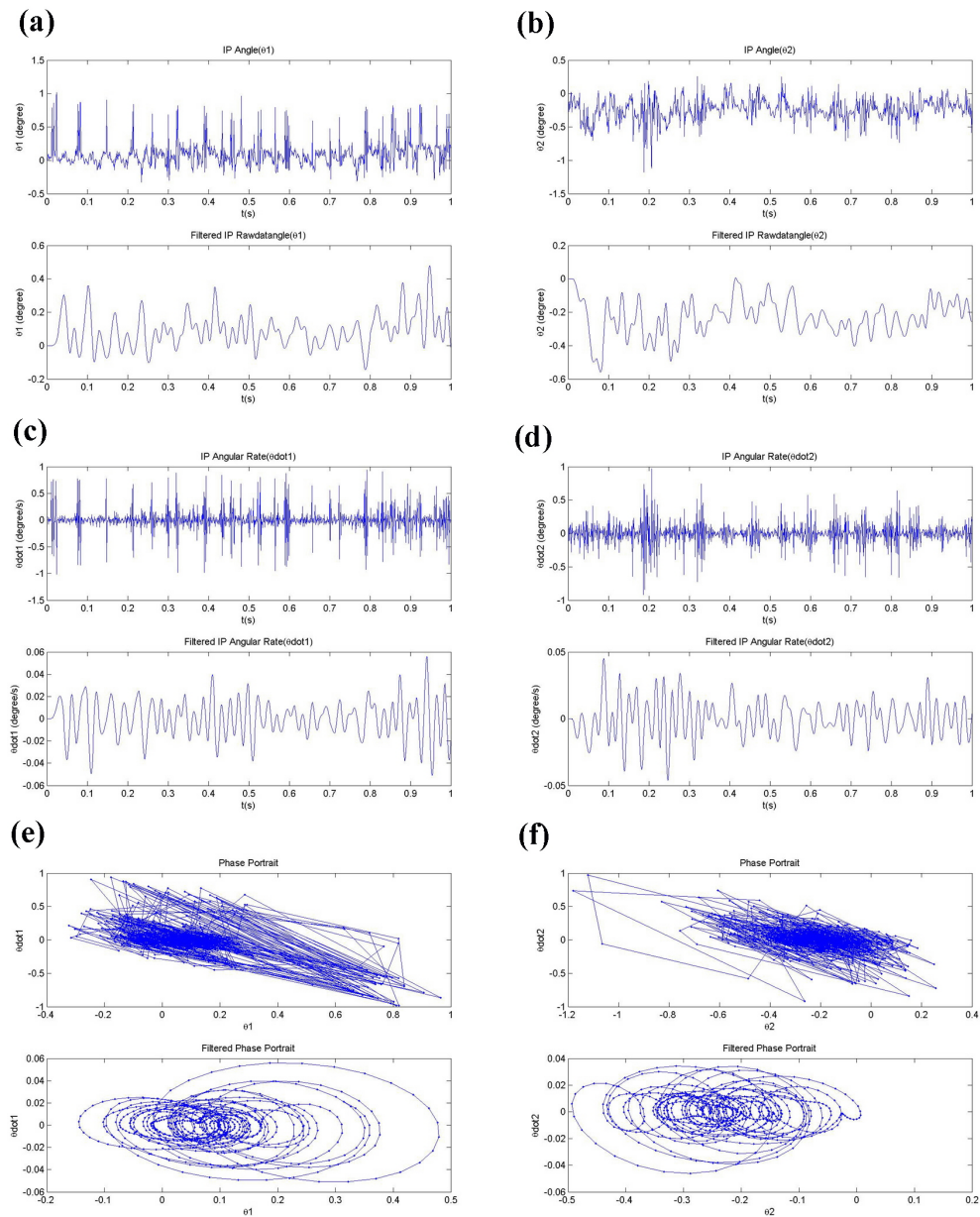


Figure 5.10: Experimental result on 2DOF inverted pendulum under periodic vertical forcing with 0 initial condition. The forcing frequency was  $\omega = 30.0 \pm 0.1$  Hz. Notice that the input forcing was not harmonic which had two forcing amplitudes involved.

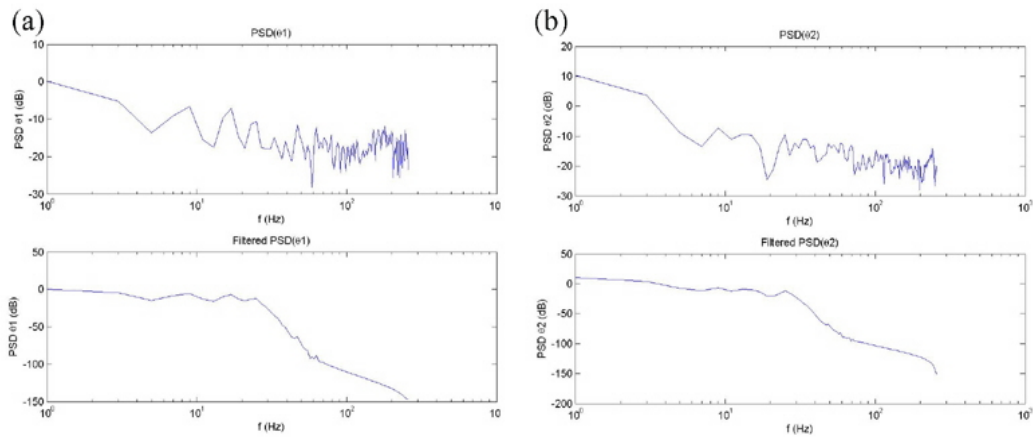


Figure 5.11: Power spectral density graphs of 2DOF inverted pendulum under periodic vertical forcing with 0 initial condition. The forcing frequency was  $\omega = 30.0 \pm 0.1$  Hz.

## Chapter 6

# Summary and Future Work

Our research shows that under stable conditions near a pendulum's inverted state, as the number of degree of freedom increase, the maximum angle of the pendulum's swinging motion decreases. In this paper, we presented four ways to characterize the pendulum's periodic responses, allowing us to conclude that when the periodic forcing amplitude increases, the frequency ratio decreases and the system slow time response will move to higher frequency resulting in faster system response. The power spectral density graph has fewer harmonic peaks when the periodic forcing amplitude is low. As we increase the periodic forcing amplitude, those few harmonic peaks will split into multiple frequency peaks. These statements are true for both  $s$ DOF case and 2DOF case.

In searching for the periodic solutions of an inverted pendulum under periodic vertical forcing to its base, our research shows that our numerical simulation results match reasonably well with our experimental results, quantitatively for the single degree of freedom case, and qualitatively for the multi-degree of freedom case. Although we carefully

constructed our 2DOF experimental setup in order to fulfill our theoretical model as described in Figure 4.2, each pendulum's center of mass still has some offset location away from the pivot point which contradicts our initial assumption of point-mass pendulum model. This can be seen from Figure 5.1, in which we measured the combined center of mass for the first pendulum located at  $R_1 = 53.7 \pm 0.1$  mm with combined weight measured as  $m_1 = 3.8 \pm 0.1$  g; the combined center of mass for the second pendulum located at  $R_2 = 25.1 \pm 0.1$  mm with combined weight measured as  $m_2 = 1.9 \pm 0.1$  g. We can construct a modified theoretical model as described in Figure 6.1 to further match our 2DOF experimental setups. We leave this to our future work to tighten up the agreement between our theoretical predictions and experiments.

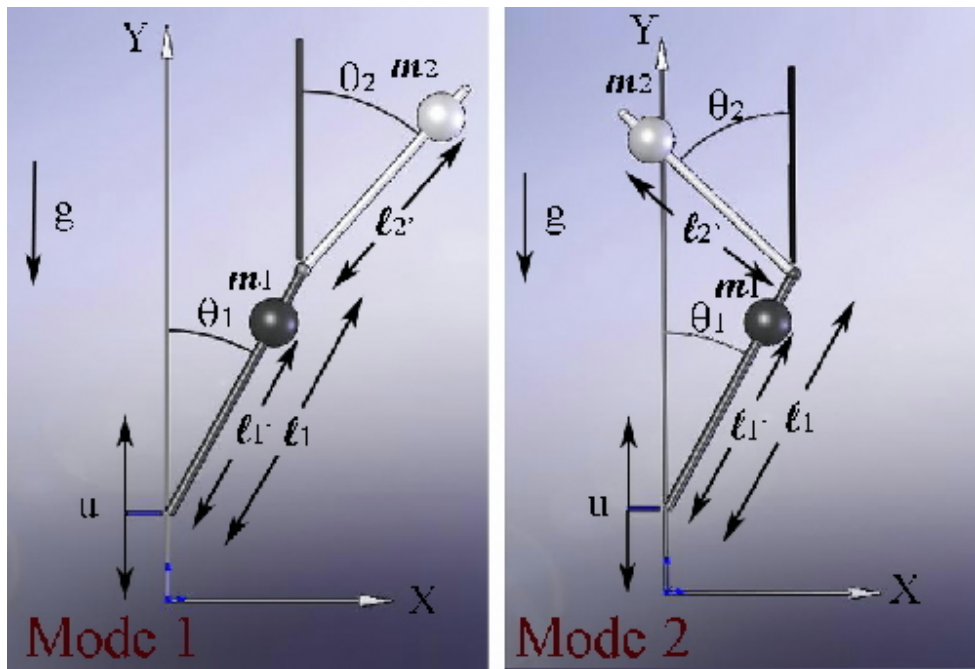


Figure 6.1: Modified 2DOF model has each pendulum's center of mass offset to a new location different than the pivot point.

# Bibliography

- [1] Acheson, D.J., *Multiple-nodding oscillations of a driven inverted pendulum*. Proc. R. Soc Lond. A448, 89-95. 1995.
- [2] Acheson, D.J., *A pendulum theorem*. Proc. R. Soc Lond. A443, 239-245. 1993.
- [3] Acheson, D.J. & Mullin, T., *Upside-down pendulum*. Nature, Lond. 366, 215-216. 1993.
- [4] Acheson, D.J. & Mullin, T., *'Ropy magic'*. New Scientist. February, 32-33. 1998.
- [5] Arnol'd, V. I., Kozlov, V. V., and Neishtadt, A. I., *Mathematical Aspects of Classical and Celestial Mechanics*, volume 3 of Encyclopaedia of Mathematical Sciences (Berlin: Springer-Verlag). 1985.
- [6] Arnscoff, F.M., *Latent roots of tri-diagonal matrices*. Proc. Edinburgh Math. Soc., 12. Edinburgh Math. Notes No. 44. 1961.
- [7] Baillieul, J., *Stable average motions of mechanical systems subject to periodic forcing*. In Dynamics and Control of Mechanical Systems: The Falling Cat and Related Problems: Fields Institute Communications (Providence, RI: American Mathematical Society), pp. 1~23. 1993.
- [8] Baillieul, J., *Energy methods for the stability of bilinear systems with oscillatory inputs*. Int. J. Robust and Nonlin. Cont., July, Special Issue on the 'Control of Nonlinear Mechanical Systems', pp. 285~301. 1995.
- [9] Baillieul, J., *The geometry of controlled mechanical systems*. In J. Baillieul and J. C. 1998.
- [10] Baillieul, J., and Weibel, S. P., *Scale dependence in the oscillatory control of micro-mechanisms*. Submitted to the 1998 IEEE Conference on Decision and Control (Tampa, FL). 1998.
- [11] Berlioz A, Dufour R. & Sinha S.C, *Experimental and Numerical Investigation of a Non-linear Autoparametric System*. ASME Design Technical Conferences, DETC97/VIB-4027. 1997.
- [12] Blackburn, J. A., Smith, H. J. T. & Gronbech-Jensen, N., *Stability and Hopf bifurcations in an inverted pendulum*. Am. J. Phys. 60, 903-908. 1992.

- [13] Bogoliubov, N. N., and Mitropolsky, Y. A., *Asymptotic Methods in the Theory of Nonlinear Oscillators*. International Monographs on Advanced Mathematics and Physics (New York: Gordon and Breach). 1961.
- [14] Byrd P.& Friedman M., *Handbook of Elliptic Integrals for Engineerings and Physicists*. Springer Verlag. 1954.
- [15] Champneys, A. & fraser, W. '*The Indian rope trick*' for a continuously flexible rod; *linearized analysis*. Proc. Roy. soc. Lond. A 456, 553-570. 2000.
- [16] Dombovari Z., Wilson R.E., Stepan G., *Estimates of the Bistable Region in Metal Cutting*. (1)Department of Applied Mechanics, Budapest university of Technology and Economics, Budapest, Hungary. (2)Department of Engineering Mathematics, University of Bristol, Bristol, UK.
- [17] Feng, Z. C., and Leal, L. G., *Nonlinear bubble dynamics*. Ann. Rev. Fluid Mechanics,29, 201~243. 1997.
- [18] Flashner, H. & Hsu, C.S., *A study of nonlinear periodic systems via the point mapping method*. International Journal for Numerical Methods in Engineering. Vol. 19. 185-215. 1983.
- [19] Gani, Ferawati., *Parametric excitation of stay-cables*. University of Ottawa (Canada) ; AAT MR01476. 2004.
- [20] Henry Dan, *Perturbation of the Boundary in Boundary-Value Problems of Partial Differential Equations*. Cambridge University Press. ISBN-10 0-521-57491-9. 2005.
- [21] Howell G.W, Ono K., *The connection between n-link chains and the continuum models*. Boston University Center for Biodynamics. 1998.
- [22] Howell G.W, *Analysis and control of Super-Articulated Biped Robots*. PhD thesis, Boston University. 2000.
- [23] Jeffrey, A., *Handbook of Mathematical Formulas and Integrals*. Academic Press Inc. ISBN 0-12-382580-6, 231-234. 1995.
- [24] Johnson, R.S., *Singular Perturbation Theory*. Springer Science + Business Media, Inc. ISBN 0-387-23200-1. 2004.
- [25] Kalmus, H. P., *The inverted pendulum*. Am. J. Phys. 38, 874-878. 1970.
- [26] Kaaajakari, Ville Pekka, *Ultrasonic surface micromachine actuation: Applications to release, microstructure assembly, and micromotors*.The University of Wisconsin - Madison ; AAT 3060427. 2002.
- [27] Khalil Hassan K. *Nonlinear Systems*. Third Edition. Prentice Hall. ISBN 0-13-067389-7, 2002.

- [28] Kim, S. and Hu, B. *Bifurcations and transitions to chaos in an inverted pendulum*. Physical Review E, Vol. 58, No. 3, pp. 3028-3035, 1998.
- [29] Kuo, A.D., Donelan, J.M., and Ruina, A. *Energetic consequences of walking like an inverted pendulum: step-to-step transitions*. Exerc. Sport Sci. Rev., Vol. 33, No. 2, pp. 88-97, 2005.
- [30] Kuznetsov Yuri A. *Elements of Applied Bifurcation Theory*. Third Edition. Springer-Verlag New York, LLC. ISBN 0-387-21906-4, 2004.
- [31] Levi, M., and Weckesser, W., *Stabilization of the inverted pendulum by high frequency vibrations*. SIAM Review, 27, 219~223. 1995.
- [32] Marcus, M., and Minc, H., *A Survey of Matrix Theory and Matrix Inequalities* (New York: Dover). 1994.
- [33] McLaughlin, J. *Period-doubling bifurcations in the parametrically forced pendulum*. Journal of Statistical Physics, Vol. 24, pp. 375-338, 1981.
- [34] Meirovitch L, *Fundamentals of Vibrations*. McGraw-Hill Companies. ISBN 0-07-288180-1. 2001.
- [35] Mennem R. C., *Parametrically excited vibrations in spiral bevel geared systems*. Purdue University ; AAT 3150802. 2004.
- [36] Michaelis M., *Stroboscopic Study of the Inverted Pendulum*. Am. J. Phys. 53(11) November 1985.
- [37] Mullin T., Champneys A., Barrie Fraser W., Galan J., Acheson D.. *The 'Indian rod trick' via parametric excitation*. Proc. Roy. soc. Lond.
- [38] Morrison T., *Three Problems in Nonlinear Dynamics with 2:1 Parametric Excitation*., Cornell University, 146 pages; AAT 3227288. 2006.
- [39] Nayfeh, A. H., *Introduction to Perturbation Techniques*. John Wiley & Son, Inc. ISBN 0-471-31013-1. 1981.
- [40] Nayfeh, A. H., *Perturbation Methods*. John Wiley & Son, Inc. ISBN 0-471-63059-4. 1973.
- [41] Nayfeh, A. H., *Problems in Perturbation*. John Wiley & Son, Inc. ISBN 0-471-82292-2. 1985.
- [42] Newton Paul K., *The N-Vortex problem: analytical techniques*. Applied mathematical sciences. Springer-Verlag New York, Inc. ISBN 0-387-95226-8. 2001.
- [43] Ng, Leslie Ho-Ming, *Three problems in parametric excitation*. , Cornell University, 159 pages; AAT 3050435. 2002.
- [44] Pai Frank. *Highly Flexible Structures: Modeling, Computation, and Experimentation*. American Institute of Aeronautics and Astronautics, Inc. ISBN-10 1-56347-917-6. 2007.

- [45] Rand R.H, Armbruster D., *Perturbation methods, bifurcation theory and computer algebra*. Applied Mathematical Sciences, 65. Springer-Verlag, NY, USA. 1987.
- [46] Rand R. H., Morrison T.M., *2:1:1 Resonance in the Quasiperiodic Mathieu Equation*. Nonlinear Dynamics 40:195-203. 2005.
- [47] Rand R. H., Barcilon A., Morrison T. M. *Parametric Resonance of Hopf Bifurcation*, Nonlinear Dynamics 39:411-421. 2005.
- [48] Sredynska M., Hanyga A., *Nonlinear differential equations with fractional damping with applications to the 1dof and 2dof pendulum*. Acta Mechanica. Vol.176, Iss. 3-4; p. 169. 2005.
- [49] Smith H. J. T. & Blackburn J. A., *Experimental study of an inverted pendulum*. Am. J. Phys. 60, 909-911. 1992.
- [50] Spears, Brian Keith, *Nonlinear dynamics of quasiperiodically driven oscillators: Knotted torus attractors and their bifurcations*. University of California, Berkeley, 115 pages; AAT 3147013. 2004.
- [51] Stephan G., Insperger T. & Szalai R., *Nonlinear Dynamics of High-speed Milling*, Budapest University of Technology and Economics, Hungary. 2005.
- [52] Stephan G., Insperger T. & Szalai R., *Delay, Parametric Excitation, and the Nonlinear Dynamics of Cutting Process*. International Journal of Bifurcation and Chaos 15 9:2783. 2005.
- [53] Stephenson A., *Memoirs and Proceedings of the Manchester Literary and Philosophical Society* 52(8), 1-10. *On a new type of dynamic stability*. 1908.
- [54] Stephenson A., *Philosophical Magazine* 15, 233-236. *On induced stability*. 1908.
- [55] Strogatz, S.H., *Nonlinear Dynamics and Chaos*. Addison-Wesley Publishing Company. ISBN 0-201-54344-3. 1994.
- [56] Weibel S., Baillieul J., Lehman B., *Equilibria and stability of an n-pendulum forced by rapid oscillations*, Decision and Control, Proceedings of the 36th IEEE Conference on Volume2, Issue , 10-12 Dec 1997 Page(s):1147-1152 vol.2, Digital Object Identifier 10.1109/CDC.1997.657602. 1997.
- [57] Weibel S., *Applications of Qualitative methods in the nonlinear control of superarticulated mechanical systems*. PhD thesis, Boston University. 1997.
- [58] Weibel S., Baillieul J., *Oscillatory control of bifurcations in rotating chains*. In Proceedings of 1997 ACC, Albuquerque, NM, pp. 2713~2717. 1997.
- [59] Weibel S., Baillieul J., *Averaging and energy methods for robust open-loop control of mechanical systems*. In J. Baillieul, S. Sastry, and H. Sussmann (Eds), *Essays in Mathematical Robotics*, (Berlin: Springer-Verlag), pp. 203~270. 1998.

- [60] Weibel S., Baillieul J., Kaper T. J., *Small-amplitude periodic motions of rapidly forced mechanical systems*. In Proceedings of 34th IEEE CDC, New Orleans, LA, pp.533~539. 1995.
- [61] Weibel S., Baillieul J., Lehman, B., *Equilibria and stability of an  $n$ -pendulum forced by rapid oscillations*. In Proceedings of 36th IEEE CDC, San Diego, CA, pp.1147~1152. 1997.
- [62] Weibel S., Baillieul J., *Open-loop oscillatory stabilization of an  $n$ -pendulum*. International Journal of Control, Volume 71, Number 5, 16 November 1998 , pp.931-957(27).
- [63] Weibel S., Kaper T. J., Baillieul J., *Global dynamics of a rapidly forced cart and pendulum*. Nonlin. Dyn., 13, 131~170. 1997.
- [64] P. A. Vela, *Averaging and Control of Nonlinear Systems*. Ph.D. thesis, California Institute of Technology, 2003.
- [65] P. A. Vela, K. A. Morgansen, and J. W. Burdick. *Second-order averaging methods for oscillatory control of underactuated mechanical systems*. In Proceedings of the American Control Conference, 2002.
- [66] Yagasaki K., Ichikawa T. *Higher-order averaging for periodically forced weakly nonlinear systems*. International Journal of Bifurcation and Chaos, 9(3):519–31, 1999.
- [67] Zounes R. S, Rand R. H., *Subharmonic resonance in the non-linear Mathieu equation*, Int. J. Nonlin. Mech. 37, 43. 2002.

# Appendix

Below are power series expansions for transition curves in Mathieu's equation calculated from solving Hill's equation using harmonic balance in Rand [47]. Those transition curves data shown in Figure 2.2, 2.3 and 2.4 were calculated using these power series expansions.

$$(n = 0)$$

$$\delta = -\frac{\varepsilon^2}{2} + \frac{7\varepsilon^4}{32} - \frac{29\varepsilon^6}{144} + \frac{68687\varepsilon^8}{294912} - \frac{123707\varepsilon^{10}}{409600} + \frac{8022167579\varepsilon^{12}}{19110297600} + \dots \quad (6.1)$$

$$(n = 1)$$

$$\begin{aligned} \delta_{1_l} &= \frac{1}{4} - \frac{\varepsilon^2}{8} + \frac{\varepsilon^3}{32} - \frac{\varepsilon^4}{384} - \frac{11\varepsilon^5}{4608} + \frac{49\varepsilon^6}{36864} - \frac{55\varepsilon^7}{294912} - \frac{83\varepsilon^8}{552960} \\ &\quad + \frac{12121\varepsilon^9}{117964800} - \frac{114299\varepsilon^{10}}{6370099200} - \frac{192151\varepsilon^{11}}{15288238080} + \frac{83513957\varepsilon^{12}}{8561413324800} - \dots \\ \delta_{1_r} &= \frac{1}{4} + \frac{\varepsilon^2}{8} - \frac{\varepsilon^3}{32} - \frac{\varepsilon^4}{384} + \frac{11\varepsilon^5}{4608} + \frac{49\varepsilon^6}{36864} + \frac{55\varepsilon^7}{294912} - \frac{83\varepsilon^8}{552960} \\ &\quad - \frac{12121\varepsilon^9}{117964800} - \frac{114299\varepsilon^{10}}{6370099200} + \frac{192151\varepsilon^{11}}{15288238080} + \frac{83513957\varepsilon^{12}}{8561413324800} + \dots \end{aligned} \quad (6.2)$$

$$(n = 2)$$

$$\begin{aligned} \delta_{2_l} &= 1 - \frac{\varepsilon^2}{12} + \frac{5\varepsilon^4}{3456} - \frac{289\varepsilon^6}{4976640} + \frac{21391\varepsilon^8}{7166361600} \\ &\quad - \frac{2499767\varepsilon^{10}}{14447384985600} + \frac{1046070973\varepsilon^{12}}{97086427103232000} - \dots \\ \delta_{2_r} &= 1 + \frac{5\varepsilon^2}{12} - \frac{763\varepsilon^4}{3456} + \frac{1002401\varepsilon^6}{4976640} - \frac{1669068401\varepsilon^8}{8/7166361600} \\ &\quad + \frac{4363384401463\varepsilon^{10}}{14447384985600} - \frac{40755179450909507\varepsilon^{12}}{97086427103232000} + \dots \end{aligned} \quad (6.3)$$

(n = 3)

$$\begin{aligned}
\delta_{3_l} &= \frac{9}{4} + \frac{\varepsilon^2}{16} - \frac{\varepsilon^3}{32} + \frac{13\varepsilon^4}{5120} + \frac{5\varepsilon^5}{2048} - \frac{1961\varepsilon^6}{1474560} + \frac{609\varepsilon^7}{3276800} \\
&\quad + \frac{4957199\varepsilon^8}{33030144000} - \frac{872713\varepsilon^9}{8493465600} + \frac{421511\varepsilon^{10}}{23488102400} \\
&\quad + \frac{16738435813\varepsilon^{11}}{1331775406080000} - \frac{572669780189\varepsilon^{12}}{58706834227200000} + \dots \\
\delta_{3_r} &= \frac{9}{4} + \frac{\varepsilon^2}{16} + \frac{\varepsilon^3}{32} + \frac{13\varepsilon^4}{5120} - \frac{5\varepsilon^5}{2048} - \frac{1961\varepsilon^6}{1474560} \\
&\quad - \frac{609\varepsilon^7}{3276800} + \frac{4957199\varepsilon^8}{33030144000} + \frac{872713\varepsilon^9}{8493465600} \\
&\quad + \frac{421511\varepsilon^{10}}{23488102400} - \frac{16738435813\varepsilon^{11}}{1331775406080000} - \frac{572669780189\varepsilon^{12}}{58706834227200000} + \dots \quad (6.4)
\end{aligned}$$

(n = 4)

$$\begin{aligned}
\delta_{4_l} &= 4 + \frac{\varepsilon^2}{30} + \frac{433\varepsilon^4}{216000} - \frac{5701\varepsilon^6}{170100000} \\
&\quad - \frac{112236997\varepsilon^8}{31352832000000} + \frac{8417126443\varepsilon^{10}}{123451776000000000} \\
&\quad + \frac{2887659548698709\varepsilon^{12}}{265470699110400000000000} + \dots \\
\delta_{4_r} &= 4 + \frac{\varepsilon^2}{30} - \frac{317\varepsilon^4}{216000} + \frac{10049\varepsilon^6}{170100000} - \frac{93824197\varepsilon^8}{31352832000000} \\
&\quad + \frac{21359366443\varepsilon^{10}}{123451776000000000} - \frac{2860119307587541\varepsilon^{12}}{265470699110400000000000} + \dots \quad (6.5)
\end{aligned}$$